Doctoral Dissertation

Development of standard n-γ mixed fields for dosimetry studies in BNCT

XU ZIXU
徐 子虚

March 2025

Graduate School of Engineering,
Osaka University

Abstract

Boron Neutron Capture Therapy (BNCT) is a promising and rising radiation therapeutic treatment for malignant tumors. However, the treatment field of BNCT is a n-γ mixed field, since contaminant gamma-rays with maximum energy above 10 MeV are produced by neutrons interactions with surrounding substances. Since neutron and gamma-ray deliver different biological effects to human bodies, it is essential to distinguish the exposure absorbed doses of neutron and gamma-ray to patients and radiation workers. Currently, Thermoluminescence Dosimeter (TLD), Optically Stimulated Luminescence Dosimeter (OSLD), and Radio-photoluminescence Glass Dosimeter (RPLGD) are widely used dosimeters for gamma-ray dose measurement in BNCT. In the BNCT project of Osaka University, a method of material-filtered Radio-photoluminescence Glass Dosimeters (RPLGD) has been newly proposed for simultaneous and separate measurement of neutron and gamma-ray doses. To validate the glass dosimeters developed for BNCT, standard fields were demanded but still scarce. Hence, in this dissertation, various types of standard n-γ mixed fields were designed and developed, including fast-neutron (F), epithermal-neutron (E), thermal-neutron (T) -dominated fields, as well as gamma-ray-only fields. In this dissertation, five chapters were contained.

In Chapter 2, the theories and methods used in this dissertation were introduced, including neutron nuclear reactions, neutron and gamma-ray sources, and Monte Carlo simulation software, i.e. Monte Carlo N-Particle code (MCNP) and Particle and Heavy Ion Transport code System (PHITS).

In Chapter 3, various types of n-γ mixed fields were designed by irradiating different moderator assemblies with a D-D neutron source at OKTAVIAN of Osaka University, Japan. The moderator assemblies were designed with different combinations of Fe, W, Pb, Bi, LiF, MgF_2, TiF_3, C, and PE materials. The n-γ mixed fields were determined with the specific characteristics as follows: (1) the dose ratios of gamma-ray to neutron are 1.0-977.0% for F-dominated field, 5.0-921.1% for E-dominated field, 0.7-946.3% for T-dominated field, and 11880.6% for gamma-ray-only field; (2) the proportions of fast, epithermal, and thermal neutron doses to total neutron dose are 98.4-100.0% for F-dominated field, 74.0-85.4% for E-dominated field, and 90.1-90.8% for T-dominated field, respectively; (3) the maximum gamma-ray energy is up to 12 MeV.

In Chapter 4, a ~10 MeV standard gamma-ray field, with characteristic gamma-rays at 2.22, 3.68, 4.95, 5.92, 6.02, 6.38, 6.51, 7.28, 7.64, 8.89, 9.30, and 10.04 MeV, was developed by irradiating a

Fe-PE Cd moderator assembly with a ~2.95 MeV p-Li (thick) neutron source at Fast Neutron Laboratory (FNL), Tohoku University, Japan. The gamma-ray dose rate, $\dot{D}_{\gamma_{air}}$, was confirmed as 3.43 × 10^{-2} μSv·μC^{-1} using GD-301, a type of Radio-photoluminescence Glass Dosimeter (RPLGD), which was consistent with the simulation results of 3.58 × 10^{-2} μSv·μC^{-1} and 3.56 × 10^{-2} μSv·μC^{-1} from MCNP6 and PHITS (ver.3.320), respectively. The gamma-ray spectrum was confirmed using a Ge detector (GC1818, CANBERRA) to identify the characteristic gamma-ray peaks at 2.22 MeV, 5.92 MeV, 6.02 MeV, 7.64 MeV, and 9.30 MeV.

In Chapter 5, a summary of this dissertation and prospects for future work were provided. Plans for future work were proposed to conduct validation experiments on F-dominated, E-dominated, and T-dominated fields, including methods of measuring neutron and gamma-ray doses and spectra separately. In conclusion, the reference n-γ mixed fields can reproduce the neutrons and gamma-rays with the same energy range and spectral shape in BNCT, which is valuable for characterization, optimization, and validation of novel neutron and gamma-ray dosimeters and detectors used in a wide energy range.

Catalogue

Chapter 1. Introduction

1.1 Background

Neutron and gamma-ray sources are widely utilized in radiation research and various applications, including nuclear physics, astrophysics, material physics, medical physics, nuclear power plant, diagnosis and probing, security inspection, radiotherapy, etc. The radiation field surrounding a neutron source is always a n-γ mixed field, comprising neutrons with various energy spectra (thermal, epithermal, and fast neutrons) along with gamma-rays emitted by the neutron source or generated through charged particles and neutron interactions with the surrounding materials. Mostly, isotopic neutron sources, reactor-based neutron sources, and accelerator-based neutron sources are produced as n-γ mixed fields.

Neutrons and gamma-rays deliver different biological effects to human bodies. For nuclear safety and security concern, it is essential to monitor the ambient neutron and gamma-ray doses surrounding a radiation facility. The personal exposure dose is a key parameter to evaluate the radiation level for radiation protection and health physics. Absorbed dose, D, is defined to quantify the dose in any type of matter, as expressed by [1]:

$$D = \frac{d\varepsilon}{dm} \tag{1.1}$$

where $d\varepsilon$ is the average deposit energy imparted by ionizing radiation to the matter and dm is the mass of the matter volume. The unit of D is Gy (J/kg).

At equal absorbed doses, neutrons and gamma-rays produce different levels of biological effects. Radiation quality is related to the type of particles and their energy spectrum. To account for the relative biological effectiveness (RBE) of different types of ionization radiation, equivalent dose, H_T [2], is introduced to weigh the total absorbed dose over an organ or tissue, $D_{T,R}$:

$$H_{T,R} = \sum w_R \cdot D_{T,R} \tag{1.2}$$

where w_R is the radiation weighting factor for the type and energy of neutron and gamma-ray incident on the body and the unit of $H_{T,R}$ is Sv (J/kg). w_R [3] for different types of ionization radiation are listed in Table 1.1 and Figure 1.1. The biological effectiveness of neutrons incident on the human body is strongly dependent on the neutron energies. In Figure 1.1, w_R for neutrons can be defined by a continuous function:

$$w_R = \begin{cases} 2.5 + 18.2 \times e^{-[ln(E_n)]^2/6}, & E_n < 1\ MeV \\ 5.0 + 17.0 \times e^{-[ln(2E_n)]^2/6}, & 1\ MeV \le E_n \le 50\ MeV \\ 2.5 + 3.25 \times e^{-[ln(0.04E_n)]^2/6}, & E_n > 50\ MeV \end{cases} \quad (1.3)$$

Table 1.1. Recommended w_R for different types of ionization radiation [3].

Radiation type	w_R
Photons	1
Electrons and muons	1
Protons and charged pions	2
Alpha particles, fission fragments, heavy ions	20
Neutrons	A continuous function of neutron energy as shown in Figure 1.1

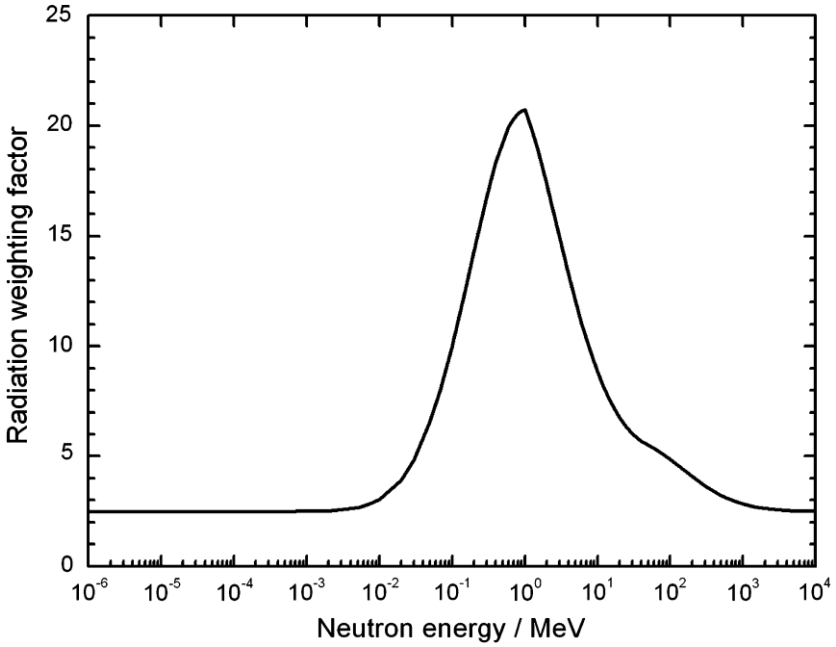

Figure 1.1. w_R for neutrons versus neutron energy [3].

To indicate the combination of different types of radiation doses to several different tissues in a way which is correlated with the total stochastic effects, the effective dose is defined by a weighted sum of tissue equivalent doses as [3]:

$$E = \sum_T w_T \cdot H_{T,R} \quad (1.4)$$

where the unit of E is Sv (J/kg) and w_T is the tissue weighting factor for tissue T. w_T for different tissues and organs are listed in Table 1.2. w_T represents the relative contribution of an organ or tissue

to the total detriment due to these effects resulting from uniform irradiation of the whole body.

Table 1.2. Recommended w_T for different tissues and organs [3].

Tissue and organ	w_T	$\sum w_T$
Bone-marrow (red), Colon, Lung, Stomach, Breast, Remainder tissues	0.12	0.72
Gonads	0.08	0.08
Bladder, Oesophagus, Liver, Thyroid	0.04	0.16
Bone surface, Brain, Salivary glands, Skin	0.01	0.04
	Total	1.00

Apparently, the mixture of neutron and gamma-ray causes challenges and complexity to understand the radiation effects due to their different interactions with materials. In a n-γ mixed field, it is essential to monitor and determine the radiation characteristics of neutrons and gamma-rays. There are many detection instruments for measuring neutrons and gamma-rays, as listed in Table 1.3 [4] [5]. Unlike gamma-rays, neutrons cannot cause ionization directly. Instead, neutrons are detected indirectly by converting them into high-energy photons or charged particles via neutron nuclear reactions. When neutrons are incident on the human body, they will be moderated and scattered, and consequently a flux of thermal and epithermal neutrons are measured to estimate the neutron dose. This process is called albedo neutron dosimetry [6], which has been widely applied for decades.

Table 1.3. Neutron and gamma-ray detectors [4] [5].

	Dosimeter	Spectrometer
Neutron	1. Calorimetry: water calorimeter, graphite calorimeter; 2. Ionization chamber and charge detector: cylindrical and parallel plate ionization chamber, proportional counter, Geiger-mueller counter, Faraday cup; 3. Luminescent dosimeter: Thermoluminescence Dosimeter (TLD), Optically Stimulated Luminescence Dosimeter (OSLD), Radio-photoluminescence Glass Dosimeter (RPLGD); 4. Scintillator: organic and plastic scintillators, liquid scintillator; 5. Chemical dosimeter: Fricke dosimeter, Polymer gels Alanine dosimeter; 6. Radiographic and radiochromic films.	1. Bonner sphere system 2. multi activation foil, 3. multi-counter system
Gamma-ray		1. Gas filled detector: Xe; 2. Scintillator: BGO, NaI:Ti, LaCl3:Ce, LaBr3:Ce 3. Solid-state detector: (CPG) CdZnTe, CdTe, Ge

Luminescent dosimeters, thermoluminescence dosimeters (TLDs) and optically stimulated luminescence dosimeters (OSLDs), are widely used to measure and distinguish neutron and gamma-ray doses in n-γ mixed fields. The TLD consists of a thermoluminescent crystalline material that traps electrons upon exposure to ionization radiation. When the crystalline material is heated, the trapped electrons are released, emitting light proportional to the radiation dose [7].

The Albedo TLDs, composed of MgB_4O_7: Tb or $Li_2B_4O_7$: Cu, are highly responsive to thermal neutrons due to the large (n,γ) cross sections of ^{6}Li and ^{10}B [8]. In contrast, the albedo TLDs, composed of Mg_2SiO_4: Tb and BeO, are used for gamma-ray dose measurement since these TLDs are relatively insensitive to thermal neutrons. Additionally, ^{6}Li is widely used as a shielding material to correct low-energy neutron contamination.

OSLs and TLDs are very similar, and the only difference is that the OSL releases trapped electrons when the crystalline material is stimulated with light. There are only two crystalline materials commercially available for the OSL [9], i.e. α-Al_2O_3: C and BeO. However, neither of these two materials is sensitive to neutrons due to the small (n,γ) cross sections. Some novel crystalline materials with intrinsic neutron sensitivity are proposed, i.e. $Li_2B_4O_7$, MgB_4O_7, and $LiMgPO_4$. Alternatively, commercially available OSLDs are combined with ^{6}Li or ^{10}B contained materials to enhance response to thermal neutrons.

TLDs and OSLDs have fading effect and cannot be used for repeatable readout [10]. On the contrary, another luminescent dosimeter, the radio-photoluminescence glass dosimeter (RPLGD), has become popular for gamma-ray dose measurement. The RPLGD has its advantages of no fading effect and repeatable readout [11] since the readout process does not eliminate the luminescent centers inside the RPLGD. The RPLGD forms the color centers when the radio-photoluminescent material is exposed to radiation, which emits fluorescence after irradiating with ultraviolet light. However, the RPLGD cannot detect neutrons directly. It is demanded to develop novel methods of applying the RPLGD for neutron dose measurement.

1.2 Boron Neutron Capture Therapy

1.2.1 Cancer in Japan

Cancer has become a major public health concern in Japan. In 2020 [12], 945,055 new cancer cases (Male: 534,814 cases; Female: 410,238 cases) were diagnosed in Japan. In 2023, 382,504 people (Male: 221,360 cases; Female: 161,144 cases) were dead from cancer in Japan. Statistically, one in every two Japanese people (Male: 62.1%; Female: 48.9%) were diagnosed with cancer in their lifetime. Among these diagnosed people, one in every two Japanese males (24.7%) and one in every six Japanese females (17.2%) were dead from cancer. As shown in Figure 1.2, in 2023 [13], malignant neoplasm (24.3%) had become the major cause of death in Japan. In Figure 1.3, the number of deaths due to malignant neoplasms exhibits a rapid rising trend from 1947 to 2023 [14].

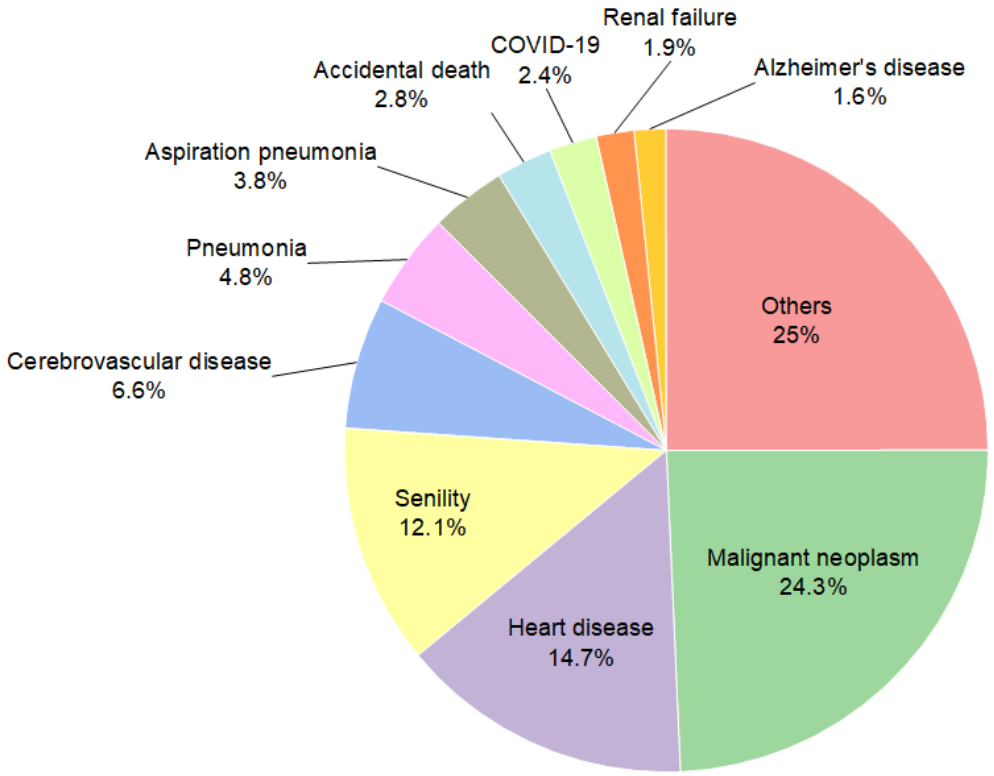

Figure 1.2. Percentage of annual deaths by cause in Japan (2023) [13].

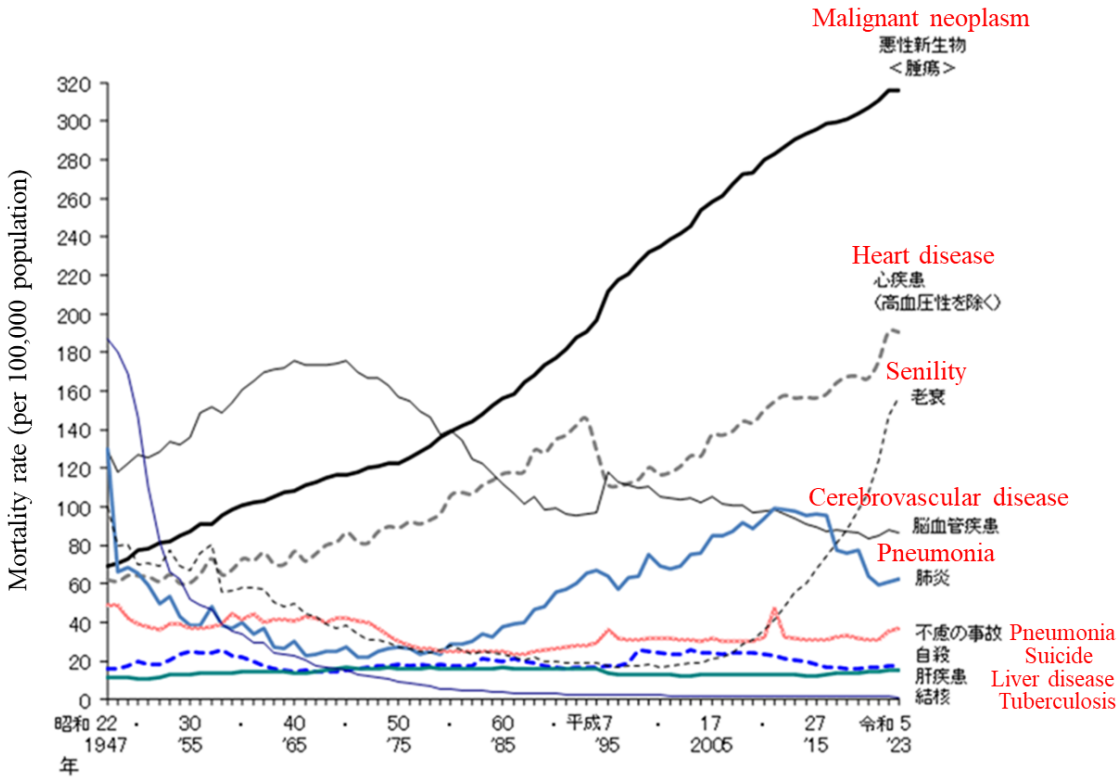

Figure 1.3. Annual trends in mortality rates by major causes of death (per 100,000 population) [14].

There are three major methods for cancer treatment, including surgery, chemotherapy, and radiation therapy. Radiation therapy uses high doses of radiation to kill cancer cells and shrink tumors by damaging their DNA. Radiation therapy can prevent cancer from returning and stop or slow cancer's growth. Currently, various types of radiation are used for therapeutic purposes, including X-rays, electrons, photons, protons, heavy ions, neutrons, etc. Over the past two decades, Japanese government has been developing radiation therapy in Japan. In Figure 1.4, more and more cancer patients have received radiation therapy in Japan [15]. In the future, radiation therapy will occupy a significant position in cancer treatment.

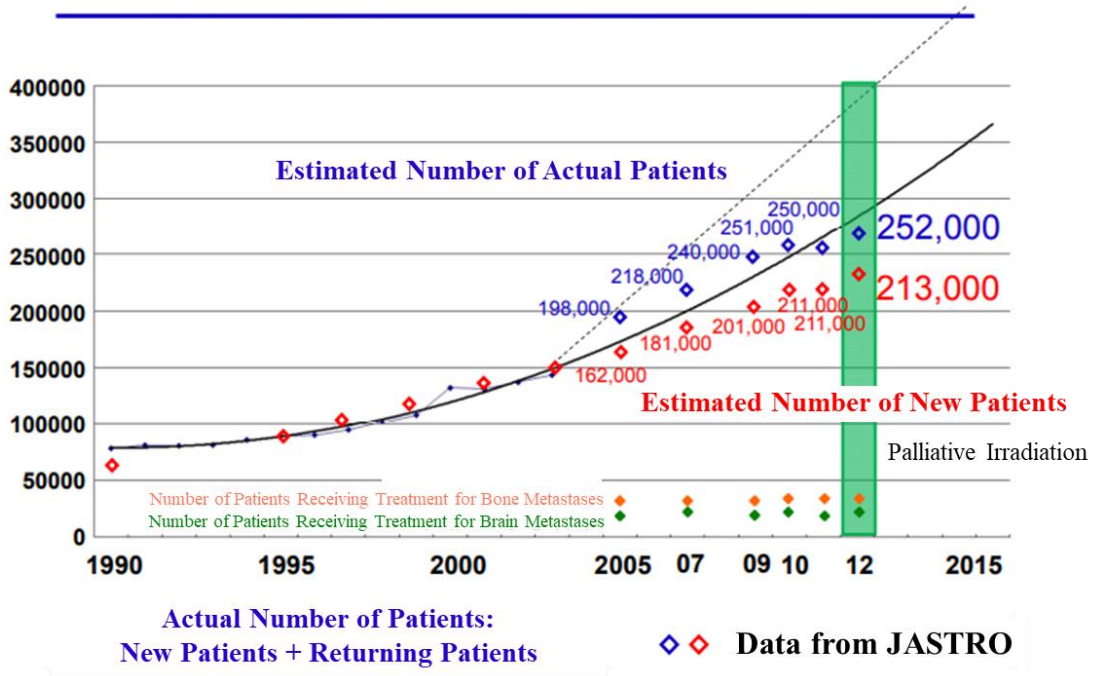

Figure 1.4. Trend of Radiation Therapy Cases (the Number of Patients) [15].

1.2.2 Boron Neutron Capture Therapy

Boron neutron capture therapy (BNCT) [16] is a neutron-based technique that allows selective cancer treatment at the tumor cellular level. It is especially suitable for treatment of brain, head, neck and skin cancers. BNCT is biochemically targeted radiotherapy that utilizes the neutron capture reaction between a thermal neutron and a ^{10}B nucleus. Before commencing BNCT, boron compounds are infused into a patient's body and concentrated in tumor cells by delivery agents. After exposing the patients to thermal and epithermal neutrons, neutron capture reactions occur. In each reaction, two

high-energy nuclei, a ^{4}He nucleus and a ^{7}Li nucleus, are produced within a combined range of 12-13 μm in tissue, which creates a high degree of localized damage to the tumor cell accurately. The nuclear reaction is as follows [17]:

$$^{10}B + \mathrm{n} \rightarrow \begin{cases} \xrightarrow{6\%} {}^{4}He + {}^{7}Li + 2.79\ \mathrm{MeV} \\ \xrightarrow{94\%} {}^{4}He + {}^{7}Li^{*}\ [{}^{7}Li + \gamma\,(0.477\ \mathrm{MeV})] + 2.33\ \mathrm{MeV} \end{cases} \tag{1.5}$$

A schematic of the principle of BNCT is shown in Figure 1.5. With both thermal and epithermal neutron neutrons, the treatable depth can be extended to 8-10 cm. Compared with the conventional radiation therapy (X-ray and electron beam), proton and heavy ion therapy, BNCT demonstrates a superior ability to destroy the tumor cells while leaving normal tissues undamaged.

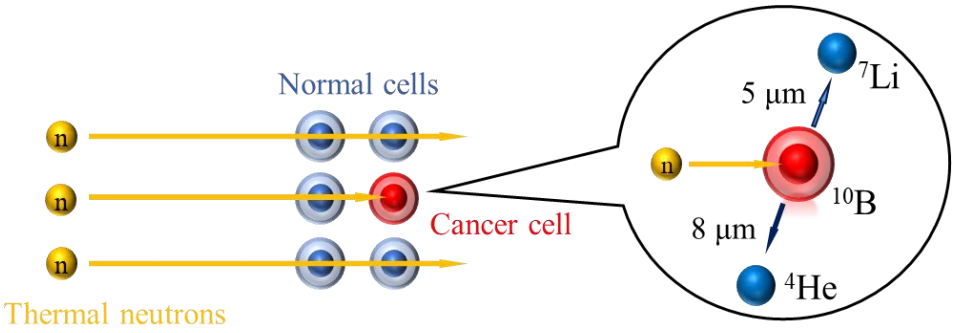

Figure 1.5. Schematic of the principle of BNCT.

In 2020 [18], BNCT was officially approved in Japan as a clinical therapy covered by the National Health Insurance. Since then, BNCT has become a rising and promising technique, undergoing a major resurgence of interest around the world. As of early 2024, there were 29 BNCT projects [19] recorded by International Atomic Energy Agency (IAEA), as shown in Figure 1.6. Over the past two decades, significant progress has been made in the development of accelerator-based BNCT (AB-BNCT) systems, as summarized in Table 1.4 [16] [19] [20] [21]. Various types of proton and deuteron accelerators are operated with energies from ~1.5 MeV to 30 MeV. For AB-BNCT, high-intensity neutron sources (> 10^{13} n·s^{-1}) are produced by proton or deuteron beams incident to lithium or beryllium targets via ^{7}Li(p,n)^{7}Be, ^{9}Be(p,n)^{9}B, ^{7}Li(d,n)^{8}Be, or ^{9}Be(d,n)^{10}B reactions [22].

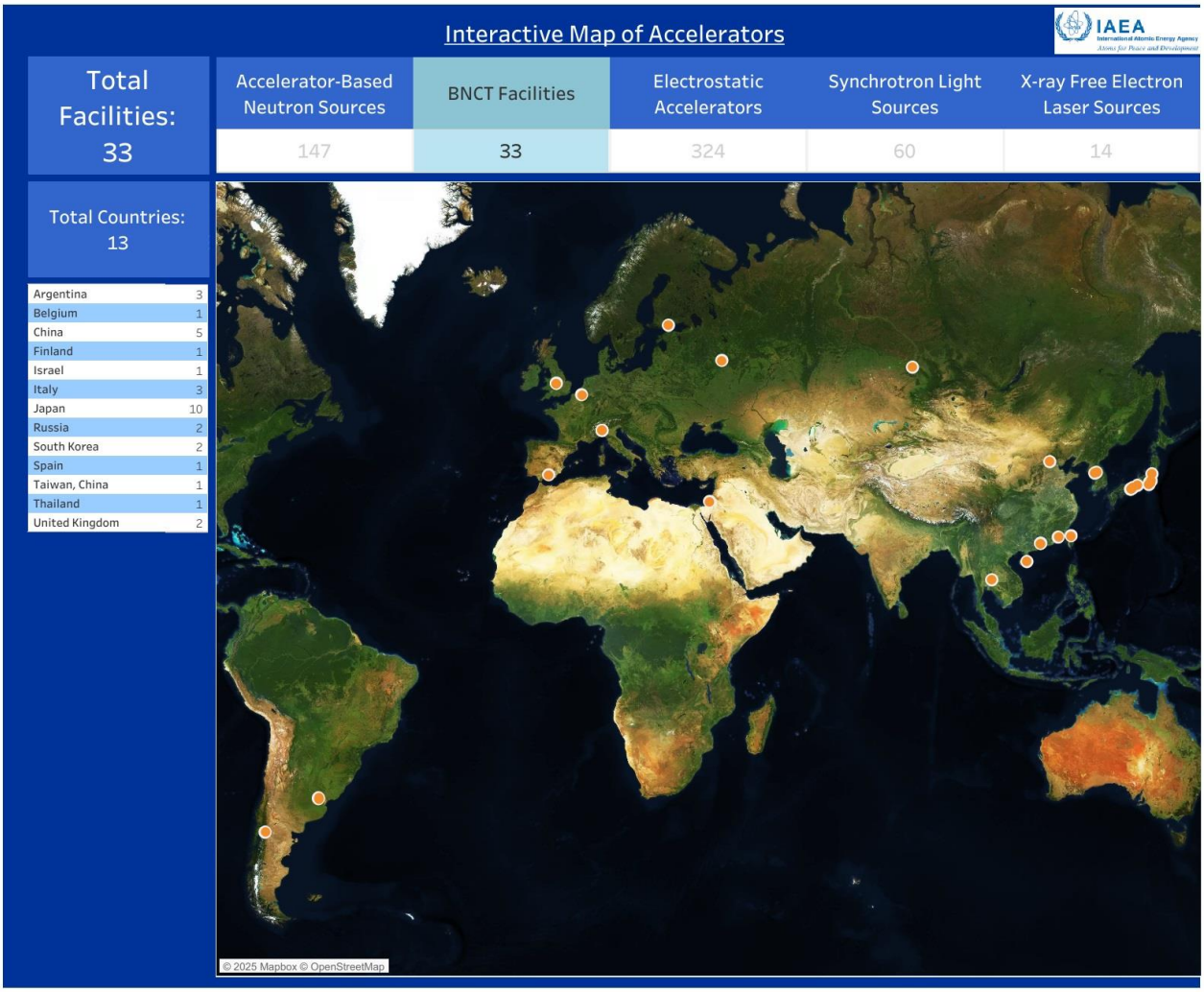

Figure 1.6. Distribution of operational BNCT facilities in the world [19].

Table 1.4. Current status and performance of AB-BNCT facilities [16] [19] [20] [21].

Country	Project	Institution	Accelerator	Beam energy (MeV)	Current goal (mA)	Current status
Japan	C-BENS	Kyoto University	Cyclotron, 5.5 mm ^{9}Be(p,n)	30	1	Clinical trial
	NeuCure (BNCT30)	Southern Tohoku BNCT Research Center	Cyclotron, 5.5 mm ^{9}Be(p,n)	30	1	Clinical treatment
	NeuCure (BNCT30)	Kansai BNCT Medical Center	Cyclotron, 5.5 mm ^{9}Be(p,n)	30	1	Clinical treatment
	NCC CICS-1	National Cancer Center Hospital	RFQ, Solid ^{7}Li(p,n)	2.5	20	Clinical trial
	CICS-2	Edogawa Hospital	RFQ, Solid ^{7}Li(p,n)	2.5	20	Clinical trial

	iBNCT	University of Tsukuba	RFQ+DTL, 0.5 mm ^{9}Be(p,n)	8	10	Clinical treatment
	nuBeam	Shonan Kamakura General Hospital	Electrostatic, Solid ^{7}Li(p,n)	2.6	30	Commissioning
	NUANS	Nagoya University	Electrostatic, Solid ^{7}Li(p,n)	2.8	15	Commissioning
China (Mainland)	NeuCure (BNCT30)	Boao BNCT center	Cyclotron, 5.5 mm ^{9}Be(p,n)	30	1	Under construction
	CYCIAE-14B (CIAE-AB-BNCT)	Tai'an Central Hospital	Cyclotron, ^{9}Be(p,n)	14	1	Commissioning
	D-BNCT01	Dongguan Neuron Science Center	RFQ, Solid ^{7}Li(p,n)	3.5	5	Operational
	D-BNCT02	Dongguan People's Hospital	RFQ, Solid ^{7}Li(p,n)	2.8	20	Under construction
	LU AB-BNCT	Fujian Medical University Union Hospital (Mazu Hospital)	RFQ, Solid ^{7}Li(p,n)	2.5	30	Commissioning
	X-TANS	Xi'an Jiaotong University	RFQ Li	14	1	Under development
	NeuPex	Xiamen Humanity Hospital	Electrostatic, Solid ^{7}Li(p,n)	2.5	10	Clinical trial
Finland	nuBeam	Helsinki University Hospital	Electrostatic, Solid ^{7}Li(p,n)	2.6	30	Commissioning
Spain	NeMeSis	Granada University Hospital	Electrostatic, Solid ^{7}Li(p,n)	2.1	30	Under development
Italy	Alphabeam	Fondazione Centro Nazionale Adroterapia Oncologica (CNAO)	Electrostatic, Solid ^{7}Li(p,n)	2.5	10	Under construction
Russia	Legnaro-RFQ	Italian Institute of Nuclear Physics (INFN)	Electrostatic, Solid ^{9}Be(p,n)	5	30	Under development
	VITA	Budker Institute of Nuclear Physics	Electrostatic, Solid ^{7}Li(p,n)	2.0-2.3	10	Operational
	VITA	Blokhin National Medical Research Center of Oncology	Electrostatic, Solid ^{7}Li(p,n)	2.3	7	Under construction
Israel	SARAF-LiLiT	Soreq Nuclear Research Center	RFQ-DTL, Liquid ^{7}Li(p,n)	2.5	20	Under development
Argentina	ES1	CNEA	ESQ 8 µm ^{9}Be(d,n), thick ^{13}C(d,n)	1.45	30	Under construction
South Korea	A-BNCT	Gachon University Gil Medical Center	Electrostatic, Thick ^{9}Be(p,n)	10	8	Preclinical
Belgium	KIRAMS AB-BNCT	Korea Institute of Radiological and Medical Sciences (KIRAMS)	ESQ 8 µm ^{9}Be(d,n), thick ^{13}C(d,n)	1.45	30	Under construction

UK	HF ADNF	Birmingham University	Electrostatic, Solid ^{7}Li(p,n)	2.6	30	Commissioning
Belgium	nuBeam	University Hospital of Brussels	Electrostatic, Solid ^{7}Li(p,n)	2.6	30	Planning

However, the irradiation field of BNCT is a n-γ mixed field. In BNCT, a substantial number of contaminant gamma-rays are generated at the neutron beam exit due to neutron capture and scattering reactions in the beamline structure, beam shaping assembly (BSA), surrounding medical equipment, and shielding room. Additionally, secondary gamma-rays are produced inside the patient's body, e.g. 2.22 MeV gamma-rays from the $^{1}H(n,\gamma)^{2}H$ reaction [16].

According to the reference spectra of neutrons and gamma-rays in the BNCT treatment field of the Nagoya University Accelerator-driven d-Li Neutron Source (NUANS), contaminant gamma-rays were generated with maximum energy above 10 MeV and mixed within the neutron beam, as shown in Figure 1.7 [23]. Hence, it is crucial to monitor these gamma-rays and evaluate their radiobiological effects on the human body during treatment, since these high energy gamma-rays have deep tissue penetration ability and result in a non-selective dose to both tumor tissue and a large volume of healthy tissue [17].

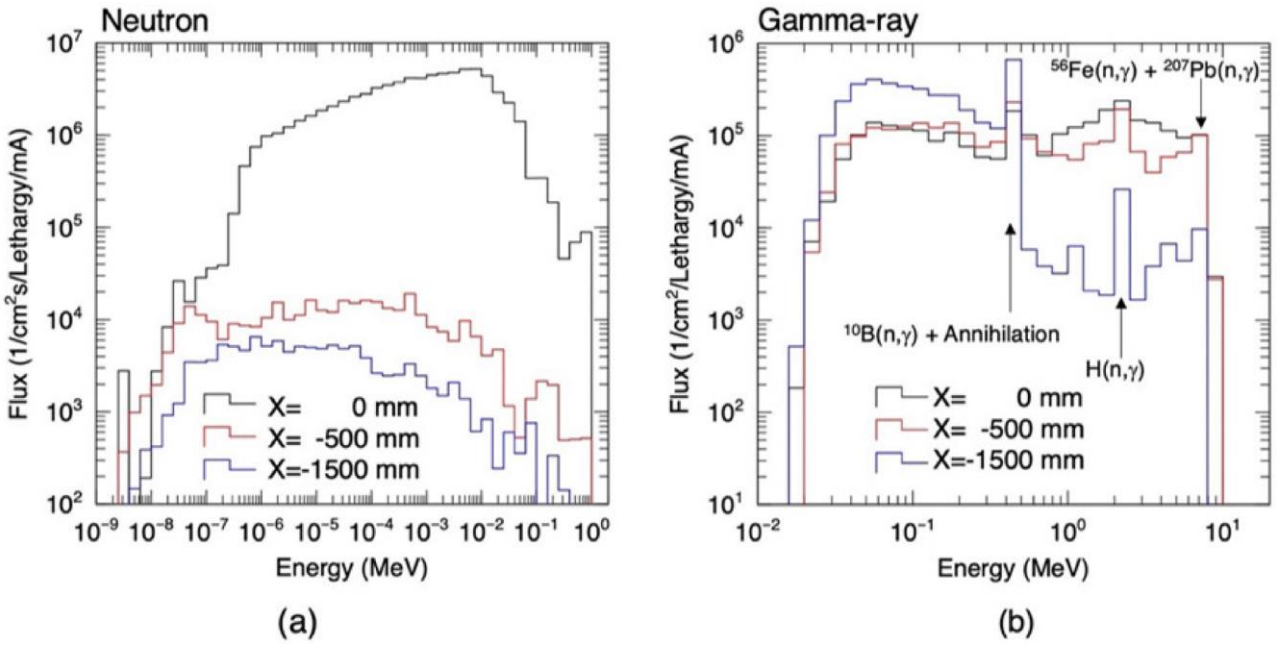

Figure 1.7. Spectra of (a) neutrons and (b) gamma-rays at the center of the BSA outlet (X = 0 mm), outside the BSA outlet (X = 500 mm), and near the wall (X = 1500 mm) [23].

1.3 Objective

Currently, TLDs, OSLDs, and RPLGDs are widely used gamma-ray dosimeters. Using these dosimeters, various novel glass dosimeters have been developed for n-γ mixed fields. Shunsuke Suzuki, et al. [24] proposed a new approach to evaluate γ-ray dose in BNCT combining Mg_2SiO_4: Tb (TLD-MSO-S) and ^{6}LiF sintered capsule. TLD-MSO-S are highly responsive to thermal neutrons while ^{6}LiF has large low-energy neutron absorption cross sections. The ^{6}LiF sintered capsule removed low-energy neutrons to evaluate the gamma-ray dose with an accuracy of within ±7% between calculated and measured values and ±7% of reproducibility. Kiyomitsu Shinsho, et al. [25] introduced a BeO ceramic plate (TLD) that contains no Na effect on thermoluminescent elements due to the thermal neutron capture reactions and no beryllium toxicity released into air, compared to Na-doped BeO powder TLD. Na-doped BeO powder TLD has high accuracy for gamma-ray dose measurement in n-γ mixed fields, however, the effect of even small amounts of Na added to a TLD is not negligible. The results suggested that BeO ceramic plates can selectively measure only γ-rays in high thermal neutron fluence fields without any correction for neutron effects. Nishiki Matsubayashi, et al. [26] characterized a BeO ceramic OSLD which has good linear of gamma-ray dose at several hundred mGy and lower thermal neutron sensitivity than Na-doped BeO powder TLD. No significant self-activation was found for the BeO ceramic OSLD.

In the BNCT project of Osaka University, our group has been developing a material-filtered RPLGD for separate and simultaneous measurement of neutron and gamma-ray doses in BNCT. K. Hiramatsu, et al. [27] and K. Tochitani, et al. [28] proposed a method of using two special shape of leader filters to estimate the gamma-ray dose rate from ~100 keV to ~10 MeV. F. Kamisaki, et al. [29] designed a delicate iron filter that reproduced the air kerma coefficients within an error of 5.3% in the gamma-ray energy range up to 10 MeV. Our group is now optimizing a filter with mixed materials to minimize the angular dependence of the material-filtered RPLGD for gamma-ray dose measurement in high-energy range. Meanwhile, we are developing a dual-filter method aimed at achieving the ultimate goal of separate and simultaneous measurement of neutron and gamma-ray doses.

Obviously, the newly developed TLDs, OSLDs, and RPLGDs demand standard n-γ mixed fields for comprehensive characterization, optimization, and calibration across a wide range of neutron and

gamma-ray energies. Standard n-γ mixed fields enable the study of complex real-world radiation environments, support the development of advanced materials, enhance medical treatments, and ensure nuclear safety.

In previous studies, various standard n-γ mixed fields were developed using isotopic neutron sources, reactor-based neutron sources, or accelerator-based neutron sources. K. Jozefowicz, et al. [30] established nine different n-γ mixed fields by ^{252}Cf, ^{241}Am-Be, and ^{239}Pu-Be sources exposed to either free-in air or surrounded with 10 cm paraffin or ion filters. The dose ratio of gamma to neutron ranged from 11% to 233%, and the total dose rate was 8-115 μGy/h at 1 m distance. B. Tournier, et al. [31] reported SILENE fission reactor source that provided a range of calibrated n-γ mixed fields. This source produced dose ratios of gamma-ray to neutron as 20%, 40%, 150%, and 1000% and a total dose rate from ~10^{-4} to ~10^{6} μGy/h at 4 m from the core by using lead, polyethylene, and steel shields. M. Ferrari, et al. [32] developed a n-γ mixed irradiation station at CERN by spallation neutrons with energies from 0.025 eV to several hundreds of MeV. At this station, the dose ratio of gamma-ray to neutron and the total dose rate were calculated as 23-45% and 0.36-0.68 Gy/pulse, respectively.

However, current research demands a wide radiation energy range and variable dose ratio of gamma-ray to neutron in n-γ mixed fields to reproduce the radiation effects occurring in real-life conditions. So far, data collected in standard n-γ mixed fields are still scarce. To meet the growing demands for standard n-γ mixed fields, it is critical to develop standard n-γ mixed fields with flexibility to adjust the dose ratio of gamma-ray to neutron into arbitrary values, shift neutron spectra, and provide gamma-rays in a wide energy range.

In this dissertation, various standard n-γ mixed fields were designed and developed with arbitrary dose ratios of gamma-ray to neutron, classification of dominant energies from thermal to fast neutrons, and a high gamma-ray energy range of up to ~10 MeV. These standard fields were classified into fast-neutron (F), epithermal-neutron (E), thermal-neutron (T) -dominated fields, as well as gamma-ray-only fields. These standard fields were generated using different moderator assemblies irradiated with a D-D neutron source (2.5 MeV) at OKTAVIAN [33], Osaka University, and a ~2.95 MeV p-Li neutron source at the 4.5 MV Dynamitron facility, Fast Neutron Laboratory (FNL) [34], Tohoku University.

1.4 Outline

Chapter 2 introduces basic theories and simulation calculation tools in this dissertation. The mechanisms of common neutron nuclear reactions are presented to explain how neutrons interact with matter and how secondary gamma-rays are generated. Neutron reaction cross section is introduced for material selection. Various common neutron sources and gamma-ray sources are classified and described for understanding of their advantages and limitations. The principle and use of RPLGD are introduced, with a method for applying it to gamma-ray dose measurement in high-gamma-ray energy fields. Additionally, two Monte Carlo simulation software tools are also introduced, which support all the theoretical particle transport calculations in this dissertation.

Chapter 3 presents a detailed simulation study about designing various types of n-γ mixed fields, including introduction of the OKTAVIAN facility, design of different moderator assemblies, classification and characterization of the n-γ mixed fields, dose rate at OKTAVIAN for practical use, and analysis of the wall scattering effect in the heavy irradiation room at OKTAVIAN.

Chapter 4 presents an experimental study about developing a high-energy gamma-ray field, including the design and performance of the moderator assembly, source term of a p-Li neutron, characterization of the gamma-ray field, experiment results of gamma-ray dose and energy spectrum measurements, analysis of electron occurrence in a high-energy gamma-ray field, a method of removing the electron contribution to a glass dosimeter, and analysis of the wall scattering effect in the experimental room at FNL.

Chapter 5 provides a retrospective summary of this study, highlighting the originality of the research objective, the core content of each chapter, basic method and tool, significant analyses and results. Finally, a future research plan is proposed to proceed with the research about neutron validation of the moderator assembly designed in Chapter 4 and validation of the n-γ mixed fields designed in Chapter 3.

Chapter 2. Theories and methods

2.1 Neutron nuclear reaction

Neutron nuclear reaction defines that a neutron interacts with a nuclear particle to produce two or more nuclear particles. The important reactions are those that occur at relatively low energies, several MeV or less [35]. Generally, neutron nuclear reactions are classified into elastic scattering, inelastic scattering, neutron capture, transmutation, and fission.

2.1.1 Elastic scattering

Elastic scattering [35], (n,n) reaction, occurs when a neutron interacts with any target nucleus. In elastic scattering, a neutron and a nucleus collide with no change in the structure of the target nucleus (or of the neutron), as shown:

$$\mathrm{n} + {}^{A}_{Z}X \rightarrow {}^{A}_{Z}X + \mathrm{n} \tag{2.1}$$

There is no energy transferred into nuclear excitation in an elastic scattering between a neutron and a target nucleus, but some of the neutron energy is transferred to the target nucleus. When the target nucleus is relatively light, the loss of neutron kinetic energy is relatively large. In such cases, elastic scattering is effective to reduce neutron energy without depleting their number.

2.1.2 Inelastic scattering

In inelastic scattering [35], (n,n'γ) reaction, some energy of the incident neutron is absorbed into a recoiling nucleus and the excited nucleus decays quickly to the ground state with gamma-ray emission, as shown in:

$$\mathrm{n} + {}^{A}_{Z}X \rightarrow {}^{A}_{Z}X^{*} + \mathrm{n} \rightarrow {}^{A}_{Z}X + \mathrm{n} + \gamma\text{'s} \tag{2.2}$$

Inelastic scattering is possible only if the neutron energy exceeds a characteristic threshold for the element. Thus, inelastic scattering can contribute to the initial slowing down of neutrons.

2.1.3 Neutron capture reaction

Neutron capture [35], (n,γ) reaction, can occur for almost any targets and results in an excited compound nucleus and neutron absorption coupled with the production of one or more gamma rays,

as shown:

$$\mathrm{n} + {}^{A}_{Z}X \rightarrow {}^{A+1}_{Z}X^{*} \rightarrow {}^{A+1}_{Z}X + \mathrm{n} + \gamma\text{'s} \tag{2.3}$$

In neutron capture, gamma-rays are produced with characteristic energies depending on neutron energy and target isotopes.

2.1.4 Transmutation

A target nucleus may absorb a neutron and form as a compound nucleus which then emits a charged particle, e.g. a proton or an alpha particle. Transmutation produces a nucleus of a different element, as shown in:

$$\begin{cases} \mathrm{n} + {}^{A}_{Z}X \rightarrow {}^{A}_{Z-1}Y + \mathrm{p} \\ \mathrm{n} + {}^{A}_{Z}X \rightarrow {}^{A-3}_{Z-3}Y + \alpha \end{cases} \tag{2.4}$$

Gamma-rays might be emitted if the final nucleus is left in an excited state.

2.1.5 Nuclear fission

In nuclear fission, the neutron is completely absorbed, and the excited compound nucleus divides into two main fragments plus several neutrons and photons and releases a large amount of energy. A typical fission reaction for a ^{235}U target is shown in:

$$\mathrm{n} + {}^{235}_{92}U \rightarrow {}^{236}_{92}U^{*} \rightarrow {}^{144}_{56}Ba + {}^{89}_{36}Kr + 3\mathrm{n} \tag{2.5}$$

Fission is possible for only a few target nuclei, especially isotopes of uranium and plutonium.

2.2 Neutron reaction cross section

When neutrons incident on a target, only a small fraction of neutrons produces a nuclear reaction. In a nuclear reaction, a single neutron interacts with an individual target nucleus. An important parameter, cross section [36], is defined as a quantitative measure of the probability of a nuclear reaction occurring, representing the effective area presented by the target nucleus to an incoming projectile for a specific reaction.

In Figure 2.1, a parallel neutron beam incidents on a thin target foil (one atomic layer thick). The number, C, of interactions is proportional to the intensity, I_0, of the neutron beam and the atomic density N_a (atoms/cm2) [37]:

$$C \propto I_0 \cdot N_a$$

$$C = \sigma \cdot I_0 \cdot N_a \tag{2.6}$$

where the constant, σ, is called nuclear reaction cross section. Since the nuclear radius is ~10^{-14} to 10^{-15} m, the cross section is ~10^{-28} m^2. The common unit of reaction cross section is a barn:

$$1 \text{ barn} = 10^{-28} \text{ m}^2 \tag{2.7}$$

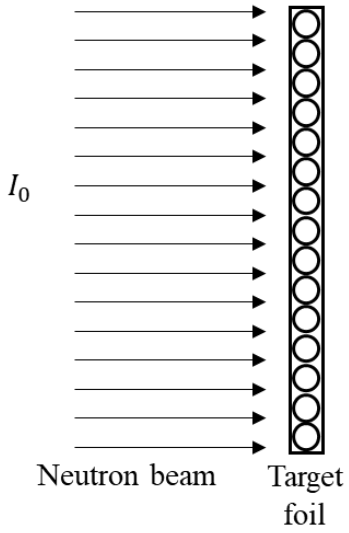

Figure 2.1. Nuclear reaction cross section: bombardment of target foil [37].

Evaluated nuclear data libraries are essential resources about cross section for nuclear research. These libraries compile data from experimental measurements and theoretical models to ensure accurate simulations and analyses. Several major evaluated nuclear data libraries have been developed and updated by national and international organizations, as listed as follows:

1. BROND (Russian Evaluated Neutron Data Library, Russia) [38]
   Latest version: BROND-3.1 (2016);
2. CENDL (Chinese Evaluated Nuclear Data Library, China Nuclear Data Center, China) [39]
   Latest version: CENDL-3.2 (Jun. 12, 2020);
3. ENDF/B (Evaluated Nuclear Data File, National Nuclear Data Center, USA) [40]
   Latest version: ENDF/B-VIII.0 (Feb. 2, 2018);
4. JEFF (Joint Evaluated Fission and Fusion File, Nuclear Energy Agency, Europe) [41]
   Latest version: JEFF-3.3.1 (Dec. 2019);

5. JENDL (Japanese Evaluated Nuclear Data Library, JAEA Nuclear Data Center, Japan) [42]
   Latest version: JENDL-5 (Dec. 2021);
6. TENDL (TALYS-based Evaluated Nuclear Data Library, TALYS) [43]
   Latest version: TENDL-2021 (Dec. 30, 2021).

2.3 Neutron source

Generally, neutrons are classified according to their kinetic energies. There is an approximate categorization of neutrons as follows: cold neutrons (< 0.025 eV), thermal neutrons (0.025 eV-0.5 eV), epithermal neutrons (0.5 eV – 10 keV), fast neutrons (10 keV – 10 MeV), and high energy neutrons (> 10 MeV). Neutron sources are valuable for probing the structure and composition of materials, enabling advancements in fields ranging from physics and materials science to medicine and nuclear engineering.

2.3.1 Isotope neutron source

2.3.1.1 Fission neutron source

^{252}Cf neutron source [44] is widely applied and emits neutrons by spontaneous fission. The half-life of ^{252}Cf is 2.731 years. In Figure 2.2, the average energy of ^{252}Cf is 2.14 MeV.

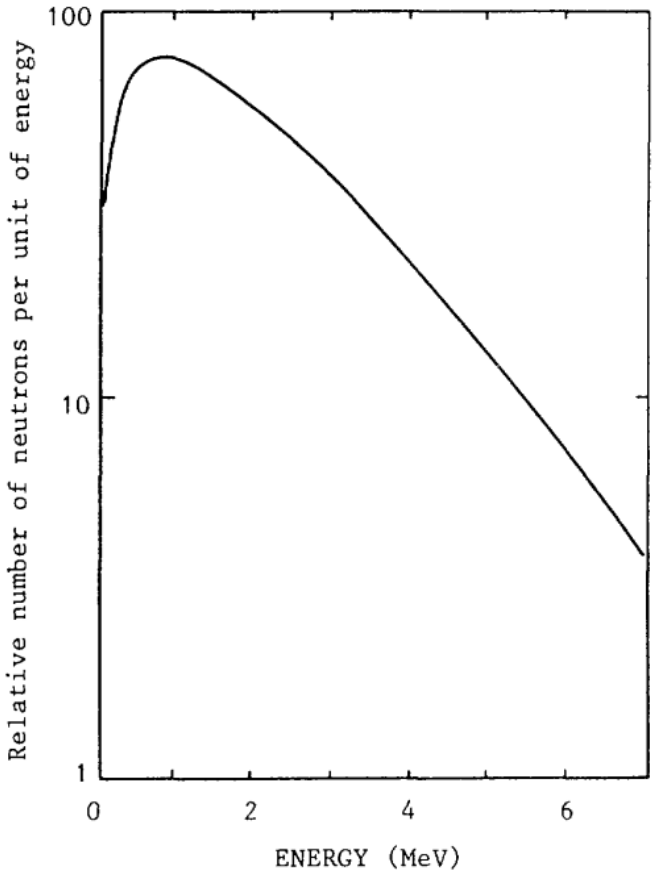

Figure 2.2. Neutron spectrum of ^{252}Cf [44].

2.3.1.2 (α,n) neutron source

Radioactive α-emitters can be used as neutron sources as they induce (α,n) reactions on target nuclides. The characteristics of (α,n) sources are shown in Table 2.1 [45].

Table 2.1. Characteristics of standard (α,n) sources [45].

Source	Half-life	Average neutron energy (MeV)
^{210}Po-Be	138 d	4.3
^{242}Cm-Be	162 d	4
^{228}Th-Be	1.9 y	-
^{244}Cm-Be	17.9 y	4
^{227}Ac-Be	21.8 y	-
^{238}Pu-Be	86.4 y	4
^{241}Am-Be	458 y	4
^{226}Ra-Be	1600 y	3.6
^{249}Pu-Be	24400 y	4.5
^{241}Am-B	458 y	3
^{241}Am-F	458 y	1.5
^{241}Am-Li	458 y	0.5

2.3.1.3 (γ,n) neutron source

(γ,n) neutron source emits nearly-monoenergetic neutrons when the γ-emitter is also monoenergetic. ^{124}Sb and ^{88}Y are commonly used (γ,n) neutron sources. The characteristics of these two sources are summarized in Table 2.2 [45].

Table 2.2. Characteristics of standard (γ,n) sources [45].

γ-emitter	Half-life	Gamma-ray energy (MeV)	Target	Average neutron energy (keV)
^{124}Sb	60 d	1.691, 2.091	Be	26
^{88}Y	107 d	1.836	Be	200

2.3.2 Reactor-based neutron source

Reactors generate neutrons based on the continuous, self-sustained fission reactions of fissile materials, e.g. ^{235}U or ^{239}Pu. The distribution of neutron spectrum is centered around 1 MeV [46]. The

exact design of reactors is dependent on features, i.e. the shape and size of the core, the arrangement and type of fuel elements, control rods, coolant, moderators, reflectors, and beam tubes. Most of the emitted neutrons are moderated in the cooling liquid, i.e. D_2O or H_2O and graphite to produce thermal neutrons with lower energy. The moderated neutrons are directed to experimental areas using beamlines.

There are some famous high-flux reactors in the world [47]: HFR (1972) at the Institut Laue-Langevin (ILL), France, JRR3 (1990) at the Japan Atomic Energy Agency, HANARO (1997) at the Korea Atomic Energy Research Institute, FRM-II (2004) at Technical University of Munich, Germany, OPAL (2006) at the Australian Nuclear Science and Technology Organization, and the CARR (2008) at China institute of atomic energy. In Figure 2.3 [48], the nuclear power reactors in the world are listed. By November 30th, 2024, there were 811 reactors in the world.

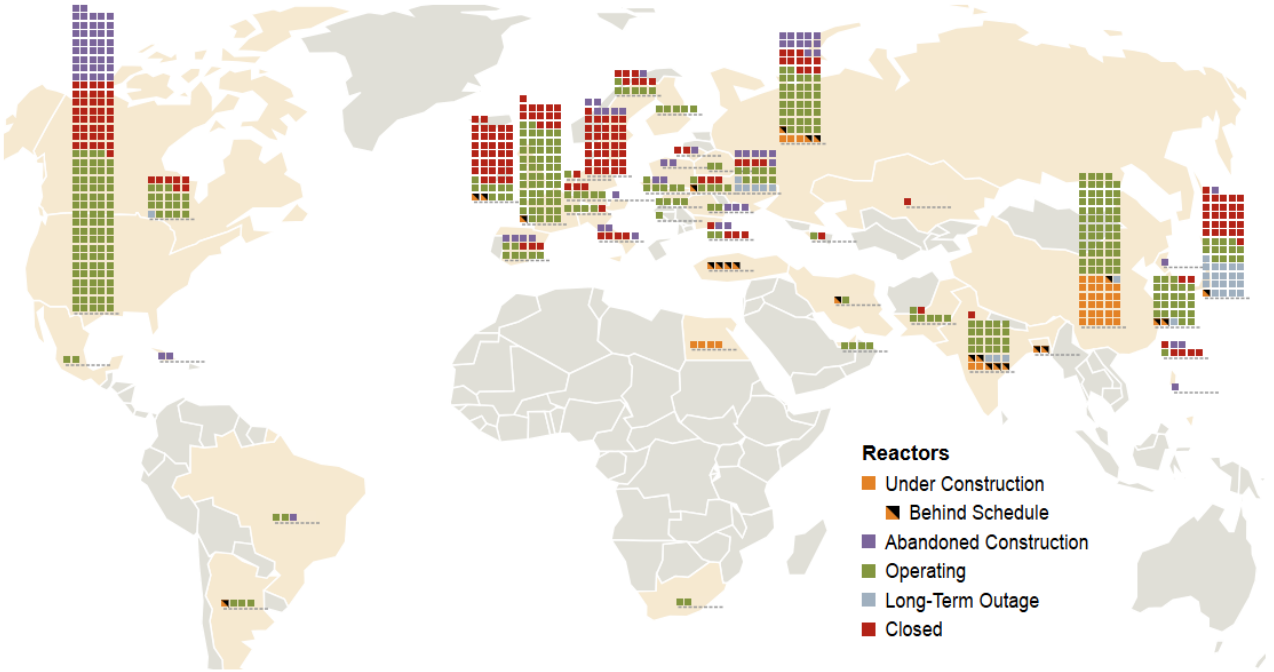

Figure 2.3. Nuclear Power Reactors in the world [48].

2.3.3 Accelerator-based neutron source

Accelerator-based neutron sources generate neutrons through the interaction of accelerated charged particles with a target material. Compact accelerator-based neutron sources (CANS) are a variety of different lower energy accelerators that produce neutrons. The neutron production targets

and the reactions are a key component of a CANS system. The materials used in targets depend on the nuclear reactions used to produce neutrons which can be fusion, low energy nuclear reactions, stripping reactions, and fission. Different nuclear reactions producing neutrons are listed below [49]:

(1) Fusion:

$$\begin{cases} {}^{2}H + {}^{3}H \rightarrow {}^{4}He + n + 17.58\ MeV \\ {}^{2}H + {}^{2}H \rightarrow {}^{3}He + n + 3.27\ MeV \\ {}^{3}H + {}^{3}H \rightarrow {}^{4}He + 2n + 11.32\ MeV \\ {}^{3}H + {}^{3}He \rightarrow {}^{4}He + p + n + 12.1\ MeV \end{cases} \tag{2.8}$$

(2) Low energy nuclear reactions with protons or deuterons:

$$\begin{cases} {}^{7}Li + p \rightarrow {}^{7}Be + n - 1.65\ MeV\ (Threshold\ energy\ 1.88\ MeV) \\ {}^{9}Be + p \rightarrow {}^{9}B + n - 1.85\ MeV\ (Threshold\ energy\ 2.06\ MeV) \\ {}^{9}Be + d \rightarrow {}^{10}B + n + 4.36\ MeV \\ {}^{7}Li + d \rightarrow {}^{8}Be + n + 15.03\ MeV \\ {}^{7}Li + d \rightarrow 2 \times {}^{4}He + n + 15.12\ MeV \\ {}^{7}Li + d \rightarrow {}^{5}He + {}^{4}He + 14.17\ \text{MeV};\ {}^{5}He \rightarrow {}^{4}He \rightarrow n + 0.96\ MeV \end{cases} \tag{2.9}$$

Nowadays, various types of accelerators have been developed to produce neutron sources [50], including neutron generators, cyclotrons, electron linear accelerators, electrostatic accelerators, proton and deuteron radiofrequency quadrupoles and linacs, Laser-driven neutron sources, and spallation neutron sources. CANS facilities in the world are listed in Figure 2.4 [19]. Until now, there are 578 facilities in the world.

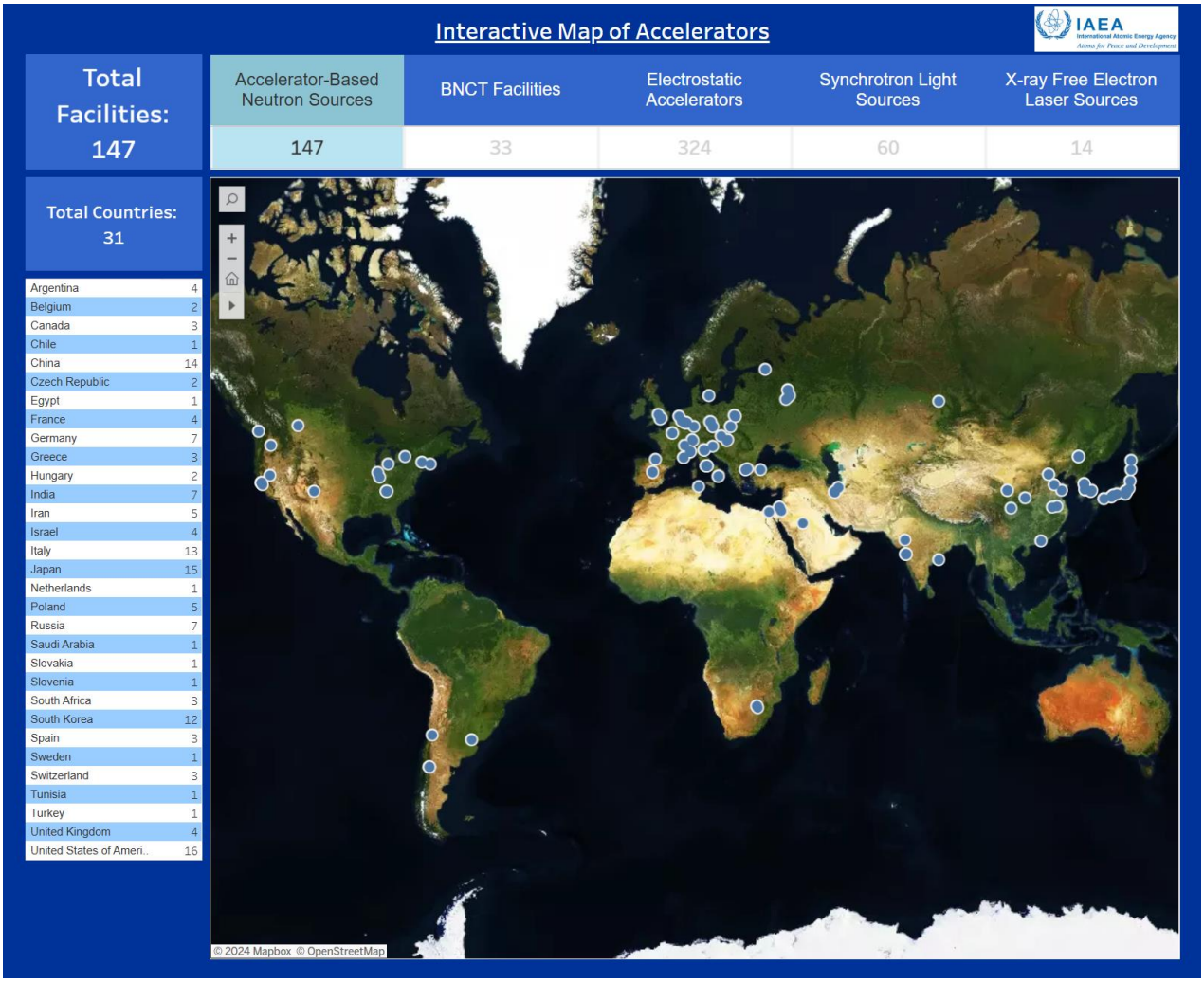

Figure 2.4. Accelerator-based neutron sources in the world [19].

Neutron generators are the smallest and simplest accelerator-based neutron production devices based on D-D and D-T reactions. Cyclotrons can accelerate proton beams from MeV to GeV and metal ions using an RF modulated electric field while being held within a static magnetic field. Electrostatic accelerators generate high voltages based around the principles of the Cockcroft–Walton voltage multiplier or Vande Graaff generators. The Tandem-Electrostatic-Quadrupole (TESQ) and the vacuum insulated tandem accelerator (VITA) are new designs of electrostatic accelerator dedicated to neutron production. RF based linac is the most prevalent and efficient technique for the acceleration of electrons (typically 4-30 MeV) to generate Bremsstrahlung photons to produce (γ,n) neutrons via ^{2}D, ^{6}Li, ^{7}Li, ^{9}Be, ^{13}C, $^{206\text{-}208}$Pb, ^{181}Ta, $^{180, 182, 183, 184,186}$ W targets. Proton and deuteron radiofrequency quadrupoles and linacs (maximum beam current: ~100 mA protons or deuterons) combine a Radio Frequency Quadrupole (RFQ) injector coupled to a Drift Tube (DTL) or a SuperConducting (SCL)

linac. Laser-driven neutron sources generate ultra-intense lasers to accelerate short and intense bursts of ion bunches to generate a very compact and bright source of neutrons exceeding 100 MeV. Spallation neutron sources use a process sending high-energy ions into a metal target to produce the most intense accelerator-based neutron sources and the brightest neutron sources in the world.

2.4 Gamma-ray source

Gamma-rays are the most energetic photons with energies ranging from 100 keV to several MeV. Gamma-ray sources are widely used in a wide range of applications, from diagnosing and treating diseases to inspecting infrastructure and studying nuclear processes.

2.4.1 Isotope gamma-ray source

Most standard isotope gamma-ray sources do not occur in nature because their half-lives are small compared with geological time. Isotope gamma-ray sources emit gamma-rays by nuclear decay, and the radioactivity of a standard isotope gamma-ray source, A(t), at time t can be calculated as:

$$A(t) = A(0) \cdot e^{-\frac{\ln(2)}{T_{1/2}}t} \tag{2.10}$$

where A(0) is the initial source radioactivity and $T_{1/2}$ is the half-life. Isotope gamma-ray sources must be produced from naturally occurring nuclides by a reactor or cyclotron. The commonly used standard isotope gamma-ray sources [45] [51] [52] are listed in Table 2.3.

Table 2.3. Commonly used standard isotope gamma-ray sources [45] [51] [52].

Isotope	Half-life	Characteristic gamma-ray energy (MeV)
^{22}Na	2.60 y	0.511, 1.275
^{54}Mn	312 d	0.835
^{60}Co	5.26 y	1.173, 1.332
^{65}Zn	244d	1.116
^{75}Se	120 d	0.136, 0.265, 0.280, 0.401
^{88}Y	107 d	0.898, 1.836
^{124}Sb	60 d	0.121, 0.603, 0.723, 1.691, 2.091
^{133}Ba	10.4 y	0.081, 0.276, 0.303, 0.356, 0.384
^{137}Cs	30.0 y	0.662
^{152}Eu	13.54	0.122, 0.344, 0.778, 0.964, 1.085, 1.112, 1.408
^{192}Ir	74 d	0.296, 0.308, 0.316, 0.468
^{203}Hg	46 d	0.279

2.4.2 Bremsstrahlung gamma-ray source

Bremsstrahlung [53] is generated when an electron passes through the vicinity of the nucleus of an atom, as shown in Figure 2.5 [54]. The Coulomb force of the nucleus deflects the electrons, and the lost “braking energy” is emitted as a high-energy photon due to energy conservation. If the electron comes to a total stop, all its energy is converted into photon energy. Bremsstrahlung sources are usually generated by focusing a laser directly onto a high-Z solid thick material to increase the conversion efficiency and maximize the number of interactions between the electrons and the nuclei. Through laser wakefield acceleration, a high-intensity laser is focused onto a gas jet to produce a high-energy electron beam in a very low divergence. Thus, a high energy (MeV-level) bremsstrahlung gamma-ray source is produced in low divergence.

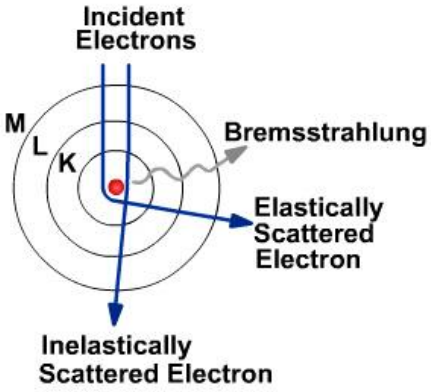

Figure 2.5 [54]. Bremsstrahlung radiation of electron.

2.4.3 Compton gamma-ray source

Multi-MeV and high-brilliance gamma-rays can be produced by Compton scattering based on the collision between a laser wakefield accelerated electron beam and another counter-propagating laser pulse or a reflected laser pulse by a plasma mirror [55]. A schematic of generating a Compton gamma-ray source is shown in Figure 2.6 [56]. When the gamma-ray energy is high compared to the binding energy of the electron in an atom, the electrons can be considered as free particles [57]. The inelastic scattering of the gamma-ray by the electrons is called Compton effect. The energy of the Compton gamma-ray is given by:

$$E'_\gamma = \frac{E_\gamma}{1+\frac{E_\gamma}{m_0c^2}(1-\cos\theta)} \tag{2.11}$$

where m_0c^2 is the rest mass of the electron and θ is the scattering angle between the incident and the scattered gamma-ray.

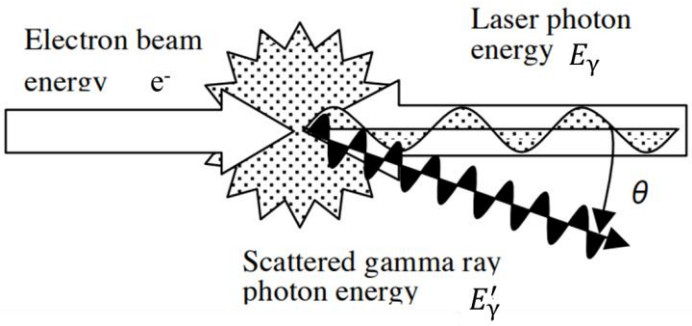

Figure 2.6 [56]. Generation of laser Compton gamma-ray.

2.4.4 Synchrotron radiation light source

Synchrotron radiation is an electromagnetic wave emitted from relativistic charged particles, e.g. electrons and positrons, traveling radically in a storage ring linked to a booster cyclotron, as shown in Figure 2.7 [58]. The radiation is vertically collimated and polarized. Synchrotron radiation is characterized by high brightness, high intensity, and variable polarization. Synchrotron radiation is usually several orders of magnitude brighter than other gamma-ray sources.

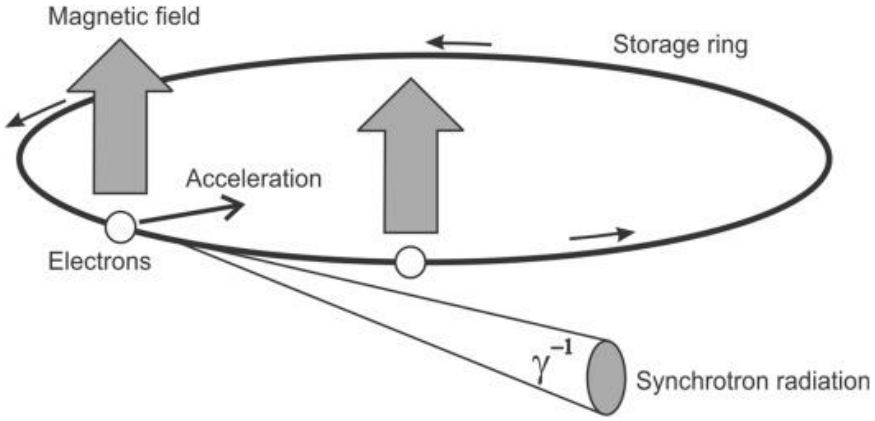

Figure 2.7 [58]. Schematic of Synchrotron radiation.

2.5 Radio-photoluminescence glass dosimeter (RPLGD)

RPLGDs have been widely used for gamma-ray dosimetry due to their advantages of no fading effect and repeatable readout. When the silver-activated phosphate material inside a RPLGD is exposed to ionization radiation, color centers are formed, and fluorescence lights are emitted from the color centers upon irradiation with an ultraviolet laser. This process is known as the radio-photoluminescence phenomena.

The GD-301 (AGC Techno Glass Co., Ltd. [59]) is a type of RPLGD, with an energy measurement range of 15 keV to 20 MeV and a dose measurement range of 10 μGy to 10 Gy for gamma-rays. A photograph of the GD-301 and its holder is shown in Figure 2.8. The size of the GD-301 is Φ 1.5 mm × 8.5 mm, and the active readout volume is Φ 1 mm × 6 mm. The GD-301 is enclosed in a 0.3 mm thick plastic holder (Φ 1.4 mm × 9.5 mm). The weight composition of the GD-301 (ρ = 2.61 g/cm^3) is O (51.16%), Na (11.00%), Al (6.12%), P (31.55%), and Ag (0.17%).

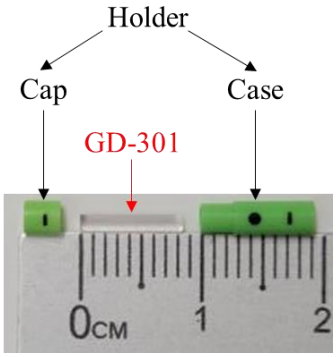

Figure 2.8. Schematic of the GD-301 and its plastic holder.

The gamma-ray dose reading of the GD-301 is performed using a reader, the FGD-1000 (AGC Techno Glass Co., Ltd.), as shown in Figure 2.9. The FGD-1000 can operate ultraviolet pulsed laser for dose reading of the GD-301. The dose calibration of the FGD-1000 is automatically performed via mode-3 [59] under standard ^{137}Cs irradiation. The gamma-ray dose, $D_{\gamma_{air}}$, calculated by the FGD-1000, is given by:

$$D_{\gamma} = \frac{D_{\gamma}\,(^{137}Cs)}{D_{glass}\,(^{137}Cs)} \cdot D_{glass} = \eta\,(^{137}Cs) \cdot D_{glass} \tag{2.12}$$

where $D_{\gamma}\,(^{137}Cs)$ is the gamma-ray dose under standard ^{137}Cs irradiation, $D_{glass}\,(^{137}Cs)$ is the gamma-ray absorbed dose of the GD-301 under standard ^{137}Cs irradiation, D_{glass} is the absorbed dose of the GD-301 read by the FGD-1000, and $\eta\,(^{137}Cs)$ = 1.2 is the built-in conversion coefficient for mode-3.

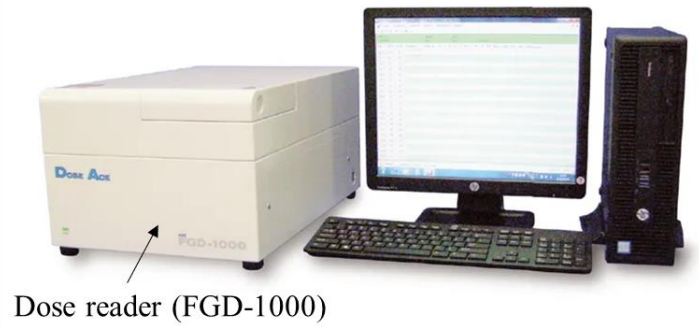

Figure 2.9. Schematic of FGD-1000 dosimerty system.

The small size of the GD-301 is convenient for redevelopment with filters, enhancing the energy measurement range and dose measurement accuracy. Currently, our group has developed a special filter for the GD-301 to measure gamma-ray dose in a high-energy gamma-ray field. The design of the filter is shown in Figure 2.10. The 1 mm thick filter is composed of C, Ni, W materials, and Ti (30%)-Al (70%) alloys. In Figure 2.11, the dose response of the GD-301 covered with the filter exhibits good agreement with air kerma coefficient [60]. The filters for neutron and gamma-ray dose measurement are still under development for validation by the standard n-γ mixed fields designed in this dissertation.

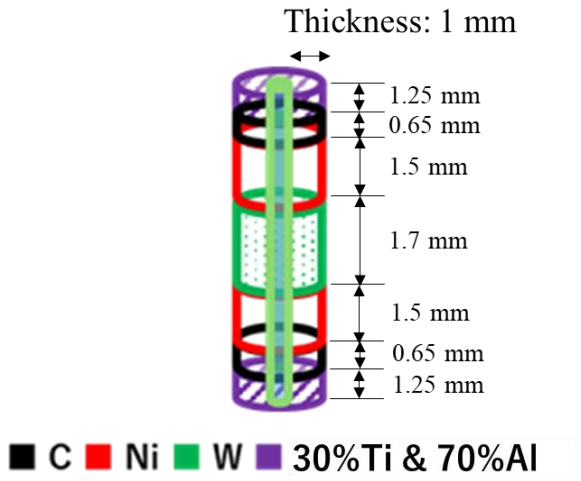

Figure 2.10. Design of filter.

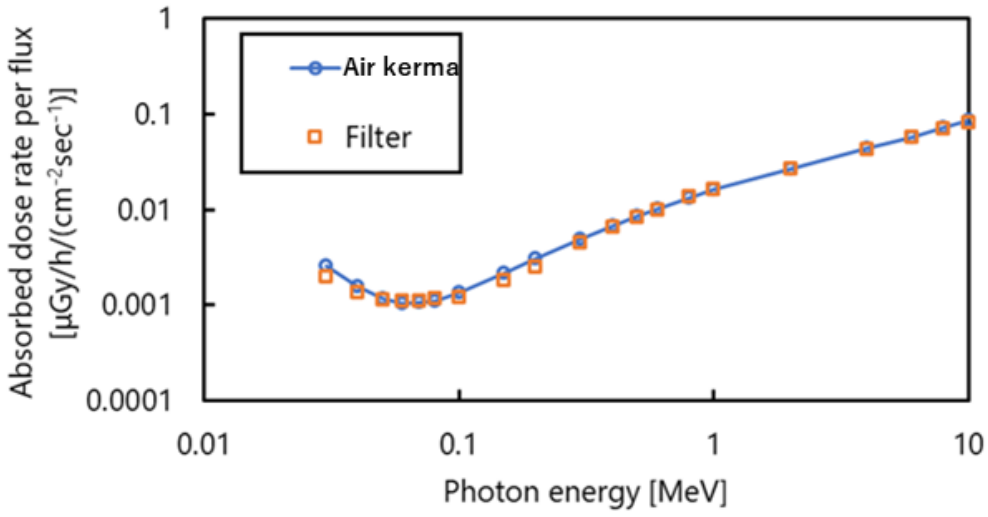

Figure 2.11. Comparison of filter response and air kerma coefficient.

2.6 Monte Carlo method

Monte Carlo [61] is a computational technique based on constructing a random process for a problem and carrying out a numerical experiment by N-fold sampling from a random sequence of numbers with a prescribed probability distribution, as defined by x-random variable, x_i:

$$\hat{x} = \frac{1}{N}\sum_{i=1}^{N} x_i \tag{2.13}$$

where $\hat{x}$ is the estimated or sample mean off x. If a problem can be given a probabilistic interpretation, then it can be modeled using random numbers.

Monte Carlo is widely used for particle transport simulation. In this method, particles are distributed randomly in a volume and the interaction energy of the particles is calculated. If the energy fulfils certain criteria, the constellation is accepted as the next step in the evolution of the system. Then a new distribution is generated, and the procedure is repeated.

2.6.1 MCNP

The Monte Carlo N-Particle code (MCNP) [62] is developed and released by Los Alamos National Laboratory, USA. MCNP can be used for general-purpose transport of many particles including neutrons, photons, electrons, ions, many other elementary particles, and coupled particles transport up to 1 TeV/nucleon. The transport of these particles is through a three-dimensional representation of materials defined in a constructive solid geometry, bounded by first-, second-, and fourth-degree user-defined surfaces. In addition, external structured and unstructured meshes can be used to define the problem geometry in a hybrid mode by embedding a mesh within a constructive solid geometry cell, providing an alternate path to defining complex geometry. The application areas that use the predictions of the MCNP include (but are not limited to): radiation protection and dosimetry, radiation shielding, radiography, medical physics, nuclear criticality safety, critical and subcritical experiment design and analysis, detector design and analysis, nuclear oil-well logging, accelerator target design, fission and fusion reactor design, decontamination and decommissioning, and nuclear safeguards and nonproliferation.

2.6.2 PHITS

Particle and Heavy Ion Transport code System (PHITS) [63] is a general Monte Carlo particle

transport simulation code developed under collaboration between Japan Atomic Energy Agency (JAEA), Research Organization for Information Science and Technology (RIST), High Energy Accelerator Research (KEK), and several other institutes. It can deal with the transport of all particles, e.g. neutron, photon, ions, electron, proton, etc. from 10^{-4} eV to 1 TeV, using several nuclear reaction models and nuclear data libraries. PHITS can support research in the fields of accelerator technology, radiotherapy, space radiation, and in many other fields which are related to particle and heavy ion transport phenomena.

Chapter 3. Design of n-γ mixed fields using various moderator assemblies with a D-D neutron source

3.1 Objective

In this dissertation, to validate the material-filtered RPLGD for BNCT, various types of n-γ mixed fields were designed using a D-D neutron source at OKTAVIAN, Osaka University. The energy of a D-D neutron source can cover the average energy of a p-Li neutron source and a p-Be neutron source for BNCT.

In a n-γ mixed field, the neutron components are classified into three energy groups: (1) fast neutron (0.01-2.5 MeV), (2) epi-thermal neutron (5×10^{-7}-0.01 MeV), and (3) thermal neutron (< 5×10^{-7} MeV). The proportions of fast neutron dose, D_{fast}, epithermal neutron dose, D_{epi}, and thermal neutron dose, $D_{thermal}$, are calculated respectively as:

$$\begin{cases} Proportion\ of\ fast\ neutron\ dose = D_{fast}/D_n \\ Proportion\ of\ epithermal\ neutron\ dose = D_{epi}/D_n \\ Proportion\ of\ thermal\ neutron\ dose = D_{thermal}/D_n \end{cases} \quad (3.1)$$

where D_n is the total neutron dose. Therefore, n-γ mixed fields are classified into three types and the performance of the moderator assemblies should follow: (1) fast-neutron (F) -dominated field (D_{fast}/D_n > 70%), (2) epithermal-neutron (E) -dominated field (D_{epi}/D_n > 70%), (3) thermal-neutron (T) -dominated field ($D_{thermal}/D_n$ > 70%). In a n-γ mixed field, the ratio of gamma-ray dose, D_γ, to neutron dose, D_n, and the ratio of gamma-ray dose, D_γ, to total dose, $D_{\gamma+n}$, are calculated respectively as:

$$\begin{cases} Ratio\ of\ gamma-ray\ dose\ to\ neutron\ dose = D_\gamma/D_n \\ Ratio\ of\ gamma-ray\ dose\ to\ total\ dose = D_\gamma/D_{\gamma+n} \end{cases} \quad (3.2)$$

The moderator assemblies are designed to produce D_γ/D_n ≈ 5-900% ($D_\gamma/D_{\gamma+n}$ ≈ 5-90%). If D_γ/D_n ≤ 1%, the n-γ mixed field is defined as a neutron-only field. If D_γ/D_n ≥ 10000% (D_n/D_γ ≤ 1%), the n-γ mixed field is defined as a gamma-ray-only field.

3.2 Materials and methods

3.2.1 Moderator assembly

In Figure 3.1, different moderator assemblies are designed to generate n-γ mixed fields with a

2.5 MeV D-D neutron source. These moderator assemblies (diameter: 40 cm; thickness: 16-80.5 cm) were designed with multi-layer materials to adjust D_γ / D_n for different types n-γ mixed fields, by changing the combination and thickness of the materials.

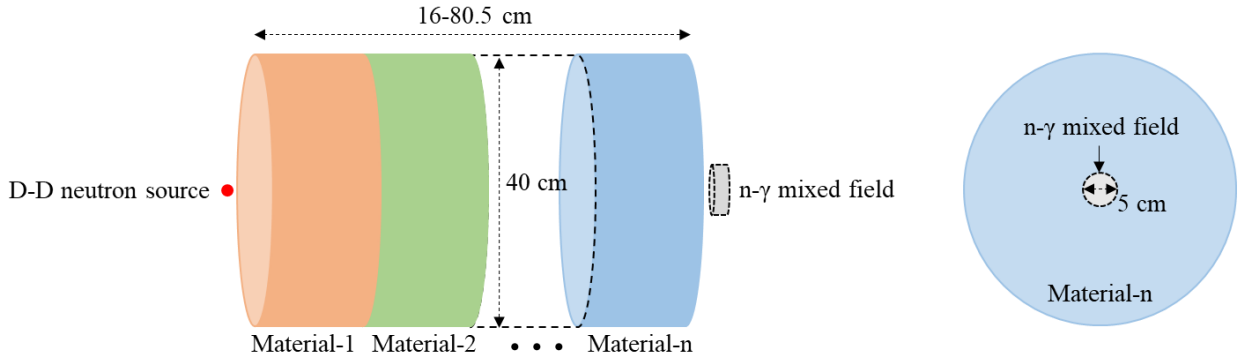

(a). Horizontal view (b). Sectional view

Figure 3.1. Moderator assembly for n-γ mixed field.

In this chapter, simulations are performed by Monte Carlo N-particle Code 5 (MCNP5) [64] based on ENDF/B-VIII.0 [65]. The neutron source is set to an isotropic point source (2.5 MeV, NPS: 1×10^9) ideally. Radiation doses and fluxes are calculated by F6 tally and F4 tally, respectively.

For the moderator assembly, 22 commonly used materials were considered as candidates.

For F-dominated fields, 10 common metal materials, i.e. Li (ρ = 0.53 g/cm^3), Mg (ρ = 1.74 g/cm^3), Al (ρ = 2.70 g/cm^3), Ti (ρ = 4.50 g/cm^3), Fe (ρ = 7.86 g/cm^3), Ni (ρ = 8.90 g/cm^3), Cu (ρ = 8.96 g/cm^3), W (ρ = 19.25 g/cm^3), Pb (ρ = 11.34 g/cm^3), Bi (ρ = 9.78 g/cm^3), were considered for three reasons as follows: (i) these metal materials have relatively small (n,n) cross sections to moderate D-D neutrons and maintain fast neutron dominance; (ii) most of these metal materials produce high energy characteristic gamma-rays based on the (n,γ) reaction [66]; (iii) their atomic numbers are relatively high to shield the target gamma-rays.

As shown in Figure 3.2, D_{fast} / D_n and D_γ / D_n for these materials were calculated by increasing the material thickness from 10 cm to 50 cm. In Figure 3.2 (a), these 10 materials produce low thermal and epithermal dose during moderation for generating F-dominated fields. In Figure 3.2 (b), as the material thicknesses increase, D_γ / D_n of Li and W exhibit a clear rising trend; Fe and Ni exhibit their ability of enhancing D_γ / D_n with thin thickness; Pb and Bi exhibit the best performance to suppress

D_γ / D_n to below 5%.

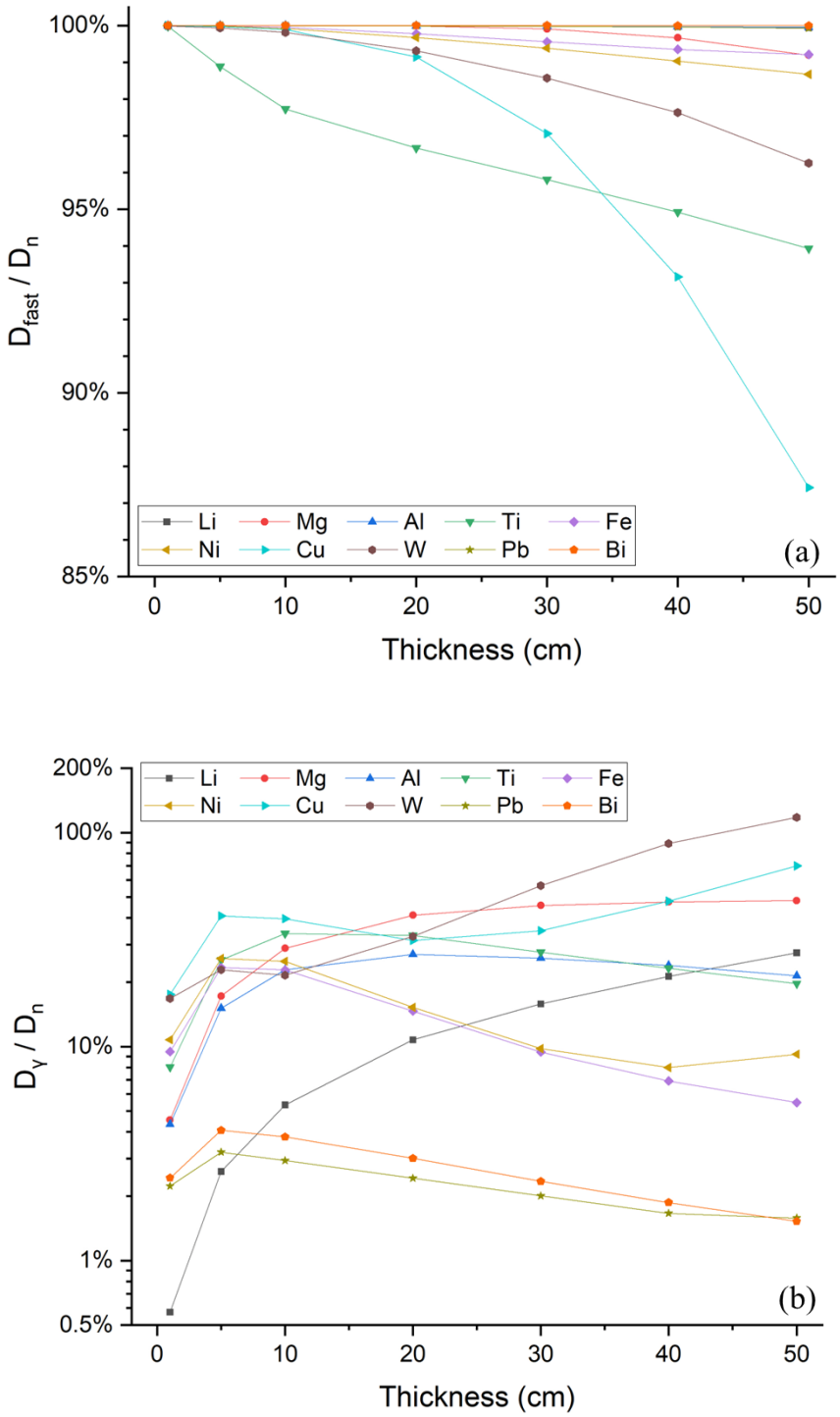

Figure 3.2. (a) D_{fast} / D_n and (b) D_γ / D_n of Li, Mg, Al, Ti, Fe, Ni, Cu, W, Pb, and Bi materials.

Currently, moderate weight elements e.g. Li, C, O, F, Mg, Al, Ca, and Ti, in the form of ceramics have been widely proposed and used in BSA design of BNCT to produce epithermal neutrons.

Fluorides and oxides are effective materials to convert fast neutrons into epithermal neutrons, because the threshold energy of the (n,n') reaction is low [16]. Therefore, nine fluoride and oxide materials were examined by increasing the material thickness from 10 cm to 100 cm, including LiF (ρ = 2.64 g/cm^3), Li_2CO_3 (ρ = 2.11 g/cm^3), CF_2 (ρ = 2.20 g/cm^3), MgF_2 (ρ = 3.15 g/cm^3), MgO (ρ = 3.60 g/cm^3), AlF_3 (ρ = 2.88 g/cm^3), Al_2O_3 (ρ = 3.99 g/cm^3), CaF_2 (ρ = 3.18 g/cm^3), TiF_3 (ρ = 3.40 g/cm^3).

The results of D_{epi} / D_n and D_γ / D_n are shown in Figure 3.3. In Figure 3.3 (a), as the material thickness is from 10 cm to 50 cm, TiF_3 and MgF_2 exhibit the best performance to enhance D_{epi}/D_n. In Figure 3.3 (b), TiF_3 exhibits the strongest ability to enhance D_γ / D_n from 37.3% to 648.5% due to the large (n,γ) cross sections of Ti, while Li_2CO_3 produces the lowest D_γ / D_n below 11.8% due to the low (n,γ) cross sections of Li. LiF, CF_2, MgF_2, and Al_2O_3 exhibit the ability to adjust D_γ / D_n, because they can enhance or suppress D_γ / D_n as the material thickness is from 30 cm to 90 cm.

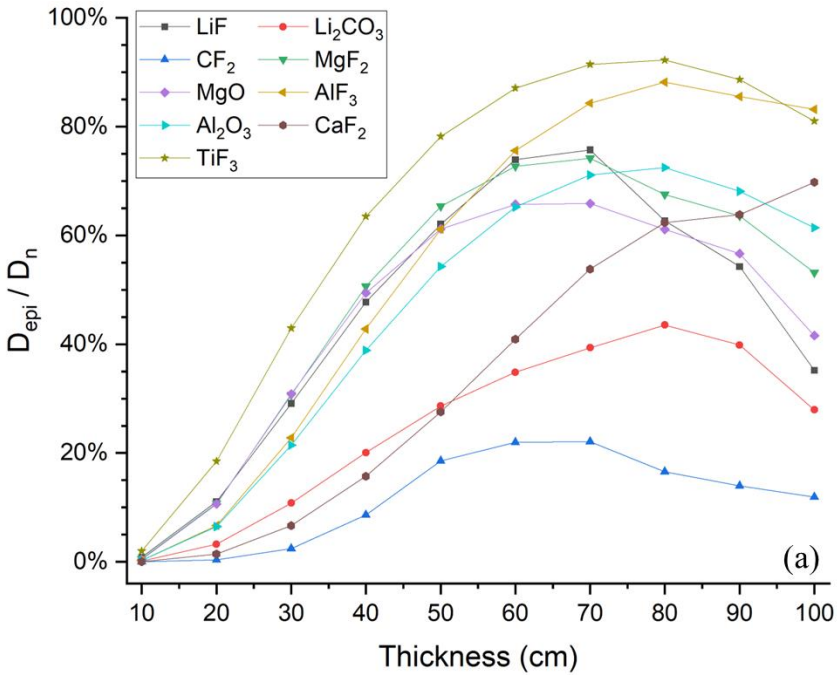

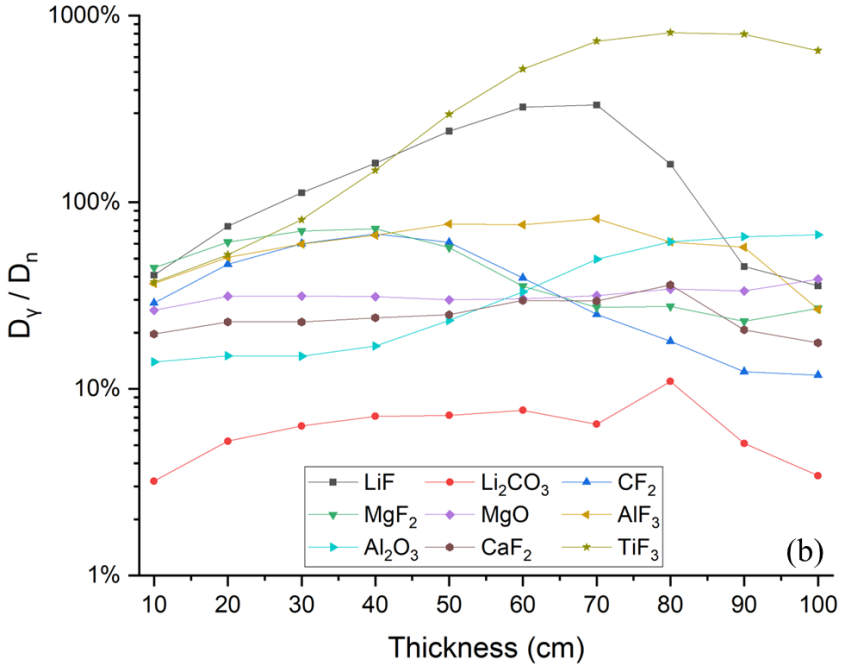

Figure 3.3. (a) D_{epi} / D_n and (b) D_γ / D_n of fluoride and oxide materials.

Graphite (C, ρ = 2.27 g/cm^3), polyethylene (PE, ρ = 0.93 g/cm^3), and water (H_2O, 1.00 g/cm^3) are commonly used materials to produce thermal neutrons due to the large (n,n) cross sections of H and C. These three materials were examined by increasing the material thickness from 10 cm to 50 cm.

The results of $D_{thermal}$ / D_n and D_γ / D_n are shown in Figure 3.4. In Figure 3.4 (a), PE exhibits the best performance which produces the highest D_γ / D_n with the material thickness from 10 cm to 70 cm. All these materials can produce $D_{thermal}$ / D_n exceeding 70%. In Figure 3.4 (b), PE and H_2O have large gamma-ray dose production that can enhance D_γ / D_n from below 100% to exceeding 10000% due to the large (n,γ) cross sections of H, while C produces D_γ / D_n below 10% with low gamma-ray dose production due to the low (n,γ) cross sections of C.

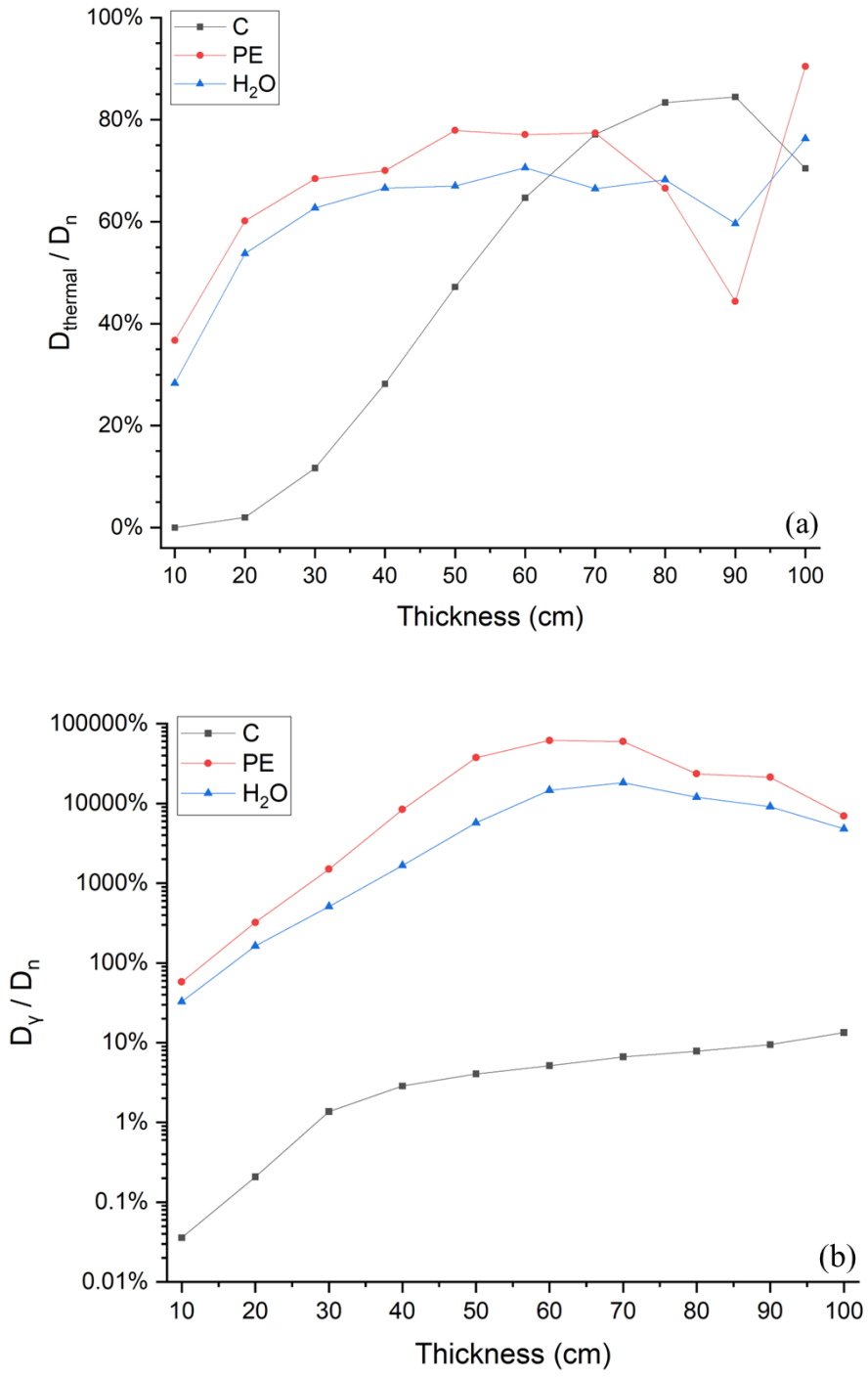

Figure 3.4. (a) $D_{thermal}$ / D_n and (b) D_γ / D_n of C (Graphite), PE, and H_2O.

3.2.2 Target gamma-ray

D-D neutrons are produced at a deuteron-loaded neutron-generating target bombarded by accelerated deuteron beams, where interactions occur inevitably between the produced neutrons and the structure materials of the beam tube and the neutron-generating target. Consequently, secondary gamma-rays (hereafter called target gamma-ray in Chapter 3) are generated unavoidably. The target

gamma-ray dose is a significant dose component [67] that can affect the readings of dosimeters [68]. If the target gamma-ray dose is comparable to the gamma-ray dose produced by the moderator assembly, it may cause large errors in gamma-ray dose measurement.

The target assembly model of the OKTAVIAN facility [33] is shown in Figure 3.5. This target assembly includes a titanium-based deuterium target (0.01 cm), a copper cooling jacket (0.1 cm), a cooling water layer (0.24 cm), and a stainless steel (304) case (0.1 cm). The spectrum of the target gamma-rays at 1 cm distance to source is shown in Figure 3.6. The target gamma-rays are produced up to 12 MeV by nuclear reactions of the source neutrons with H, C, O, Si, P, S, Ti, Cr, Mn, Fe, Ni, and Cu elements of the target assembly.

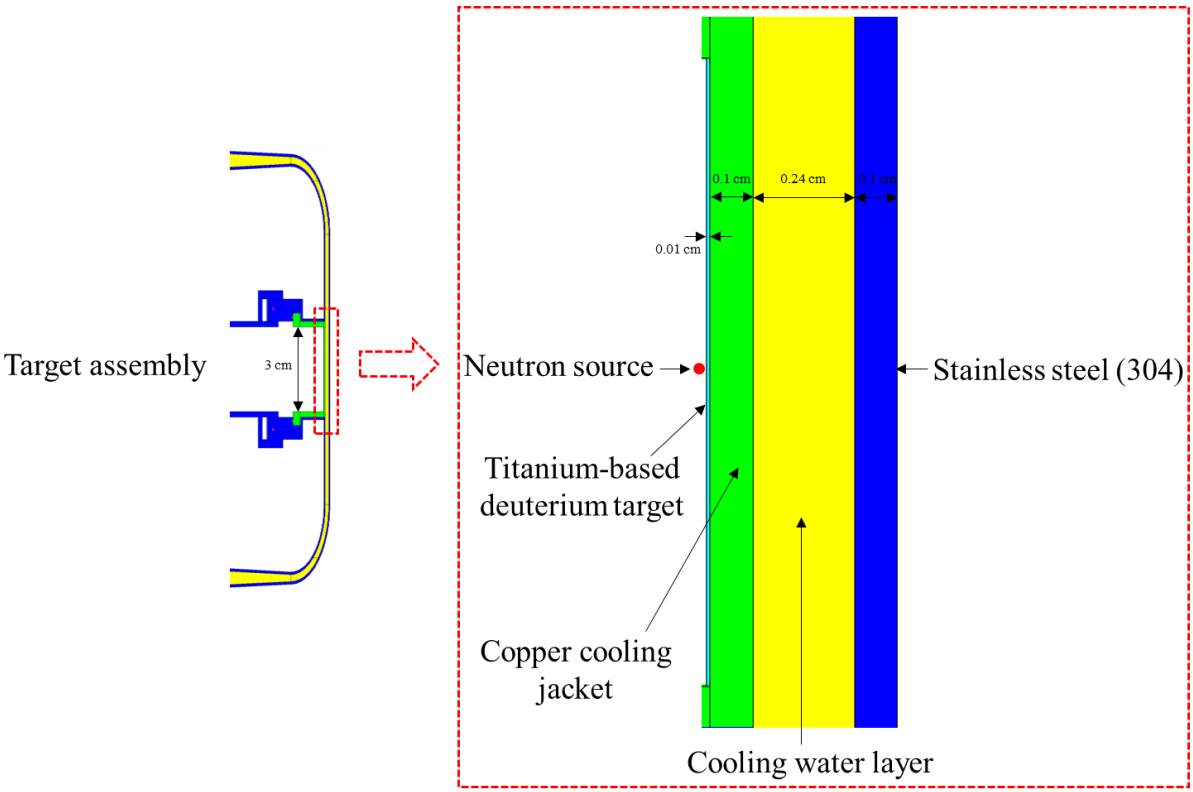

Figure 3.5. Target assembly model of OKTAVIAN facility.

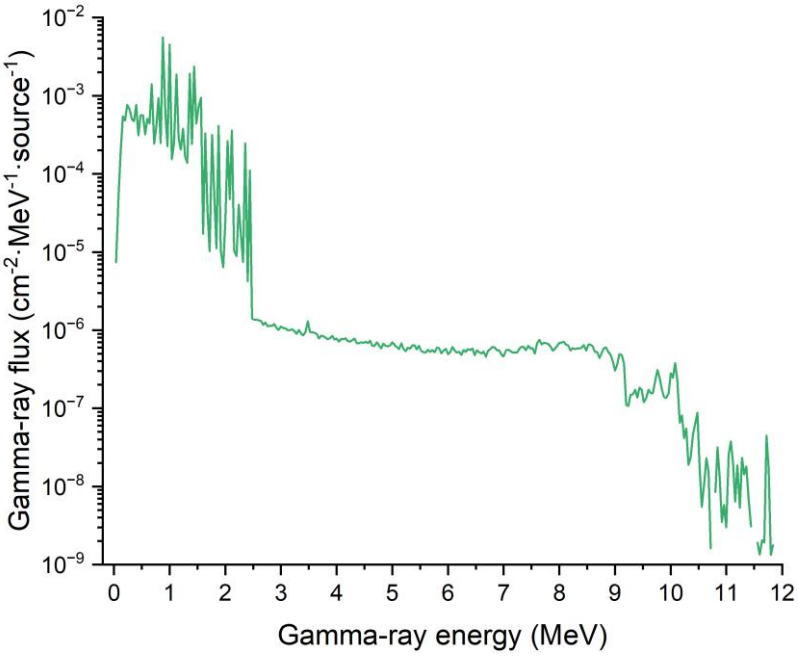

Figure 3.6. Spectrum of the target gamma-rays (1 cm distance to source).

To analyze the effect of the target gamma-rays, the target gamma-ray dose, $D_{\gamma_{target}}$, and the incident neutron dose, D_n', were calculated at different locations (distance of the measurement point to the source: 1-100 cm). The results of $D_{\gamma_{target}}$ and D_n' are shown in Figure 3.7. The proportion of $D_{\gamma_{target}}$ to D_n' is 5.5-7.1%, indicating that the target gamma-ray dose should not be negligible. Hence, the moderator assemblies should be able to remove the target gamma-ray dose. $\eta_{\gamma_{target}}$ is defined to evaluate the ability of a moderator assembly to remove the target gamma-ray dose:

$$\eta_{\gamma_{target}} = \frac{D_{\gamma_{target}}}{D_{\gamma_{total}}}, \tag{3.3}$$

where $D_{\gamma_{total}}$ is the total gamma-ray dose generated by the target assembly and the moderator assembly. Theoretically, if $\eta_{\gamma_{target}}$ = 0%, the target gamma-ray dose is completely removed by the moderator assembly, meaning that the gamma-ray component in a n-γ mixed field purely originates from the moderator assembly. For a shielding material, the attenuation of the target gamma-rays is described by [69]:

$$I = I_0 \cdot e^{-\mu_{total} \cdot \rho \cdot t} \tag{3.4}$$

where I is the gamma-ray intensity after attenuation, I_0 is the incident density of the target gamma-

rays, μ_{total} is the total mass absorption coefficient of each material, ρ is the density of the material, and t is the thickness of the material.

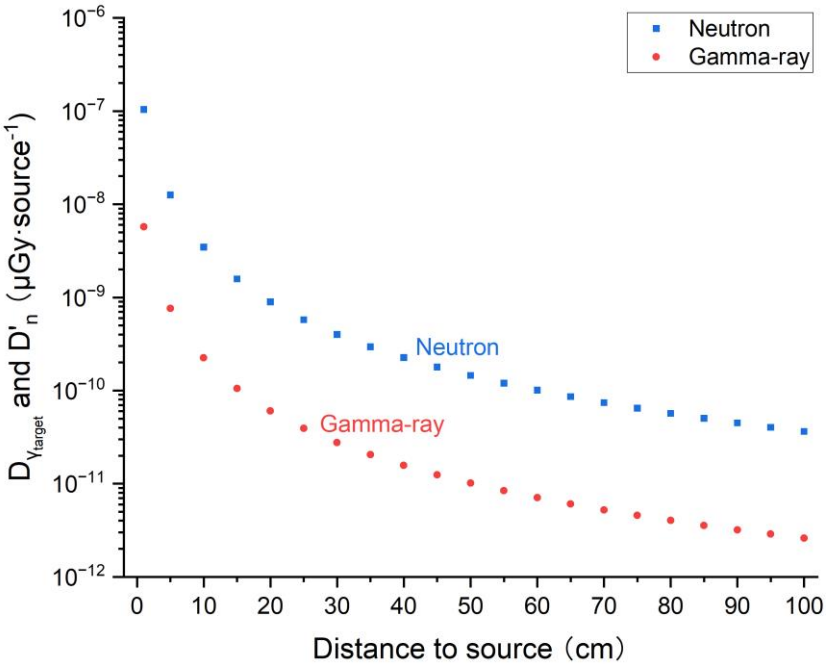

Figure 3.7. $D_{\gamma_{target}}$ and D_n' at 1-100 cm to source.

Fe, W, Pb, and Bi, were considered as shielding materials due to their large $\mu_{total} \cdot \rho$ [70] . $\mu_{total} \cdot \rho$ of Fe, W, Pb, and Bi are shown in Figure 3.8. The attenuation abilities of Fe, W, Pb, and Bi were calculated to determine the minimum thickness of each material to remove the target gamma-ray dose, as shown in Figure 3.9. In Figure 3.9 (a), as the material thickness increases from 1 cm to 20 cm, the target gamma-ray dose, $D_{\gamma_{target}}$, is attenuated by Fe, W, Pb, and Bi effectively, compared to $D_{\gamma_{target}}$ in Figure 3.7. In Figure 3.9 (b), the minimum thicknesses of Fe, W, Pb, and Bi to remove the target gamma-ray dose are determined as 16 cm Fe ($\eta_{\gamma_{target}}$ = 0.9%), 5 cm W ($\eta_{\gamma_{target}}$ = 0.6%), 11 cm Pb ($\eta_{\gamma_{target}}$ = 0.8%), and 12 cm Bi ($\eta_{\gamma_{target}}$ = 0.9%).

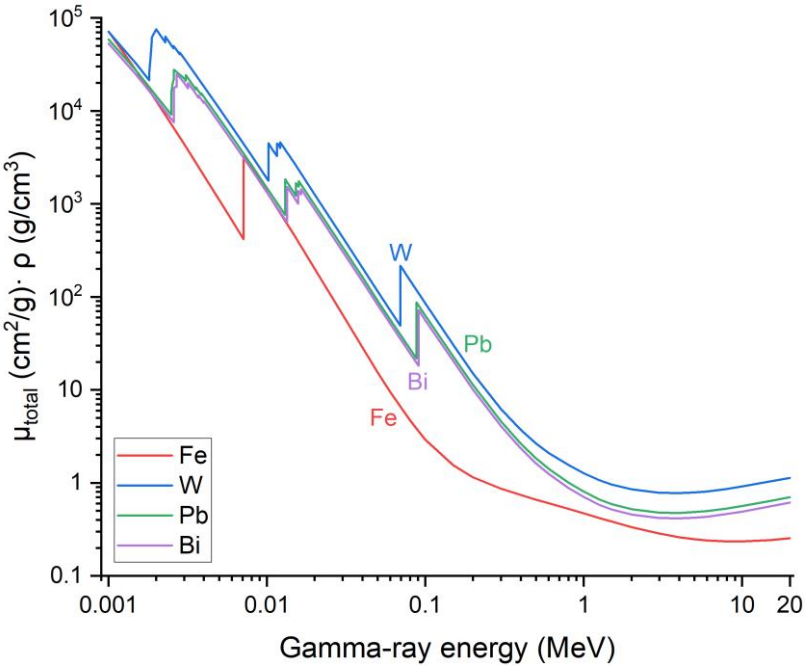

Figure 3.8. $\mu_{total} \cdot \rho$ of Fe, W, Pb, and Bi.

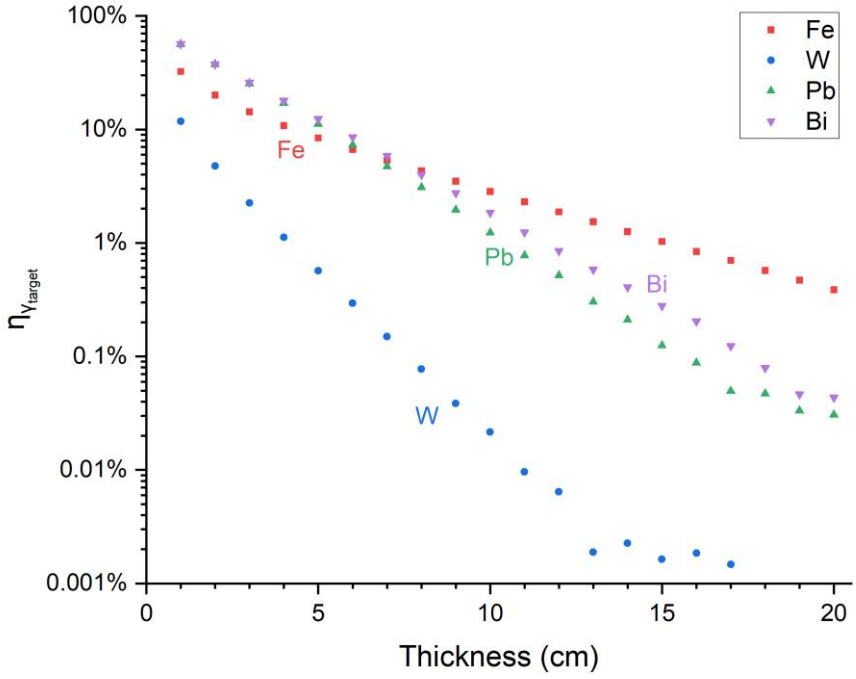

Figure 3.9. (a) $D_{\gamma_{target}}$ attenuated by Fe, W, Pb, and Bi; (b) $\eta_{\gamma_{target}}$ of Fe, W, Pb, and Bi.

3.3 Characteristics of mixed field

3.3.1 F-dominated field

According to the results in Figure 3.2 and 3.9, Fe and PE were selected for F-dominated fields, since PE can produce high D_γ/D_n via the $^{1}H(n,\gamma)^{2}H$ reaction and Fe can absorb the thermal neutrons moderated PE and produce high-energy gamma-rays via $^{56}Fe(n,\gamma)^{57}Fe$, $^{57}Fe(n,\gamma)^{58}Fe$, $^{54}Fe(n,\gamma)^{55}Fe$ reactions [66] [71].

F-dominated fields were generated using "Fe 16 cm", "PE 1-31 cm + Fe 16 cm", and "Fe 16 cm + Pb 1-28 cm", and the results are summarized in Table 3.1. In the F-dominated fields, D_γ/D_n is 1.0-977.7% ($D_\gamma/D_{\gamma+n}$ = 1.0-90.7%) and D_{fast}/D_n is 98.4-100.0%. 16 cm Fe is used to remove the target gamma-ray dose and produce high energy gamma-rays. To enhance D_γ/D_n, 1-31 cm PE is used to generate extra gamma-ray dose and 16 cm Fe can absorb the thermal neutrons moderated by PE. For "PE 1-31 cm + Fe 16 cm", D_γ/D_n is provided from 18.0% to 977.0%. To reduce D_γ/D_n, as 1 cm Pb is attached with 16 cm Fe, gamma-rays are absorbed effectively and D_γ/D_n decreases to 5.9%. As the thickness of Pb increases to 28 cm, a neutron-only field (D_γ/D_n = 0.99%) is achieved.

Table 3.1. Characteristics of F-dominated fields.

Material	Dose (μGy·source^{-1})		D_γ/D_n	$D_\gamma/D_{\gamma+n}$	D_{fast}/D_n
	D_γ	D_n			
Fe 16 cm	7.84×10^{-11}	4.38×10^{-10}	17.9%	15.2%	99.997%
PE + Fe 1-31 cm + 16 cm	7.17×10^{-11} - 1.13×10^{-12}	3.95×10^{-10} - 1.50×10^{-13}	18.0 - 977.0%	15.3 - 90.7%	99.871 - 98.444%
Fe + Pb 16 cm + 1 cm	2.59×10^{-11}	4.41×10^{-10}	5.9%	5.6%	99.997%
Fe + Pb 16 cm + 28 cm	1.86×10^{-13}	1.88×10^{-11}	0.99%	0.98%	99.991%

The neutron and gamma-ray spectra of "Fe 16 cm", "PE 14 cm + Fe 16 cm", "PE 24 cm + Fe 16 cm", and "Fe 16 cm + Pb 28 cm" are shown in Figure 3.10. In Figure 3.10 (a), the neutron energy

range of “Fe 16 cm” is from ~10^{-6} MeV to 2.5 MeV, and the neutron energy ranges of “PE 14 cm + Fe 16 cm” and “PE 24 cm + Fe 16 cm” are extended from ~10^{-8} MeV to 2.5 MeV. Even so, the influence of thermal and epithermal neutron doses is rather small ($D_{thermal}/D_n$ < 0.3%, D_{epi}/D_n < 1.3%). In Figure 3.10 (b), gamma-rays are produced with energy up to 12 MeV with characteristic peaks from 0.9 MeV to 10.04 MeV. For “PE 14 cm + Fe 16 cm” and “PE 24 cm + Fe 16 cm”, peaks in 5-11 MeV become noticeable due to the (n,γ) reaction of Fe, because Fe absorbs a large number of thermal neutrons moderated by PE.

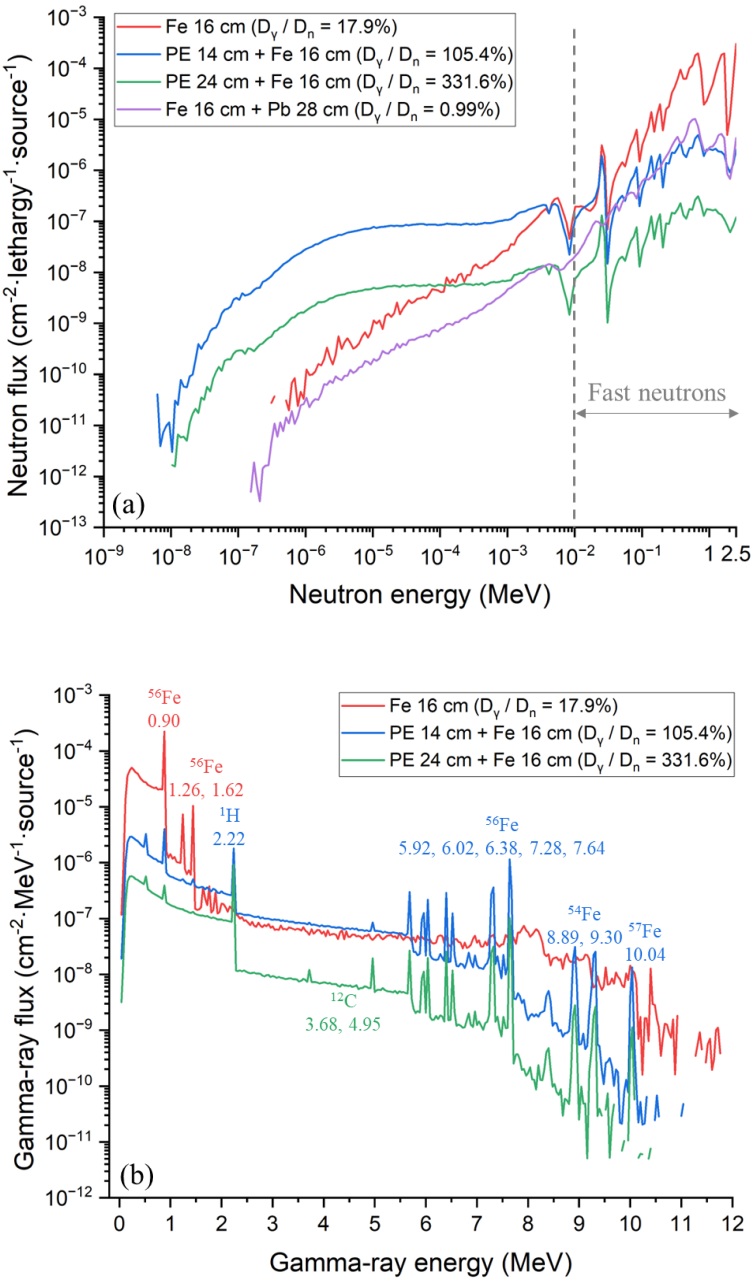

Figure 3.10. Energy spectra of F-dominated fields: (a) Neutron spectra; (b) Gamma-ray spectra.

3.3.2 E-dominated field

According to the results in Figure 3.3 and 3.9, Fe, W, Pb LiF, MgF_2, and TiF_3 were selected for E-dominated fields. The combination of "Heavy material + MgF_2 + thermal neutron absorber" was considered for high D_{epi}/D_n. W and Fe benefit fast neutron moderation due to the relatively large (n,n'γ) cross sections and effectively suppress D_{fast}/D_n. LiF absorbs thermal neutrons to suppress $D_{thermal}/D_n$. TiF_3 can enhance D_γ/D_n effectively. Pb was used as a gamma-ray filter.

E-dominated fields are generated using "W 15 cm + Fe 5 cm + MgF_2 40 cm + LiF 0.5 cm", "W 15 cm + Fe 5 cm + MgF_2 40 cm + TiF_3 1-8 cm + LiF 0.5 cm", and "W 15 cm + Fe 5 cm + MgF_2 40 cm + LiF 0.5 cm + Pb 1-20 cm", and the results are summarized in Table 3.2. In the E-dominated fields, D_γ/D_n is 5.0-921.1% ($D_\gamma/D_{\gamma+n}$ = 4.7-90.2%) and D_{epi}/D_n is 74.0-85.4%. For "W 15 cm + Fe 5 cm + MgF_2 40 cm + 0.5 cm LiF", D_γ/D_n is 112.2% and D_{epi}/D_n is 74.2%. To enhance D_γ/D_n, as 1-8 cm TiF_3 is added, η_d increases from 249.5% to 921.1%. To reduce D_γ/D_n, as 1-20 cm Pb is attached, η_d declines from 65.2% to 5.0%. However, a neutron-only field is difficult to achieve even the thickness of Pb increases, because gamma-rays are absorbed but epithermal neutrons are also scattered due to the large (n,n) cross sections of Pb [40].

Table 3.2. Characteristics of E-dominated fields.

Material	Dose (μGy·source^{-1})		D_γ/D_n	$D_\gamma/D_{\gamma+n}$	D_{epi}/D_n
	D_γ	D_n			
W + Fe + MgF_2 + LiF 15 cm + 5 cm + 40 cm + 0.5 cm	1.29×10^{-13}	1.15×10^{-13}	112.5%	52.9%	74.2%
W + Fe + MgF_2 + TiF_3 + LiF 15 cm + 5 cm + 40 cm + 1-8 cm + 0.5 cm	2.56×10^{-13} - 4.18×10^{-13}	6.43×10^{-14} - 4.54×10^{-14}	249.5% - 921.1%	71.4 - 90.2%	76.4 - 85.4%
W + Fe + MgF_2 + LiF + Pb 15 cm + 5 cm + 40 cm + 0.5 cm + 1-20 cm	6.79×10^{-14} - 6.40×10^{-16}	1.04×10^{-13} - 1.29×10^{-14}	65.2 - 5.0%	39.5 - 4.7%	74.0 - 75.4%

The neutron and gamma-ray spectra of "W 15 cm + Fe 5 cm + MgF_2 40 cm + LiF 0.5 cm", "W 15 cm + Fe 5 cm + MgF_2 40 cm + TiF_3 2 cm + LiF 0.5 cm", and "W 15 cm + Fe 5 cm + MgF_2 40 cm

+ LiF 0.5 cm + Pb 3 cm" are shown in Figure 3.11. In Figure 3.11 (a), thermal and fast neutron spectra are well-shaped, and their influence is acceptable ($D_{thermal}/D_n$ = 9.3-10.1%, D_{fast}/D_n = 12.5-16.3%). In Figure 3.11 (b), gamma-rays are produced up to 12 MeV with characteristic peaks from 0.54 MeV to 10.64 MeV. For "W 15 cm + Fe 5 cm + MgF_2 40 cm + 0.5 cm LiF", peaks in 7-12 MeV are produced via (n,γ) reactions of W, Fe, and Mg [66]. For "W 15 cm + Fe 5 cm + MgF_2 40 cm + TiF_3 2 cm + 0.5 cm LiF", gamma-ray intensity is enhanced due to the large (n,γ) cross sections of Ti [66].

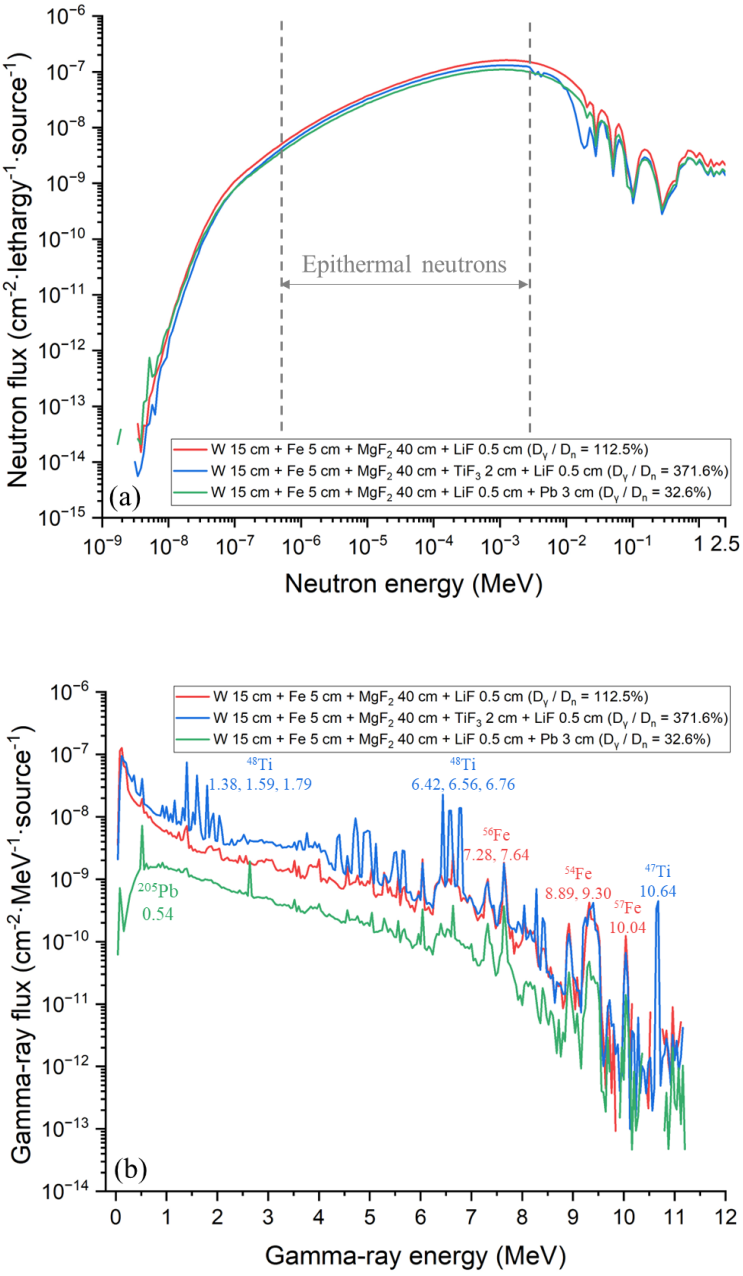

Figure 3.11. Energy spectra of E-dominated fields: (a) Neutron spectra; (b) Gamma-ray spectra.

3.3.3 T-dominated field

According to the results in Figure 3.4 and 3.9, Fe, Pb, Bi, C, and PE were selected for T-dominated fields. Fe was used to produce high-energy gamma-rays. C and PE were used to produce thermal neutrons. Pb and Bi were used as gamma-ray filters.

T-dominated fields are generated using "Fe 16 cm+ C 16-0 cm + PE 5-19 cm", "Fe 16 cm + C 16 cm + PE 5 cm + Pb 1-5 cm", and "C 52 cm + Bi 12 cm", and the results are summarized in Table 3.3. In the T-dominated fields, D_γ/D_n is 0.7-946.3% ($D_\gamma/D_{\gamma+n}$ = 0.7-90.4%) and $D_{thermal}/D_n$ is 90.1-90.8%. The target gamma-ray dose is removed by using 16 cm Fe or 12 cm Bi. C and PE are used to produce thermal neutrons. For "Fe 16 cm + C 16-0 cm + PE 5-19 cm", D_γ/D_n is balanced between 86.9% and 946.3% by the combination of C (low gamma-ray production) and PE (hydrogen rich for high gamma-ray production). To reduce D_γ/D_n, as 1-5 cm Pb is attached to "Fe 16 cm + C 16 cm + PE 5 cm", D_γ/D_n declines from 39.1% to 8.3%. A neutron-only field (D_γ/D_n = 0.7%) is achieved by "C 52 cm + Bi 12 cm". Bi is used because it has lower neutron absorption than Pb [72].

Table 3.3. Characteristics of T-dominated fields.

Material	Dose (μGy·source^{-1})		D_γ/D_n	$D_\gamma/D_{\gamma+n}$	$D_{thermal}/D_n$
	D_γ	D_n			
Fe + C + PE 16 cm + 16-0 cm + 5-19 cm	3.59×10^{-11} - 1.18×10^{-10}	4.30×10^{-11} - 1.13×10^{-11}	86.9 - 946.3%	46.5 - 90.4%	90.6 - 90.1%
Fe + C + PE + Pb 16 cm + 16 cm + 5 cm + 1-5 cm	1.51×10^{-11} - 2.15×10^{-12}	3.87×10^{-11} - 2.58×10^{-11}	39.1 - 8.3%	28.1 - 7.7%	90.5 - 90.8%
C + Bi 52 cm + 12 cm	3.03×10^{-14}	4.11×10^{-12}	0.7%	0.7%	90.7%

The neutron and gamma-ray spectra of "Fe 16 cm + C 16 cm + PE 5 cm", "Fe 16 cm + C 16 cm + PE 5 cm + Pb 2 cm", "Fe 16 cm + C 6 cm + PE 12 cm", and "C 52 cm + Bi 12 cm" are shown in Figure 3.12. In Figure 3.12 (a), even if epithermal and fast neutrons exist, their dose influence is small (D_{epi}/D_n = 0.8-3.7%, D_{fast}/D_n = 5.6-9.1%). In Figure 3.12 (b), gamma-rays are produced up to 11

MeV with characteristic peaks from 0.54 MeV to 10.04 MeV. The characteristic peaks in 5-11 MeV are produced via $^{56}Fe(n,\gamma)^{57}Fe$, $^{57}Fe(n,\gamma)^{58}Fe$, $^{54}Fe(n,\gamma)^{55}Fe$ reactions [66]. For "Fe 16 cm + C 6 cm + PE 12 cm", gamma-ray intensity is enhanced compared to "Fe 16 cm + C 16 cm + PE 5 cm", because the thickness of PE increases from 5 cm to 12 cm and more gamma-rays are produced due to the large (n,γ) cross sections of H [40].

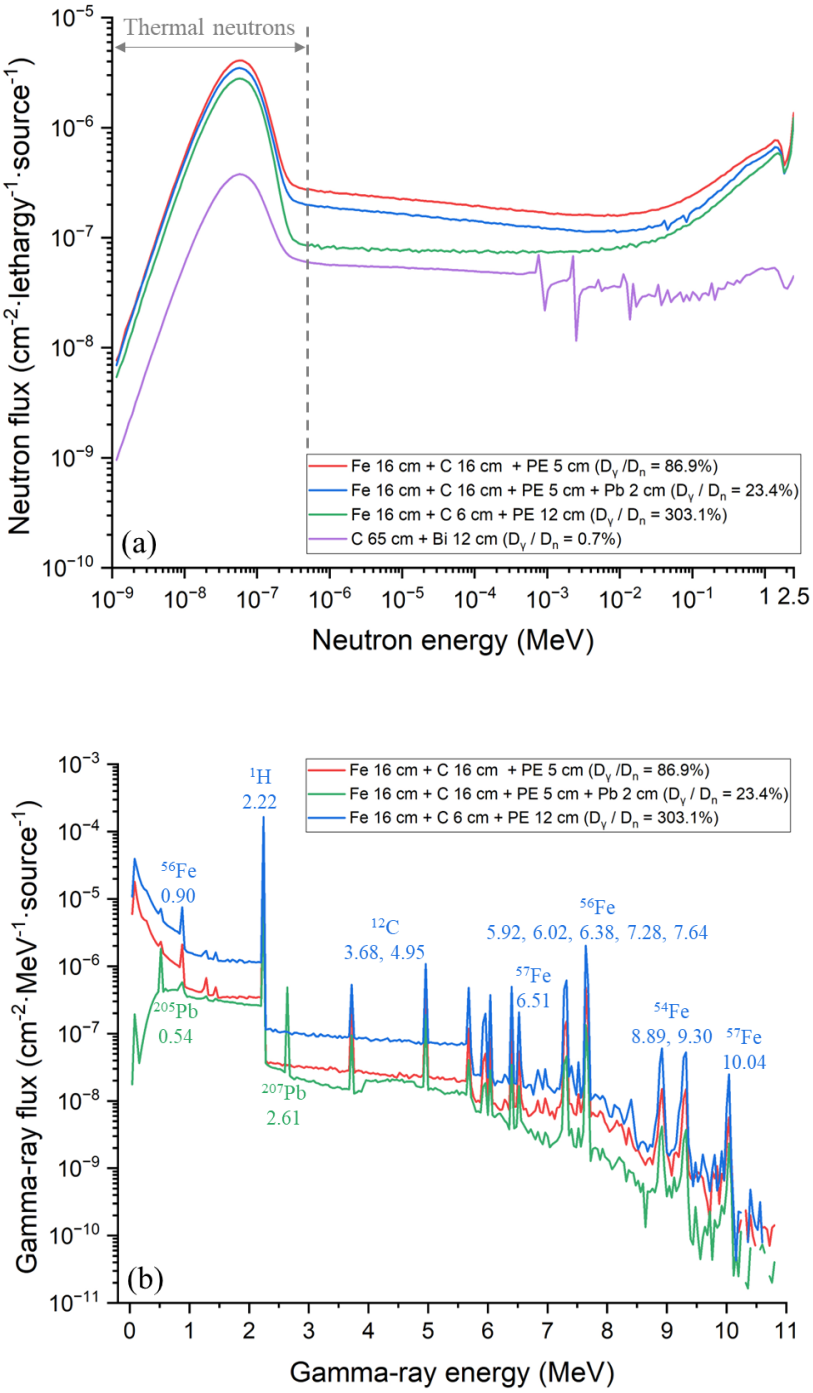

Figure 3.12. Energy spectra of T-dominated fields: (a) Neutron spectra; (b) Gamma-ray spectra.

3.3.4 Gamma-ray-only field

A gamma-ray-only field is generated using "Fe 16 cm + PE 33 cm", and the results are summarized in Table 3.4. 16 cm Fe is used to remove the target gamma-ray dose. PE is used to absorb neutrons and produce gamma-rays via the $^{1}H(n,\gamma)^{2}H$ reaction to increase D_γ/D_n. In this gamma-ray-only field, D_γ/D_n is 11880.6% and $D_\gamma/D_{\gamma+n}$ is 99.2%. The gamma-ray spectrum of "Fe 16 cm + PE 33 cm" is shown in Figure 3.13. Gamma-rays are produced up to 11 MeV, with characteristic peaks at 2.22, 3.68, 4.95, 5.92, 6.02, 6.38, 6.51, 7.28, 7.64, 8.89, 9.30, and 10.04 MeV via $^{1}H(n,\gamma)^{2}H$, $^{12}C(n,\gamma)^{13}C$, $^{56}Fe(n,\gamma)^{57}Fe$, $^{57}Fe(n,\gamma)^{58}Fe$, $^{54}Fe(n,\gamma)^{55}Fe$ reactions [66] [71].

Table 3.4. Characteristics of gamma-ray-only field.

Material	Dose (μGy·source^{-1})		D_γ/D_n	$D_\gamma/D_{\gamma+n}$
	D_γ	D_n		
Fe + PE 16 cm + 33 cm	2.75×10^{-11}	2.31×10^{-13}	11880.6%	99.2%

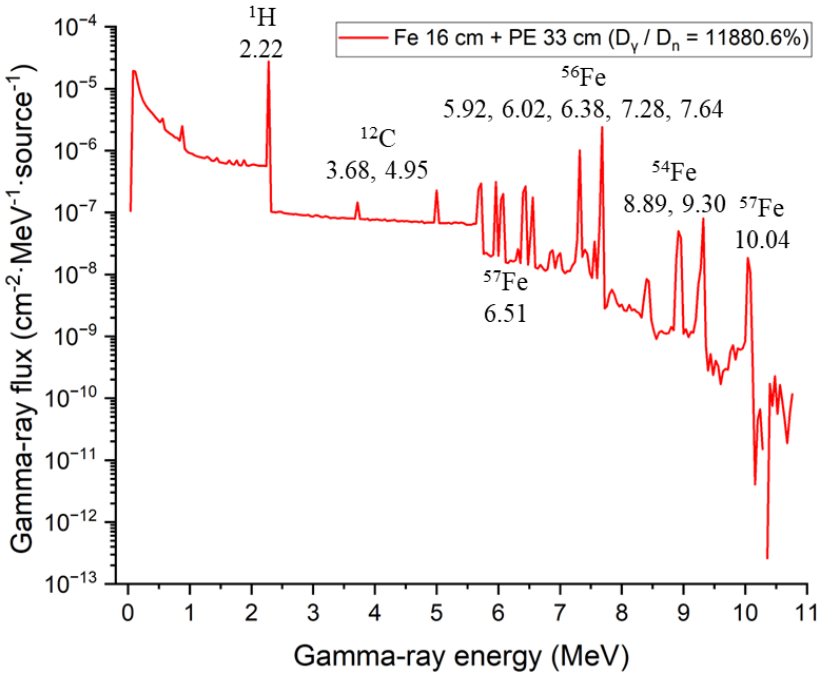

Figure 3.13. Gamma-ray spectrum of gamma-ray-only field.

3.4 Dose rate at OKTAVIAN

The neutron intensity of the continuous D-D neutron source at the OKTAVIAN facility was ~1×10^9 n/s. The dose rate of the target gamma-ray dose, $\dot{D}_{\gamma_{target}}$, was estimated as 2.06×10^4 μGy·h^{-1} to 9.34 μGy·h^{-1} at the distance to source from 1 cm to 100 cm. The gamma-ray dose rates, $\dot{D}_\gamma$, and neutron dose rates, $\dot{D}_n$, were estimated for each n-γ mixed field, as summarized in Table 3.5. These n-γ mixed fields can be easily customized by selecting the moderator assemblies for users with different requirements of radiation characteristics.

Table 3.5. Estimation of $\dot{D}_\gamma$ and $\dot{D}_n$.

Mixed field	$\dot{D}_\gamma/\dot{D}_n$	$\dot{D}_\gamma/\dot{D}_{\gamma+n}$	$\dot{D}_\gamma$ (μGy·h^{-1})	$\dot{D}_n$ (μGy·h^{-1})
F-dominated field	1.0-5.9%	1.0-5.6%	0.67 - 93.22	67.64 - 1.59×10^3
	17.9-977.7%	15.2-90.7%	282.08 – 3.76	1.58×10^3 - 0.38
E-dominated field	5.0-65.2%	4.7-39.5%	2.31×10^{-3} - 0.24	0.05 - 0.38
	112.5-921.1%	52.9-90.2%	0.46 - 1.58	0.41 - 0.16
T-dominated field	0.7%	0.7%	0.11	14.79
	8.3-39.1%	7.7-28.1%	7.75 - 54.45	92.97 - 139.27
	86.9-946.3%	46.5-90.4%	129.06 – 426.09	154.71 – 40.63
Gamma-ray-only field	11880.6%	99.2%	98.88	0.83

To enhance $\dot{D}_\gamma$ and $\dot{D}_n$, a Pb reflector was considered with thicknesses of 5 cm, 10 cm, and 20 cm, as shown in Figure 3.14. A reflector can scatter neutrons back into the moderators and avoid neutron leakage. Pb ensures no additional neutron moderation occurs and only redirection of neutrons due to the large (n,n) cross sections [40]. With a 5-20 cm Pb reflector, $\dot{D}_\gamma$ and $\dot{D}_n$ were calculated for "Fe 16 cm", "W 15 cm + Fe 5 cm + MgF_2 40 cm + LiF 0.5 cm", "Fe 16 cm + C 16 cm + PE 5 cm", and "Fe 16 cm + PE 33 cm", as summarized in Table 3.6. $\dot{D}_\gamma$ and $\dot{D}_n$ are enhanced by approximately 0.3-0.7 times for "Fe 16 cm", 1.8-11.4 times for "W 15 cm + Fe 5 cm + MgF_2 40 cm + LiF 0.5 cm", 0.7-2.9 times for "Fe 16 cm + C 16 cm + PE 5 cm", and 0.4-2.2 times for "Fe 16 cm + PE 33 cm",

respectively.

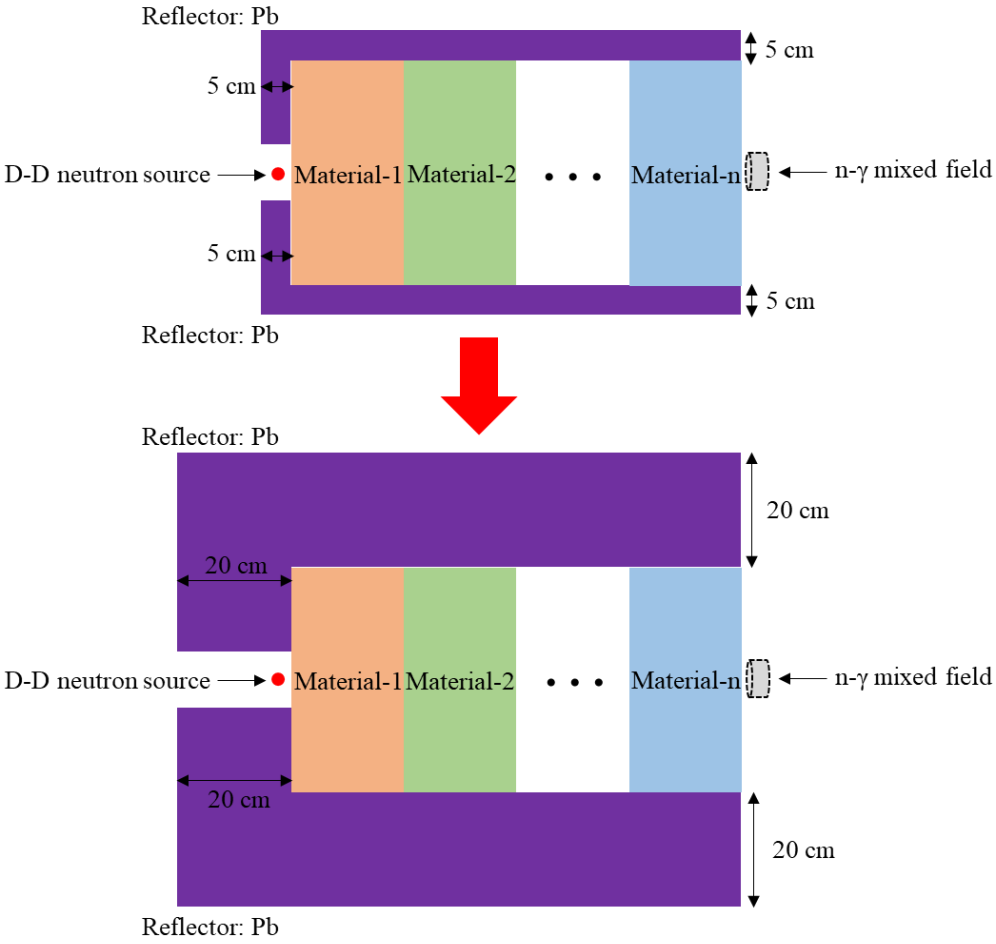

Figure 3.14. 5-20 cm Pb reflector for moderator assembly.

Table 3.6. Performance of a 5-20 cm Pb reflector.

Moderator	Reflector	$\dot{D}_\gamma$ (μGy·h^{-1})	$\dot{D}_n$ (μGy·h^{-1})
Fe 16 cm	×	282.08	1.58×10^3
	Pb 5 cm	377.20	2.27×10^3
	Pb 10 cm	404.30	2.53×10^3
	Pb 20 cm	425.12	2.76×10^3
W 15 cm + Fe 5 cm + MgF_2 40 cm + LiF 0.5 cm	×	0.46	0.41
	Pb 5 cm	1.28	1.28
	Pb 10 cm	2.45	2.51
	Pb 20 cm	5.04	5.14
Fe 16 cm + C 16 cm + PE 5 cm	×	129.06	148.47
	Pb 5 cm	241.20	248.36
	Pb 10 cm	348.97	336.19
	Pb 20 cm	504.40	455.84
Fe 16 cm + PE 33 cm	×	98.88	0.83
	Pb 5 cm	164.98	1.15
	Pb 10 cm	225.80	1.59
	Pb 20 cm	319.33	2.61

3.5 Analysis of wall scattering effect in the heavy irradiation room at OKTAVIAN

3.5.1 Source term of the D-D neutron

OKTAVIAN was built in Osaka University and first operated in 1981 [73]. There is an intense 14 MeV neutron source facility by D-T reaction [74]. For more than 40 years, various fusion related experiment studies have been carried out, i.e. neutron-nuclear reaction cross section measurements, integral benchmark experiments, tritium breeding ratio (TBR) measurements, neutron detector developments, etc. The configuration of OKTAVIAN [74] is shown in Figure 3.15. OKTAVIAN is an 18 m × 32 m room with 80 cm thick concrete walls. A 300 keV deuterium beam is available by using a Cockcroft-Walton type accelerator with a duoplasmatron ion source. After acceleration, two beamlines are provided through the switching magnet as follows: (1) one is at 37.5° line for a continuous neutron source in the heavy irradiation room; (2) another one is at the 30° line for a pulsed neutron source. The parameters of OKTAVIAN [75] are listed in Tables 3.7 and 3.8. The maximum intensity of the continuous neutron source is approximately 3×10^{12} D-T neutrons per second. D-D neutrons are also available via interaction between the self-loading deuterons and incident deuterons.

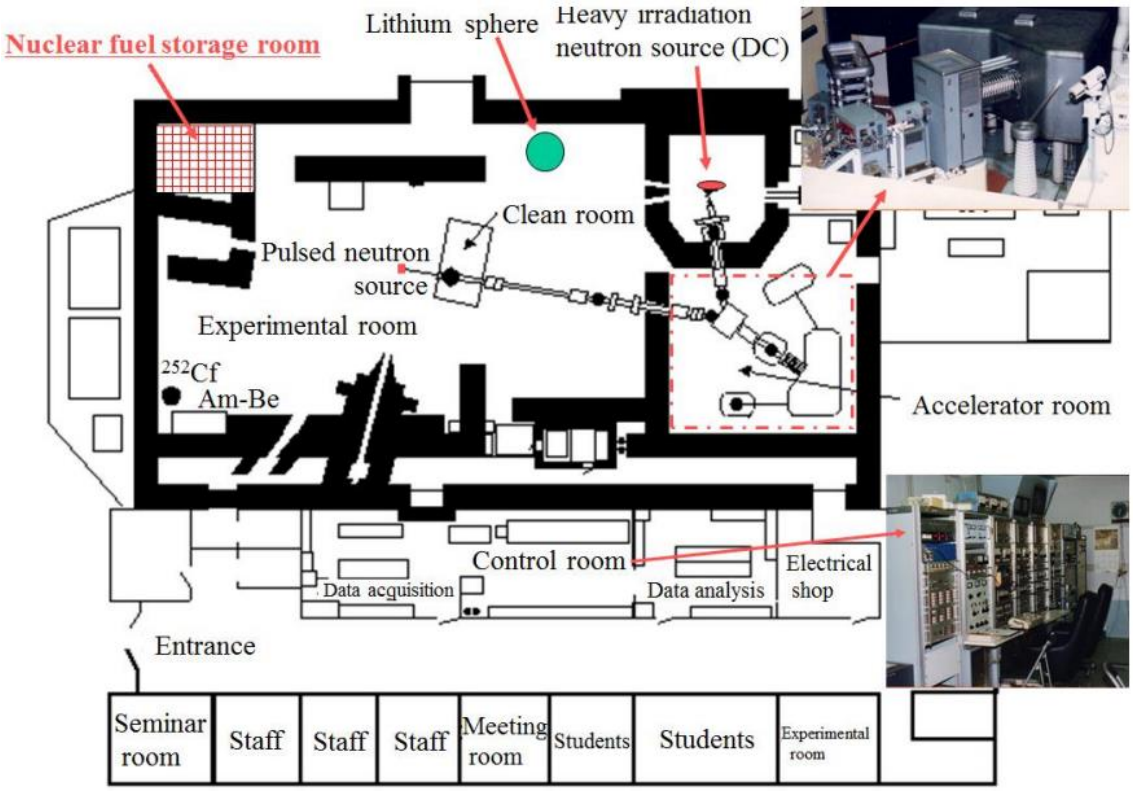

Figure 3.15. Layout of OKTAVIAN [74].

Table 3.7. Maximum and daily operation parameters of continuous beam of OKTAAVIAN [75].

	Maximum	Daily
Beam energy (keV)	300	250
D+ beam current at the rotating target (mA)	20	10
Minimum beam spot size at the target	15	~30
Ratoting target, diameter (cm)	20	~20
D-D neutron yield, continuous (n/s)	3×10^{10}	No use
D-T neutron yield, continuous (n/s)	3×10^{12}	10^{12}
Tritium amount for one rotating target (Bq / piece)	3×10^{13}	1×10^{13}
Target life (half value of neutron yield) (A·h)	~ 1 A·h for half life	

Table 3.8. Maximum and daily operation parameters of pulsed line of OKTAAVIAN [75].

	Maximum	Daily
Beam energy (keV)	300	250
Minimum beam spot size at the target	15	~30
Target life (half value of neutron yield) (A·h)	~ 1 A·h for half life	
Pulse width (ns)	1.5	1.8
Ratio of neutron pulse / peak and background	10^{14}	5×10^{13}
D-T neutron yield of nanosecond pulsed mode (n / pulse)	~ 10^{4}	10^{3}

The source term of the D-D neutron at the heavy irradiation room is shown in Figure 3.16. The average energy of the D-D neutron source is ~2.62 MeV. Considering the target assembly model in Figure 3.5, the incident neutron spectrum at 0° direction was calculated, as shown in Figure 3.17. The average neutron energy of the incident neutrons at 0° direction is ~2.83 MeV.

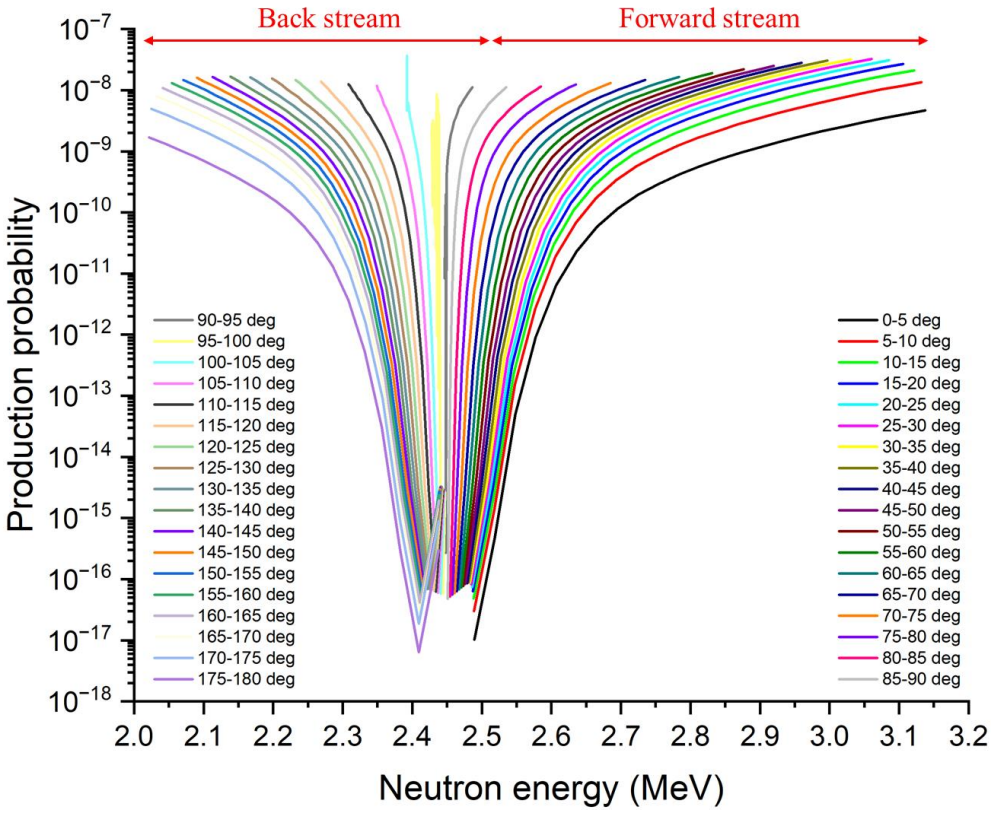

Figure 3.16. Source term of D-D neutron at OKTAVIAN.

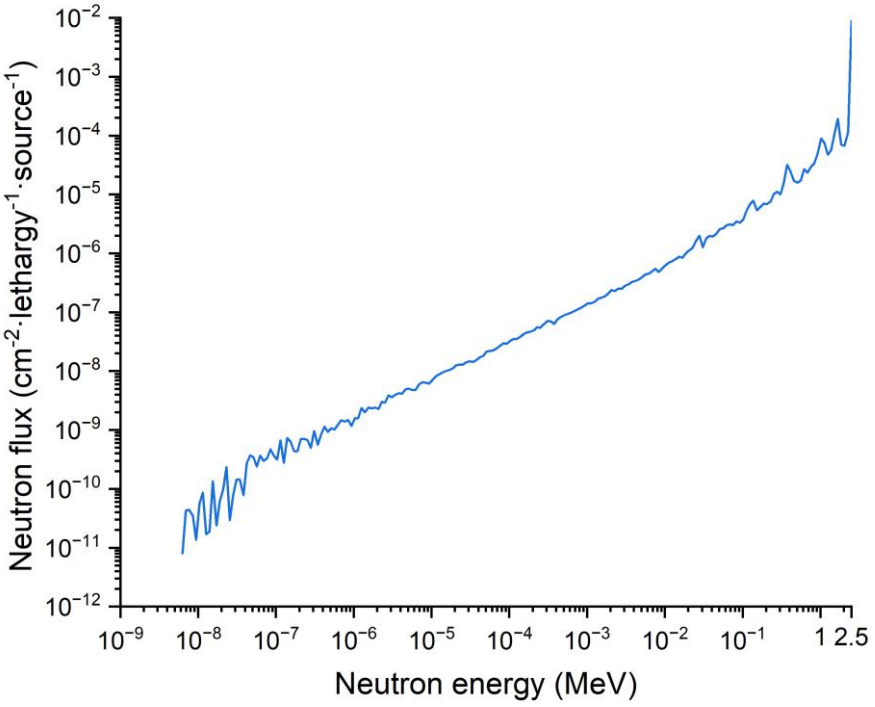

Figure 3.17. Incident neutron spectrum at 0° direction, OKTAVIAN.

3.5.2 Contaminant neutron and gamma-ray

The layout of the heavy irradiation room at OKTAVIAN is shown in Figure 3.18. The size of the experimental room is 460 cm × 420 cm × 420 cm and the thickness of the concrete structure (ρ = 2.20 g/cm^3) is 100 cm. To analyze the room scattered neutron effect and give reference to neutron irradiation experiments in the heavy irradiation room at OKTAVIAN, the direct neutron dose, D_n, the target gamma-ray dose, $D_{\gamma_{target}}$, the wall scattered neutron dose, $D_{n_{wall}}$, and the wall induced gamma-ray dose, $D_{\gamma_{wall}}$, were calculated at 10-190 cm distance. The results of D_n, $D_{\gamma_{target}}$, $D_{n_{wall}}$, and $D_{\gamma_{wall}}$ are shown in Figure 3.19. $D_{n_{wall}}$ and $D_{\gamma_{wall}}$ remain approximately constant in the room, while D_n and $D_{\gamma_{target}}$ is inversely proportional to the square of the distance. The results of $D_{\gamma_{target}}$ / D_n, $D_{n_{wall}}$ / D_n and $D_{\gamma_{wall}}$ / D_n are shown in Figure 3.20. $D_{\gamma_{target}}$ / D_n remains below 2% at 10-190 cm distance. In contrast, $D_{n_{wall}}$ / D_n and $D_{\gamma_{wall}}$ / D_n increase rapidly, rising from 0.2% to 91.9% and from 0.1% to 22.8%, respectively, as the distance increases from 10 cm to 190 cm. As the distance is below 100 cm, $D_{n_{wall}}$ / D_n and $D_{\gamma_{wall}}$ / D_n are below 20.2% and 8.0%, respectively. $D_{\gamma_{target}}$ is

relatively low, however, it is essential to evaluate $D_{n_{wall}}$ and $D_{\gamma_{wall}}$ if the distance is far from the neutron target.

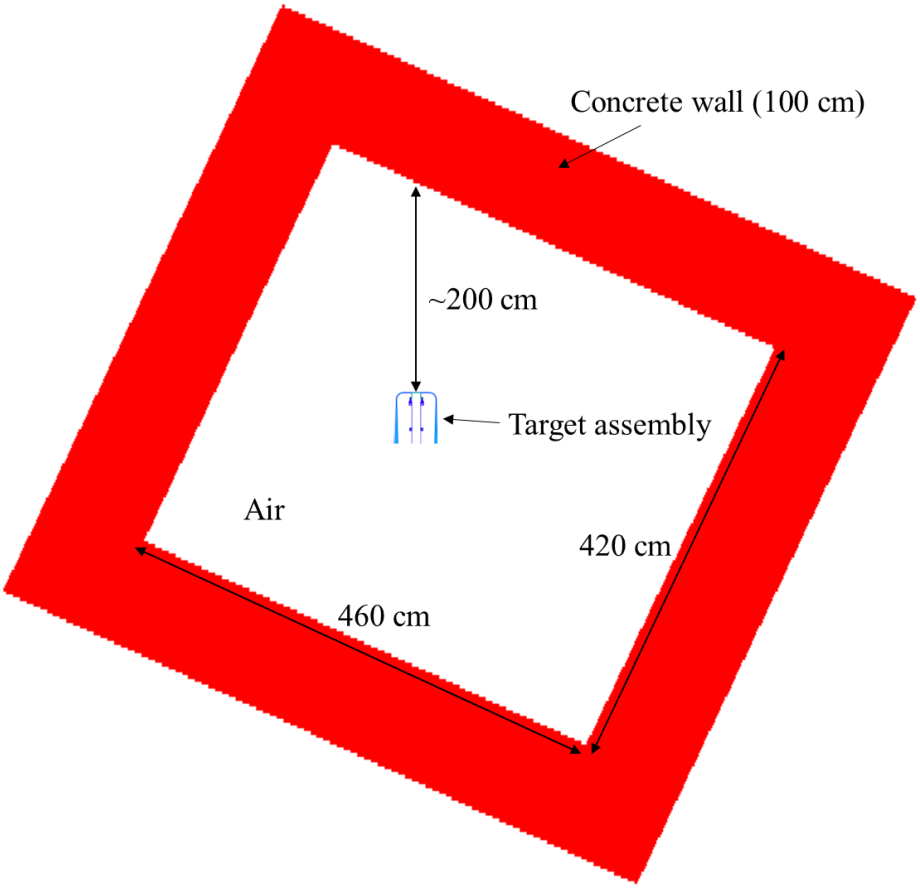

Figure 3.18. Top view of heavy irradiation room.

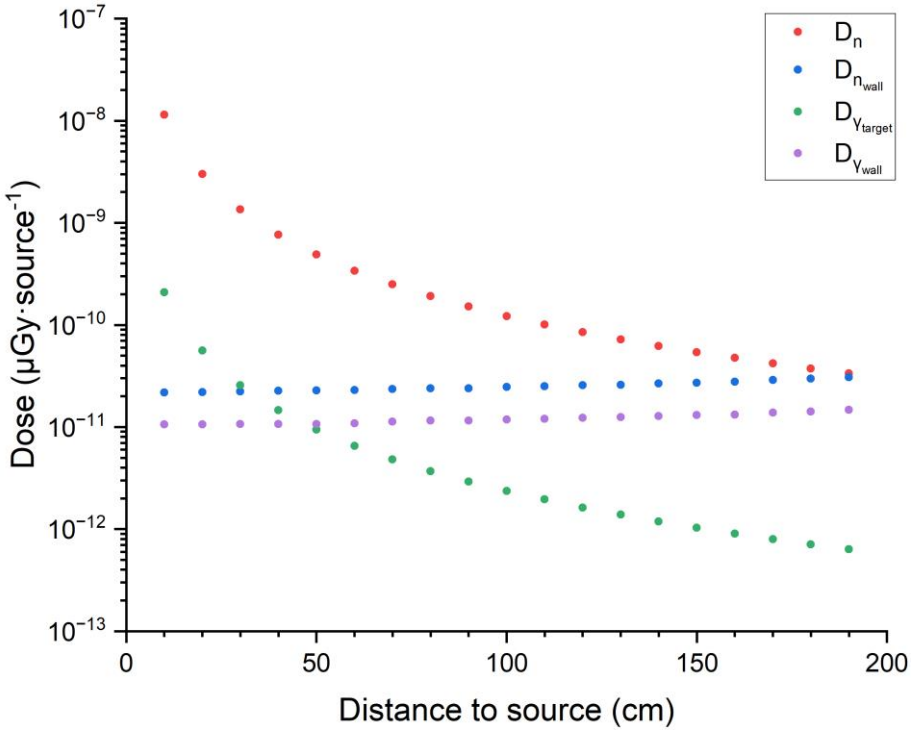

Figure 3.19. Results of D_n, $D_{\gamma_{target}}$, $D_{n_{wall}}$, and $D_{\gamma_{wall}}$.

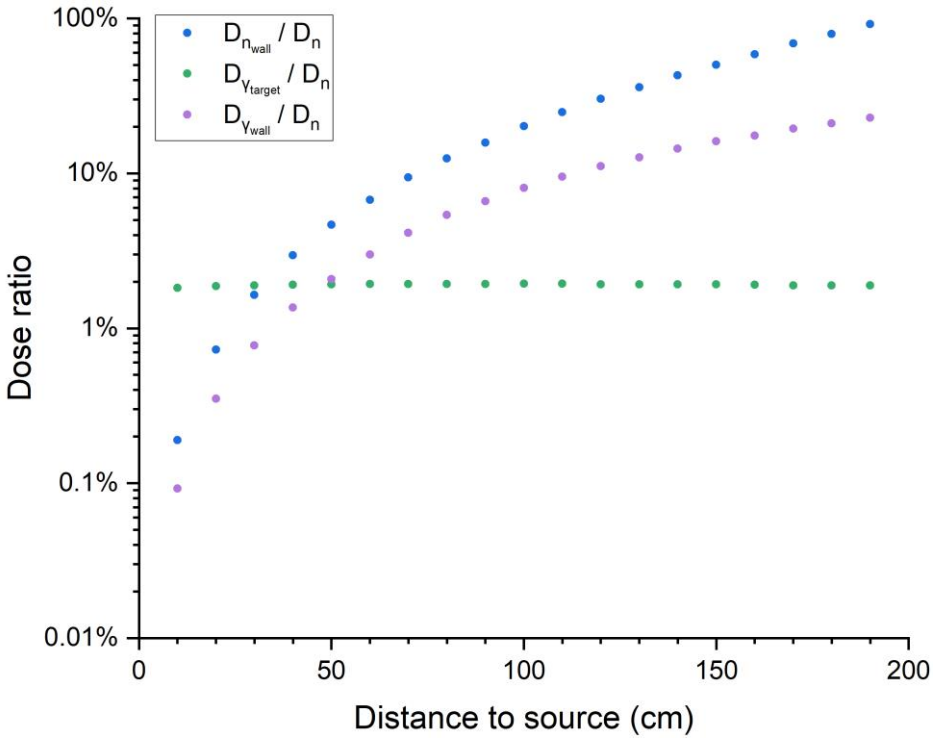

Figure 3.20. Results of $D_{n_{wall}}$ / D_n and $D_{\gamma_{wall}}$ / D_n.

The spectra of the scattered neutrons and the wall induced gamma-rays are shown in Figure 3.21. In Figure 3.21 (a), $D_{thermal}$ / D_n, D_{epi} / D_n, and D_{fast} / D_n are 67.3-53.7%, 2.5-2.0%, 30.3-44.3%,

respectively, at the distance from 10 cm to 190 cm, In Figure 3.21 (b), gamma-rays are observed in the energy range up to 14 MeV due to the H, O, Na, Mg, Al, Si, S, K, Ca, and Fe elements from the concrete room.

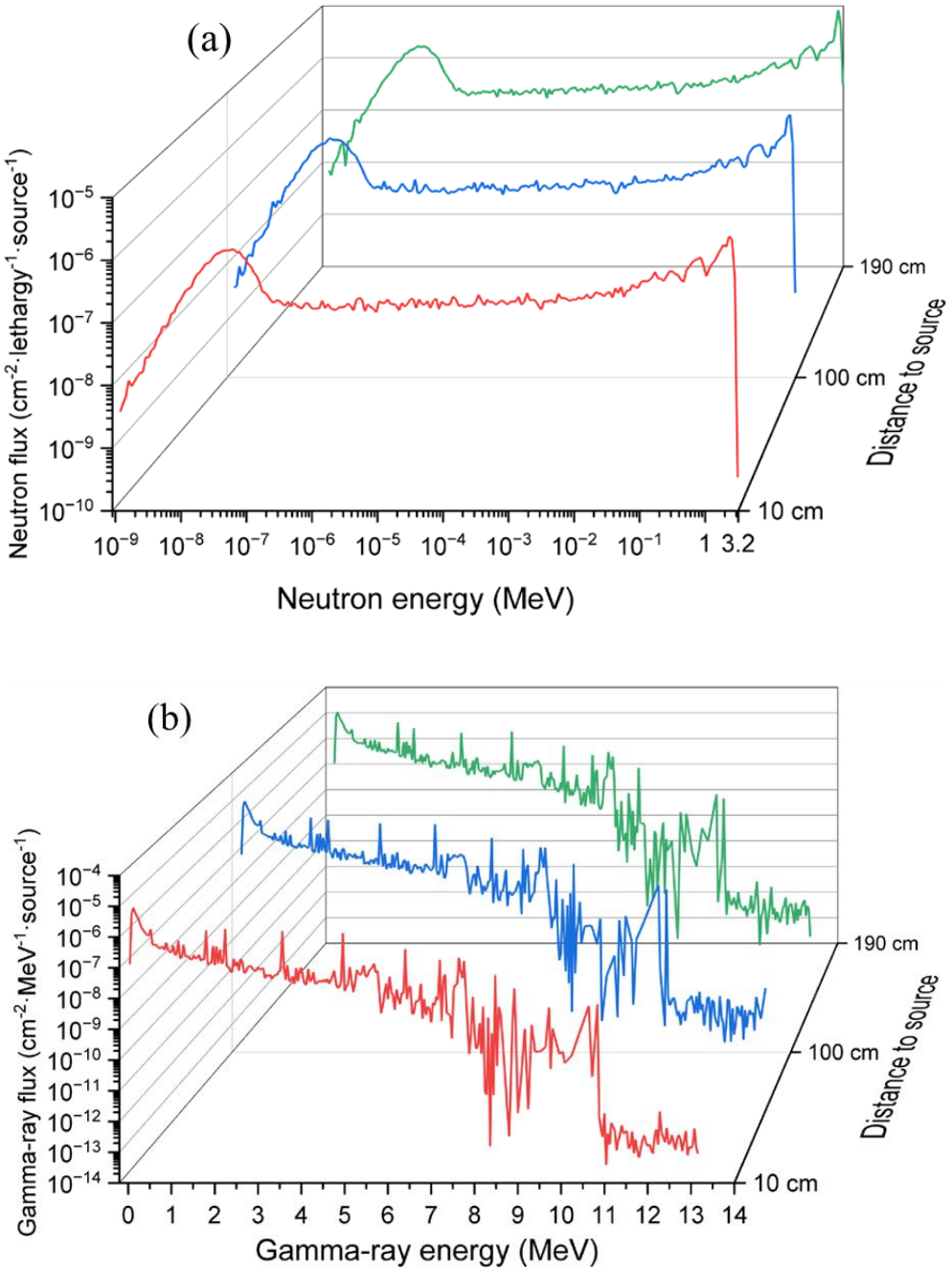

Figure 3.21. (a) Scattered neutron spectra; (b) Wall induced gamma-ray spectra.

Chapter 4. Development of a ~10 MeV gamma-ray field using an Fe-PE-Cd moderator assembly with a p-Li neutron source

4.1 Introduction

High energy gamma-rays can not only expand the applications of gamma-ray measurement equipment but also contribute to advancements in medical treatment and biological research and support industrial application. Standard isotope gamma-ray sources are widely used for dosimeter calibration, as ^{22}Na, ^{54}Mn, ^{60}Co, ^{65}Zn, ^{75}Se, ^{88}Y, ^{124}Sb, ^{133}Ba, ^{137}Cs, and ^{152}Eu, ^{192}Ir, ^{203}Hg [45] [51] [52] listed in Table 2.8. However, these gamma-ray sources are limited to the energy range below 1.5 MeV.

In previous studies, many gamma-ray sources have been proposed within an energy range from a few to tens of MeV. Joel G. Rogers, et. al. [76] constructed a 7-9 MeV gamma-ray source using an Am-Be and a ^{252}Cf neutron sources moderated by 60×60×50 cm^3 paraffin and a Φ 7.6 mm × 6-25 mm “Nickel-200” rod. P.-A. Soderstrom, et. al. [77] constructed a 9 MeV gamma-ray source using a Pu-Be neutron source moderated by 8 cm radius assembly mixed with 1.84 kg paraffin and 0.21 kg Ni. Both of these two gamma-ray sources were produced via thermal neutron capture reaction of ^{58}Ni(n,γ)^{59}Ni, however, ^{252}Cf, Am-Be, and Pu-Be neutron sources emit neutrons in a high energy and neutrons are mixed with the gamma-ray sources. Otherwise, large size moderators and far distance away from the sources are required to avoid neutron influence. Additionally, strong radioactive isotope neutron sources are necessary to increase gamma-ray flux, but it may cause safety issues for workers to build up the facility for the neutron source.

G. B. Bishop [78] reported a 6 MeV gamma-ray facility that utilized the fast neutron capture reaction of ^{16}O(n,p)^{16}N in the reactor cooling water. Andrej Zohar, et. al. [79] reported a 6-7 MeV irradiation system (air dose rate at 1 m from source: 0.1 mGy/h) using activated cooling water from TRIGA Mark II research reactor. Due to the high energy threshold of activation of water (10 MeV) and short half-life of ^{16}N (7.13 s), high energy neutrons and high circulation rate of cooling water are required to design the irradiation facility. Suzanne F. Nowicki, et. al. [80] developed a 6 MeV gamma-ray facility that utilized a circulating flow of water irradiated by a D-T pulsed neutron generator.

The 6-7 MeV Gamma-ray sources based on ^{19}F(p,αγ)^{16}O were developed by proton beams

bombarding CAF_2 Targets . H. Mach, et. al. [81] described a 6.13 MeV gamma-ray source using a ~340 KeV proton beam bombarding a 100 μg/cm2 CaF_2 target. Munehiko Kowatari, et. al. [82] described a 6-7 MeV gamma-ray source (91.2±4.3 $\mu Gyh^{-1}\cdot\mu A^{-1}$ at 100 cm) using a 2.7 MeV proton beam bombarding a 5.30 $mg\cdot cm^{-2}$ CaF_2 target.

High energy and flux gamma-rays can be generated by electron beams stopping by high atomic number (z) target Cu, Pb based on bremsstrahlung. Shun Li, et. al. [83] optimized a gamma-ray beam (up to 15 MeV) by 3.4 MeV and 12.5 MeV electron beams. V. Senthilkumaran, et. al. [84] produced focused 100 keV to 33 MeV gamma-ray beams (6.4 MeV in average) using a 200 MeV electron beams focused by a Pb converter target.

High quality and energy gamma-rays can be generated from inverse-Compton-scattering (ICS) off relativistic electron beams interacting with an intense laser pulse. Kazuhisa Nakajim [85] presented a gamma-ray beam source (2-20 MeV) via Compton scattering off relativistic 300-900 MeV electron beams from a high-power laser plasma accelerator. Shouyuan Chen, et. al. [86] reported a laser-driven in gamma-ray source (~6 MeV) based on a laser-wakefield accelerator (Ge/cm). These laser-driven ICS gamma-ray sources require high quality laser systems and extremely-high-energy electron accelerators (~GeV level).

In this chapter, a 2–10 MeV gamma-ray field was developed using a compact moderator assembly and a ~2.95 MeV p-Li neutron source at the 4.5 MV Dynamitron facility, Fast Neutron Laboratory (FNL), Tohoku University [34].

4.2 Materials and methods

4.2.1 Fast Neutron Laboratory (FNL)

In 1974, a 4.5 MV Dynamitron accelerator was constructed at Fast Neutron Laboratory (FNL) [87] of Tohoku University. This accelerator is a single-ended type with a Schenkel type high-voltage power. It provides a high-current duoplasmatron ion source to generate hydrogen, deuterium, and helium ion beams. In Figure 4.1, the size of the experimental room is 2300 cm × 1900 cm × 960 cm [34]. The concrete structure (ρ = 2.20 g/cm^3) is ~100 cm in thickness. The 30° neutron beam line, positioned 150 cm above the floor, provides neutron sources with energies from 8 keV to 15 MeV. The neutron sources [88] are listed in Table 4.2.

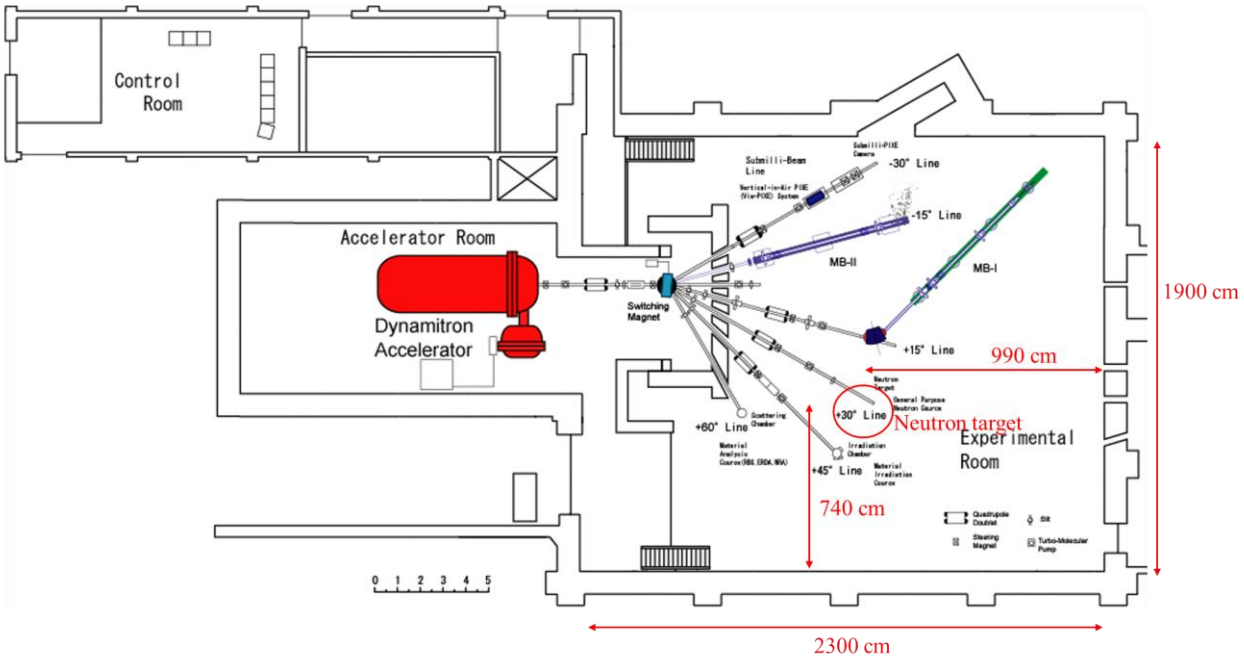

Figure 4.1. Layout of FNL [34].

Table 4.2. Neutron sources of FNL [88].

Neutron energy	Source reaction	Target / Backing	Neutron fluence ($n \cdot cm^{-2} \cdot \mu C^{-1}$)[b]
8 keV	$^{45}Sc(p,n)^{45}Ti$	^{45}Sc / Pt	1.0×10^{2}
27 keV	$^{45}Sc(p,n)^{45}Ti$	^{45}Sc / Pt	1.0×10^{2}
0.25 MeV	$^{7}Li(p,n)^{7}Be$	LiF / Pt	1.0×10^{4}
0.55 MeV	$^{7}Li(p,n)^{7}Be$	LiF / Pt	3.2×10^{4}
1.0 MeV	$T(p,n)^{3}He$	T-Ti / Cu	1.2×10^{4}
2.0 MeV	$T(p,n)^{3}He$	T-Ti / Cu	2.2×10^{4}
5.0 MeV	$D(d,n)^{3}He$	D_2 gas / Pt	2.2×10^{5}
15 MeV	$T(d,n)^{4}He$[a]	T-Ti / Cu	8.0×10^{4}

[a] D_3^+ beam (1.5 MeV).

[b] Typical values at 10 cm from the target.

4.2.2 Moderator assembly

In Figure 4.2, a ~10 MeV gamma-ray field is generated by a cuboid moderator assembly

consisting of a 1 cm thick Fe plate (ρ = 7.86 g/cm^3), a 50 cm thick PE moderator (ρ = 0.93 g/cm^3), and a 0.5 mm thick Cd foil (ρ = 8.65 g/cm^3). The neutron source is produced based on a p-Li reaction, where a ~2.95 MeV proton beam bombards a thick Li target. A detailed model of the neutron target is shown in Figure 4.3, consisting of a 2 mm thick Cu substrate and a 1.5 mm thick SUS304 beam tube.

In the moderator assembly, the Fe plate is used to produce high-energy gamma-rays based on the (n,γ) reaction. The PE moderator is designed to reflect source neutrons and reduce neutron leakage. Neutrons are effectively moderated and absorbed with the 30 cm thickness of PE based on neutron scattering and capture reactions with H and C. The Cd foil serves as a thermal neutron absorber due to its large (n,γ) cross sections [40].

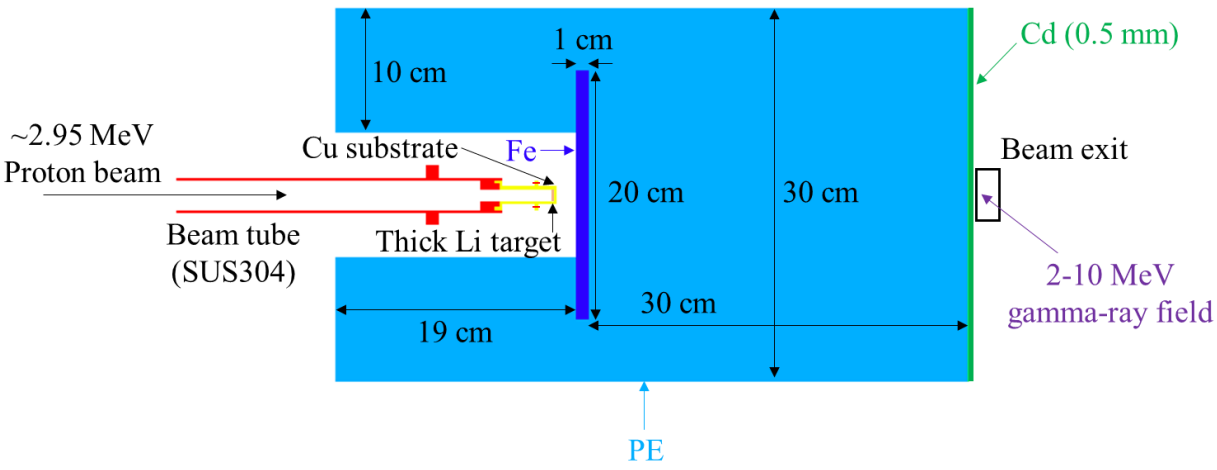

Figure 4.2. Design of moderator assembly.

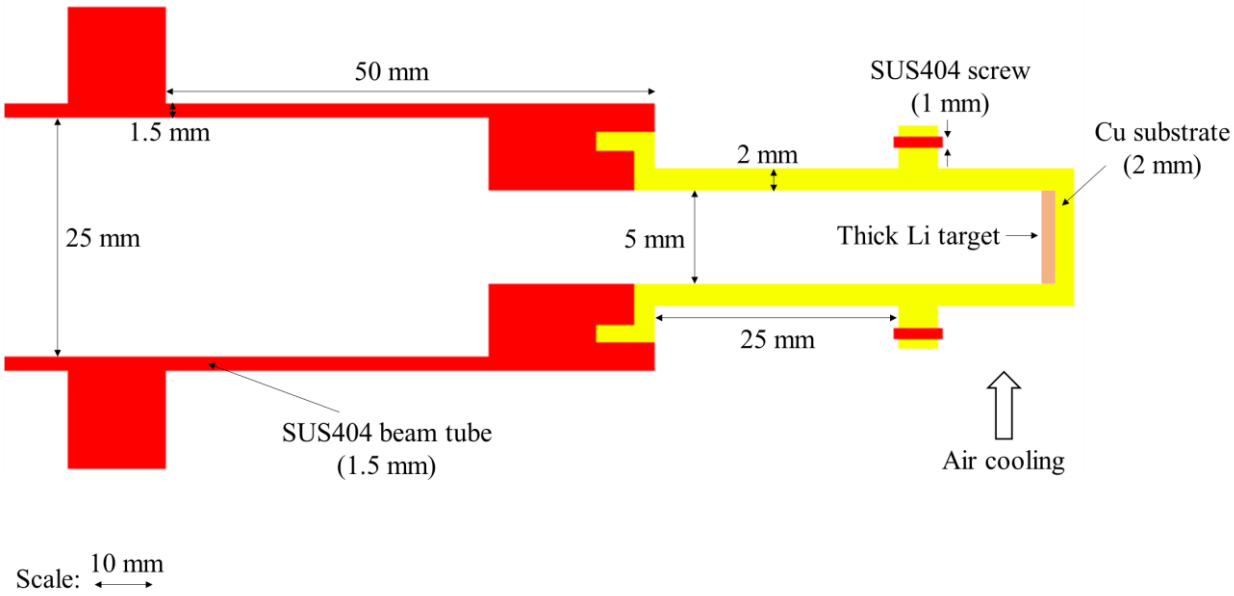

Figure 4.3. Model of neutron target.

4.2.3 Source term of ~2.95 MeV p-Li (thick) neutron

The neutron intensity of the p-Li source (~2.95 MeV proton beam, thick Li target) at FNL is ~1.08×10^{8} n·μC^{-1} [89]. The source term of energy and angular distributions is extracted from DROSG-2000 [90], as shown in Figure 4.4. Neutrons are produced with an average energy of 0.52 MeV in the energy range from 0.03 keV to 1.30 MeV.

In this Chapter, simulations are performed via Monte Carlo N-particle Code 6 (MCNP6) [91] based on ENDF/B-VIII.0 [65]. To compare different types of radiation, gamma-ray, neutron, and electron doses (Sv) are calculated using F4 tally combined with DEn and DFn cards, based on AP irradiation data [92]. The contribution of the concrete wall to a tally is calculated using CFn card.

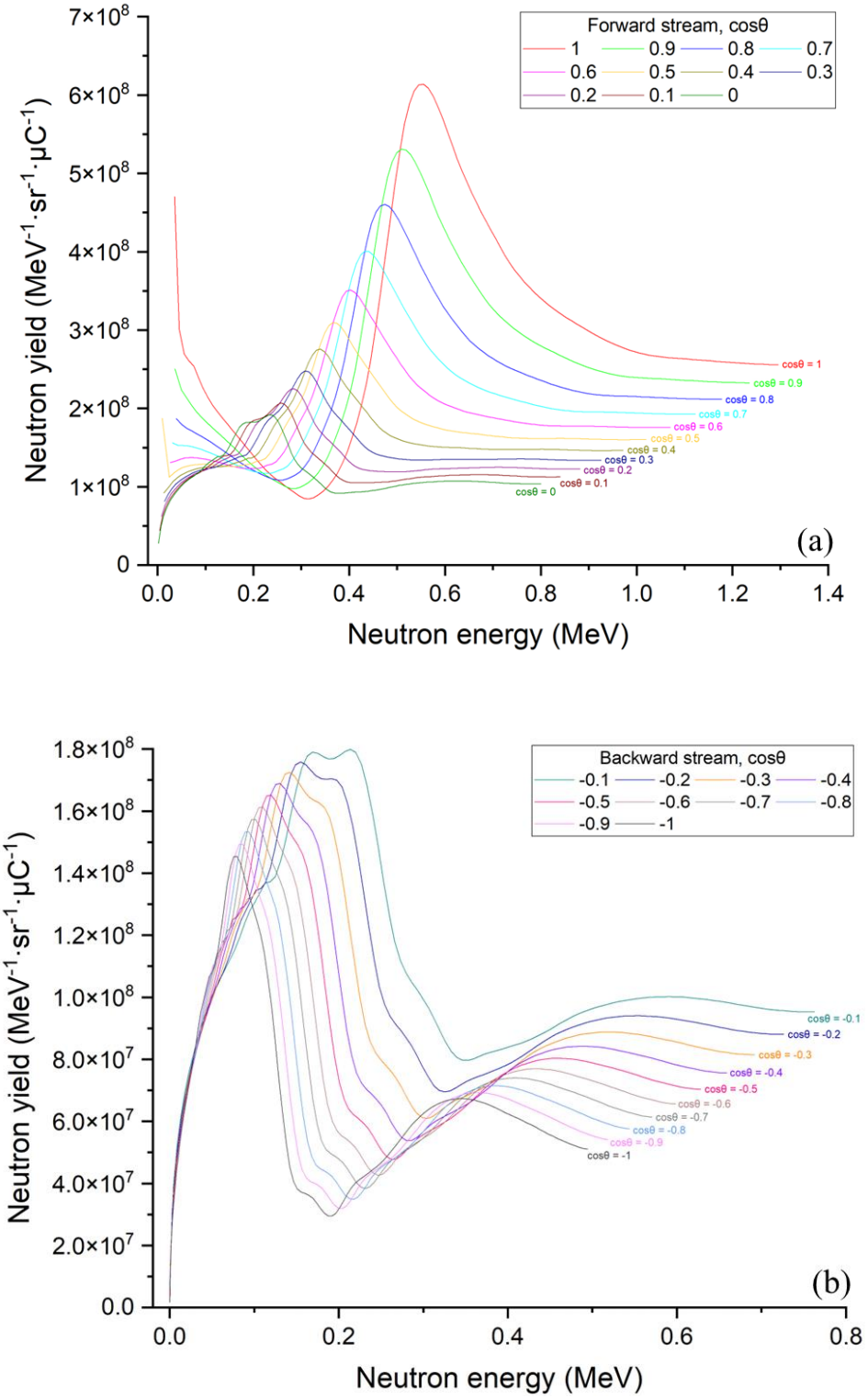

Figure 4.4. Angular and energy distributions of 2.5 MeV p-Li (thick target) neutron source. (a) Forward stream: cosθ = (-1,0); (b) Backward stream: cosθ= (-1, -0.05).

4.3 Simulation results

In the experimental room, contaminant neutrons and gamma-rays are generated unavoidably due

to neutron interactions with the surrounding materials. The scattered neutrons are reflected by the concrete wall, while the gamma-rays (target gamma-rays and wall-induced gamma-rays) are generated by neutron interactions with the neutron target structure and the concrete wall. The neutron and gamma-ray dose contamination, η, is defined as:

$$\eta = (D_n + D_{\gamma_{target}} + D_{n_{wall}} + D_{\gamma_{wall}}) / D_\gamma \quad (4.1)$$

where D_n and D_γ are the neutron and gamma-ray doses produced by the moderator assembly, $D_{\gamma_{target}}$ is the gamma-ray dose generated by the neutron target, $D_{n_{wall}}$ is the scattered neutron dose, and $D_{\gamma_{wall}}$ is the wall-induced gamma-ray dose.

At the beam exit shown in Figure 4.2, D_γ, D_n, $D_{\gamma_{target}}$, $D_{n_{wall}}$, and $D_{\gamma_{wall}}$ were calculated to determine η with and without the concrete wall. The results are summarized in Table 4.3. η is 0.46% without the concrete wall and 1.01% with the concrete wall. Contaminant neutrons and gamma-rays are negligible, since both η without and with the concrete wall are very low.

The gamma-ray spectrum produced by the moderator assembly was calculated at the beam exit, as shown in Figure 4.5. Gamma-rays are produced up to 10 MeV, with characteristic peaks at 2.22, 3.68, 4.95, 5.92, 6.02, 6.38, 6.51, 7.28, 7.64, 8.89, 9.30, and 10.04 MeV from $^{1}H(n,\gamma)^{2}H$, $^{12}C(n,\gamma)^{13}C$, $^{56}Fe(n,\gamma)^{57}Fe$, $^{57}Fe(n,\gamma)^{58}Fe$, $^{54}Fe(n,\gamma)^{55}Fe$ reactions [66] [71], respectively.

Table 4.3. Characteristics of gamma-ray field.

	η	D_γ (μSv·μC^{-1})	error	D_n (μSv·μC^{-1})	error	D_n / D_γ	$D_{\gamma_{target}}$ (μSv·μC^{-1})	error	$D_{\gamma_{target}} / D_\gamma$
Without wall	0.46%	3.57×10^{-2}	0.05%	1.15×10^{-4}	1.29%	0.32%	4.73×10^{-5}	2.32%	0.13%
With wall	1.01%	3.56×10^{-2}	0.04%	3.86×10^{-5}	11.56%	0.11%	4.73×10^{-5}	2.32%	0.13%

	$D_{n_{wall}}$ (μSv·μC^{-1})	error	$D_{n_{wall}} / D_\gamma$	$D_{\gamma_{wall}}$ (μSv·μC^{-1})	error	$D_{\gamma_{wall}} / D_\gamma$
With wall	1.73×10^{-4}	1.67%	0.48%	1.01×10^{-4}	1.54%	0.28%

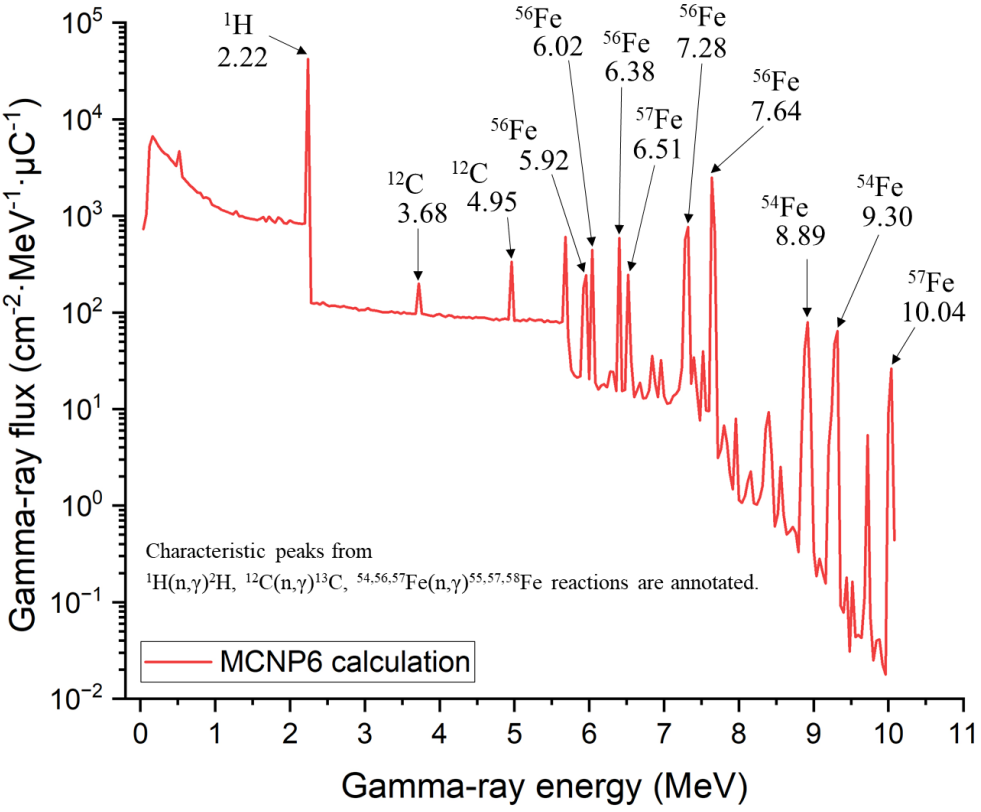

Figure 4.5. Gamma-ray spectrum at the exit.

4.4 Experiment results

4.4.1 Measurement of gamma-ray dose

The experimental setup for gamma-ray dose measurement is shown in Figure 4.6. In the experiment, nine pieces of the GD-301 with holder were placed inside a Cd case (compose six pieces of 0.05 mm Cd foils). In this chapter, to accurately calculate the absorbed dose of the GD-301 accurately, photon and electron transport simulations were performed via Particle and Heavy Ion Transport code System (PHITS) [93] version 3.320 based on ENDF/B-VIII.0 [65] and EGS5 [94] mode. Setting negs = 1, EGS5 mode can improve the accuracy of electron behavior from 1 keV to 1 TeV in medical physics. Radiation doses were calculated using T-track tally based on AP irradiation data [92].

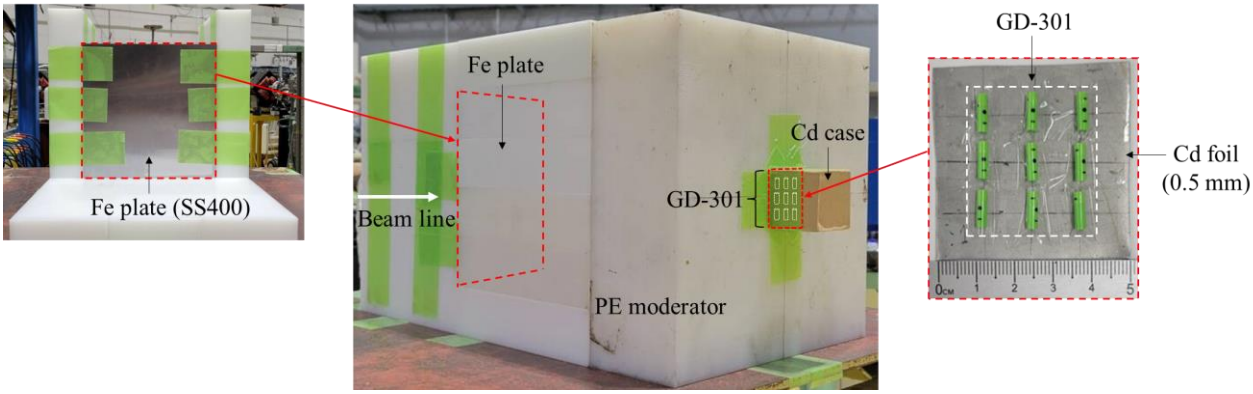

Figure 4.6. Experimental setup for dose measurement.

To calibrate the absorbed dose of the GD-301 with different gamma-ray energies, E_γ, in 15 keV - 12 MeV, $\dot{D}_{\gamma_{glass}}$ is expressed as:

$$\dot{D}_{\gamma_{glass}} = \int \dot{\Phi}_{E_\gamma} \cdot f_\gamma \, dE_\gamma \tag{4.2}$$

where $\dot{D}_{\gamma_{glass}}$ is the absorbed dose rate of the GD-301, $\dot{\Phi}_{E_\gamma}$ ($cm^{-2} \cdot h^{-1}$) is the gamma-ray flux rate, and f_γ ($\mu Gy \cdot cm^2$) is the gamma-ray dose conversion coefficient of the GD-301. In PHITS (ver.3.320) simulations, secondary electrons were discovered to be emitted from the moderator assembly due to gamma-ray interactions with H and C atoms in the PE moderator, including photoelectric effect, Compton scattering, and pair production, etc.

As shown in Figure 4.7, the electron flux is approximately two orders of magnitude lower than the gamma-ray flux. However, since these electrons are produced with energies up to 10 MeV, it is essential to quantify the absorbed dose of the GD-301. Hence, $\dot{D}_{glass}$ is extended as follows:

$$\dot{D}_{glass} = \dot{D}_{\gamma_{glass}} + \dot{D}_{e_{glass}} = \int \dot{\Phi}_{E_\gamma} \cdot f_{E_\gamma} \, dE_\gamma + \int \dot{\Phi}_{E_e} \cdot f_{E_e} \, dE_e \tag{4.3}$$

where $\dot{D}_{e_{glass}}$ is the electron absorbed dose of the GD-301, $\dot{\Phi}_{E_e}$ ($cm^{-2} \cdot h^{-1}$) is the electron flux rate, and f_{E_e} ($\mu Gy \cdot cm^2$) is the electron dose conversion coefficient of the GD-301 (with holder).

f_{E_γ} and f_{E_e} from 15 keV to 12 MeV are shown in Figure 4.8. In the energy range above 1 MeV, f_{E_e} is approximately two orders of magnitude larger than f_{E_γ}. The results of $\dot{D}_{glass}$, $\dot{D}_{\gamma_{glass}}$, and $\dot{D}_{e_{glass}}$, at the position shown in Figure 4.6, are summarized in Table 4.4. The experiment result of

$\dot{D}_{glass}$ was calculated as the average result from the nine pieces of the GD-301. The error of $\dot{D}_{glass}$ between PHITS (ver.3.320) simulation result and the experimental result is 6.27%.

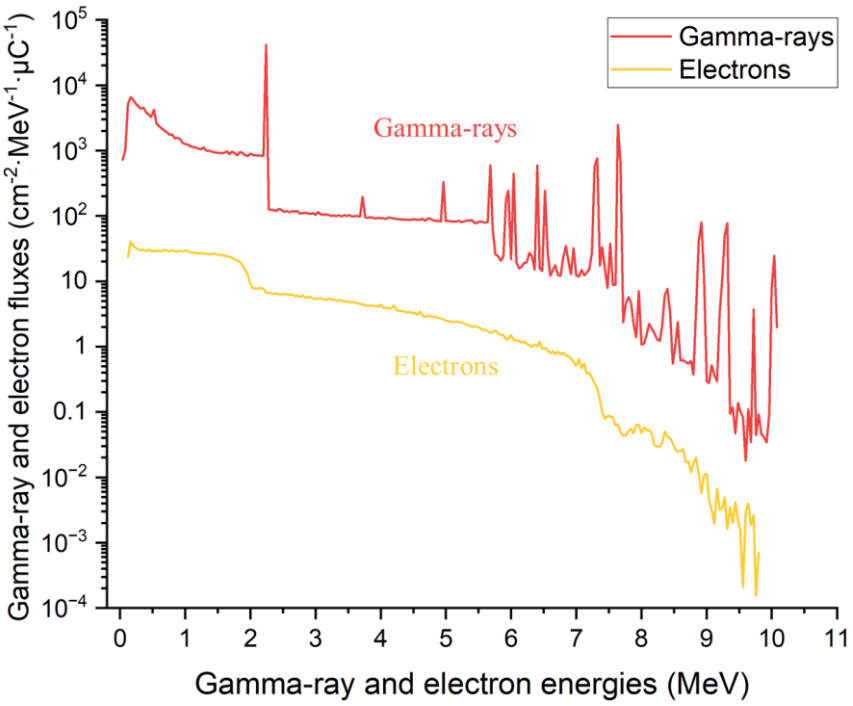

Figure 4.7. Gamma-ray and electron spectra via PHITS (ver.3.320) simulation.

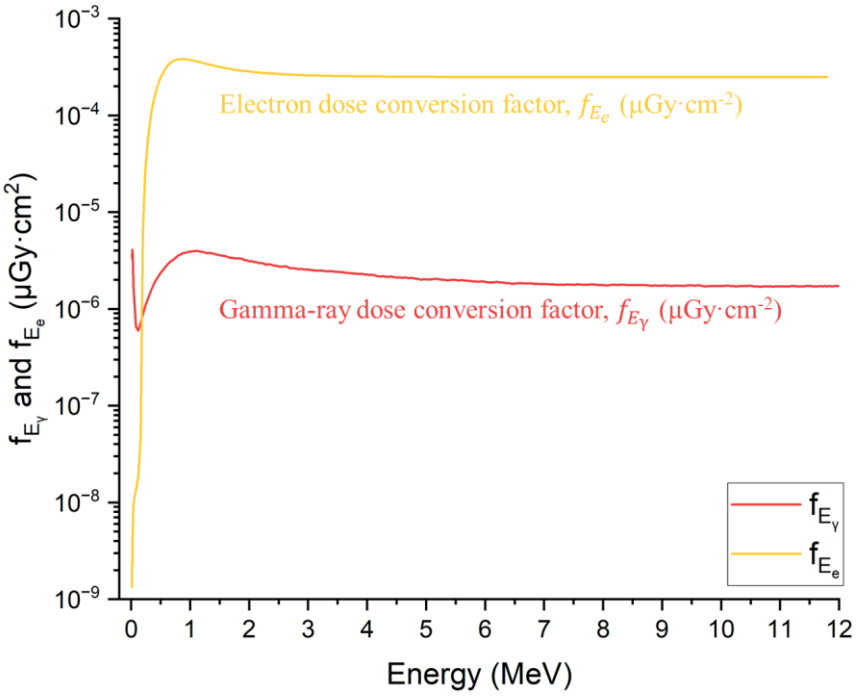

Figure 4.8. $f_{E_{\gamma,i}}$ and $f_{E_{e,i}}$ of GD-301 with holder.

Table 4.4. Absorbed dose rate of GD-301.

	$\dot{D}_{glass}$ (μGy·μC^{-1})	$\dot{D}_{\gamma_{glass}}$ (μGy·μC^{-1})	$\dot{D}_{e_{glass}}$ (μGy·μC^{-1})
PHITS (ver.3.320)	3.30×10^{-2}	1.62×10^{-2}	1.68×10^{-2}
Experiment	3.09×10^{-2}		

For mono-energetic gamma-rays, the gamma-ray dose rate in air, $\dot{D}_{\gamma}$, is expressed as:

$$\dot{D}_{\gamma} = \frac{\dot{\Phi}_{E_\gamma} \cdot \alpha_{E_\gamma}}{\dot{\Phi}_{E_\gamma} \cdot f_{E_\gamma}} \cdot \dot{D}_{\gamma_{glass}} = \eta_{\gamma} \cdot \dot{D}_{\gamma_{glass}} \tag{4.4}$$

where α_{E_γ} is the gamma-ray dose conversion coefficient in air calculated via PHITS (ver.3.320), and η_{γ} is the conversion coefficient of $\dot{D}_{\gamma_{glass}}$ to $\dot{D}_{\gamma}$. The results of η_{γ} (15 keV to 12 MeV) for the GD-301 (with holder) are shown in Figure 4.9. For gamma-rays with a continuous spectrum, $\dot{D}_{\gamma}$ is extended as:

$$\dot{D}_{\gamma} = \frac{\int \dot{\Phi}_{E_\gamma} \cdot \alpha_{E_\gamma} \, dE_\gamma}{\int \dot{\Phi}_{E_\gamma} \cdot f_{E_\gamma} \, dE_\gamma} \cdot \dot{D}_{\gamma_{glass}} = \eta_{\gamma} \cdot \dot{D}_{\gamma_{glass}} \tag{4.5}$$

η_{γ} was calculated as 2.27 for the GD-301 (with holder) according to the gamma-ray spectrum shown in Figure 4.7.

In Table 4.5, the experimental result of $\dot{D}_{\gamma}$, calculated using η_{γ} = 2.27, is compared with the simulation results from MCNP6 (mode n p e) and PHITS (ver.3.320) for gamma-ray dose rate, $\dot{D}_{\gamma}$, neutron dose rate, $\dot{D}_{n}$, and electron dose rate, $\dot{D}_{e}$. The errors of $\dot{D}_{\gamma}$ the simulation results and the experiment result are 1.64% for MCNP6 and 1.28% for PHITS (ver.3.320). $\dot{D}_{n}$ is negligible, as $\dot{D}_{n}/\dot{D}_{\gamma}$ is only 0.32%. Although $\dot{D}_{e}/\dot{D}_{\gamma}$ remains between 3% and 4%, it is essential to correct the electron absorbed dose of the GD-301, since $\dot{D}_{e_{glass}}$: $\dot{D}_{\gamma_{glass}} \approx$ 1:1.

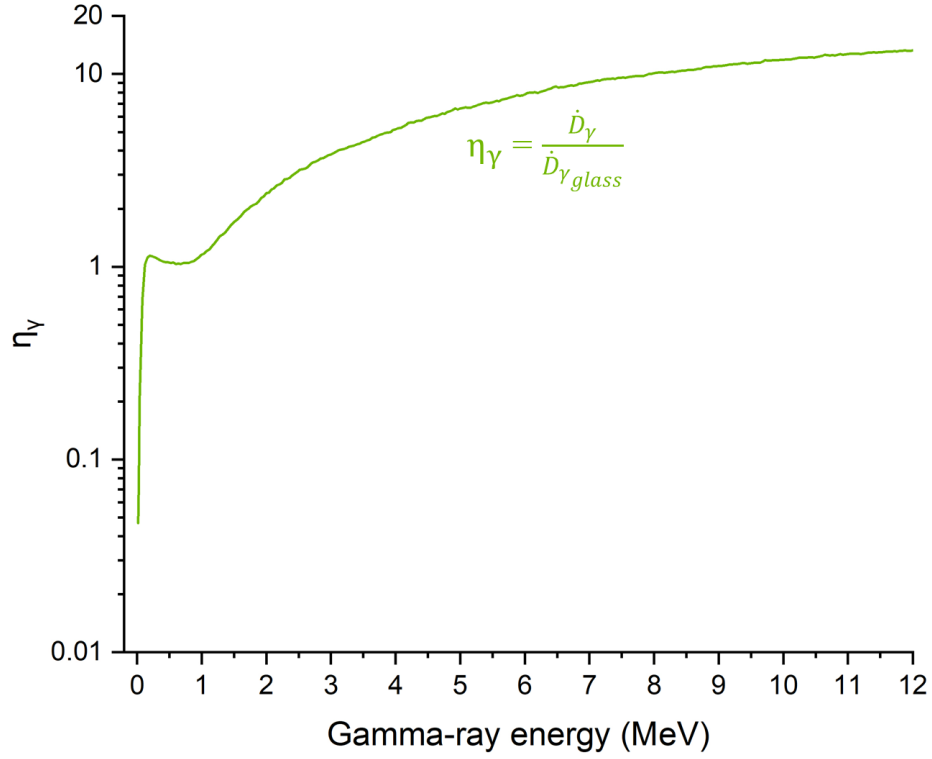

Figure 4.9. $\eta_{E_{\gamma,i}}$ of GD-301 with holder to mono-energetic gamma-rays.

Table 4.5. Dose rates of gamma-ray, electron, and neutron.

	$\dot{D}_\gamma$ (μSv·μC^{-1})	$\dot{D}_e$ (μSv·μC^{-1})	$\dot{D}_e$ / $\dot{D}_\gamma$	$\dot{D}_n$ (μSv·μC^{-1})	$\dot{D}_n$ / $\dot{D}_\gamma$
MCNP6	3.58×10^{-2}	1.41×10^{-3}	3.95%	1.16×10^{-4}	0.33%
PHITS (ver.3.320)	3.56×10^{-2}	1.17×10^{-3}	3.28%	1.14×10^{-4}	0.32%
Experiment	3.52×10^{-2}				

As proposed by our group [28] [29], the GD-301 can be used in combination with a filter to enhance the energy dependency. Meanwhile, a thin filter is enough to effectively stop these high energy electrons. In Figure 4.10, the minimum thickness of a filter material to stop the electrons is determined using an isotropic electron point source with a normalized spectrum from Figure 9. The electron stopping ability of a filter, ε_{filter}, is defined as:

$$\varepsilon_{filter} = \frac{D_{filter}}{D_{bare}} \tag{4.6}$$

where D_{bare} is the absorbed dose of the GD-301 without a filter, and D_{filter} is the absorbed dose of the GD-301 with a filter. Fe, Cu, Sn, W, and Pb were considered as a filter material with thickness from 0.1 mm to 5 mm, and the corresponding results of ε_{filter} for these materials were calculated via PHITS (ver.3.320). As shown in Figure 4.11, Fe (3.5 mm), Cu (3.1 mm), Sn (3.5 mm), W (1.2 mm), and Pb (2.1 mm) filters can control $\varepsilon_{filter} < 1\%$.

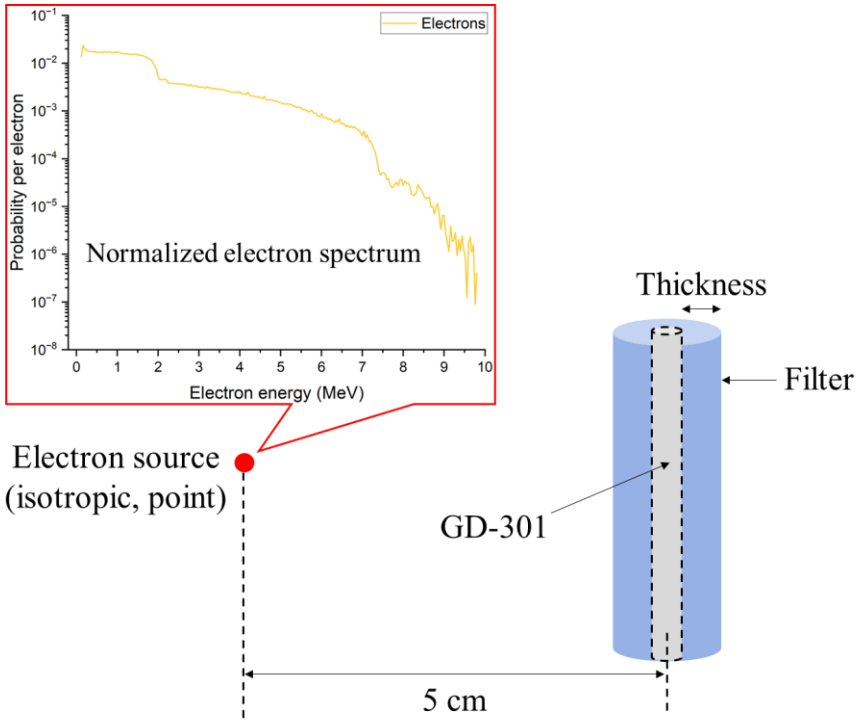

Figure 4.10. Filter to stop the electrons.

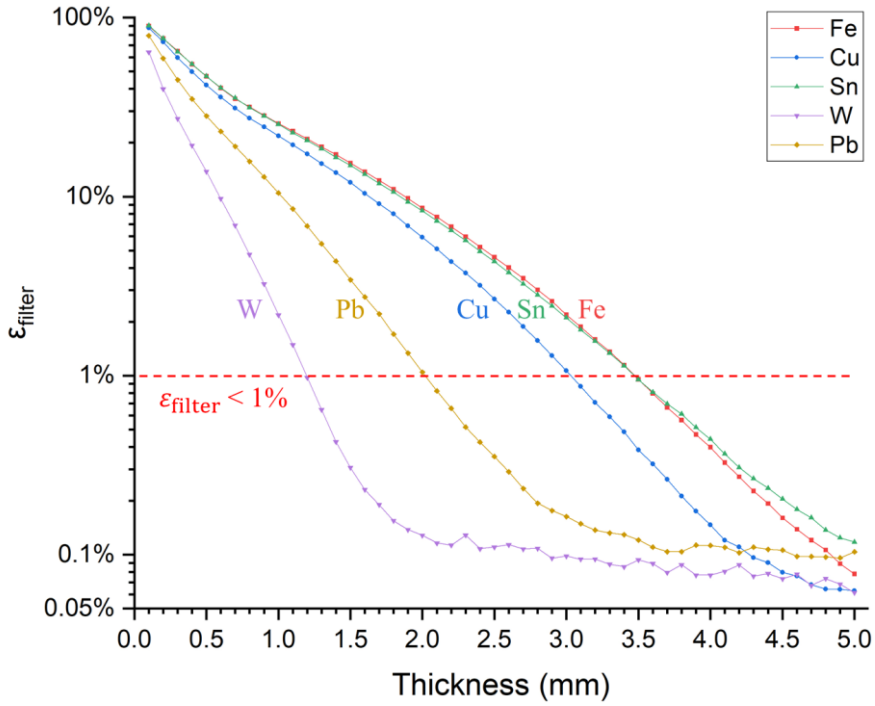

Figure 4.11. ε_{filter} of Fe, Cu, Sn, W, and Pb as a filter material.

4.4.2 Measurement of gamma-ray spectrum

The experimental setup for gamma-ray spectrum measurement is shown in Figure 4.12. The gamma-ray spectrum was measured by a high purity Ge detector (Φ 3.8 cm × 4 cm, GC1818, CANBERRA), positioned 10 cm from the moderator assembly. The relative detection efficiency of the Ge detector, ε_r, for a standard source is defined as [95]:

$$\varepsilon_r = \frac{C}{A_t \cdot Y \cdot \Delta_t} \tag{4.7}$$

where C is the total count (net area under the peak) recorded by the Ge detector, A_t is the radioactivity of the measured source corrected by decay time, Y is the gamma-ray yield, and Δ_t is the measurement time interval. ε_r was calculated in 20 keV - 12 MeV using F8 tally in MCNP6 and corrected by a standard ^{152}Eu source (9.29×10^3 Bq), as shown in Figure 4.13.

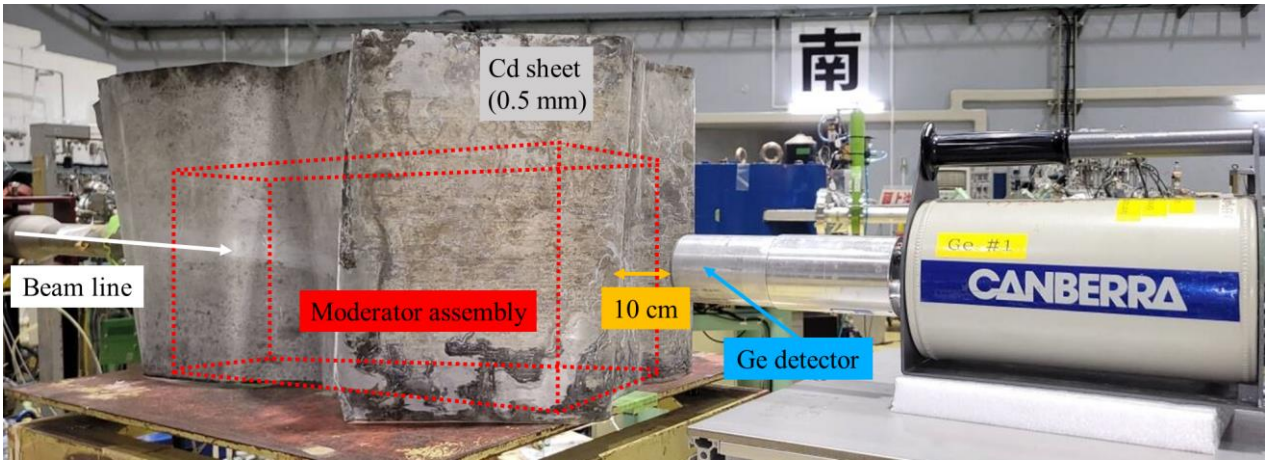

Figure 4.12. Experimental setup for gamma-ray spectrum measurement.

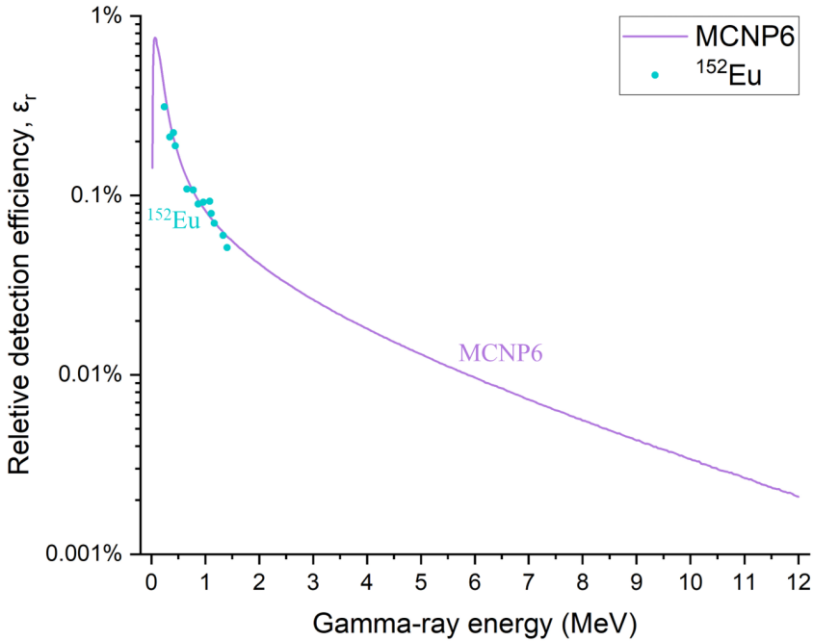

Figure 4.13. Detection efficiency of Ge detector.

Using the Ge detector, two gamma-ray spectra were measured with and without the Fe plate inside the moderator assembly, as shown in Figure 4.14. In Figure 4.14 (a), for the red curve, as the Fe plate is removed, the signal contribution in the energy range above 5 MeV from the surrounding substances in the experiment room can be distinguished, since H and C elements in the PE moderator primarily produce gamma-rays below 5 MeV [66] [71]. In Figure 4.14 (b), the background counts above 5 MeV are suppressed to correct the gamma-ray spectrum, through subtraction of the red curve from the blue curve in that energy range. Characteristic peaks at 2.22 MeV, 5.92 MeV, 6.02 MeV,

7.64 MeV, and 9.30 MeV from $^{1}H(n,\gamma)^{2}H$, $^{56}Fe(n,\gamma)^{57}Fe$, and $^{54}Fe(n,\gamma)^{55}Fe$ reactions are identified successfully.

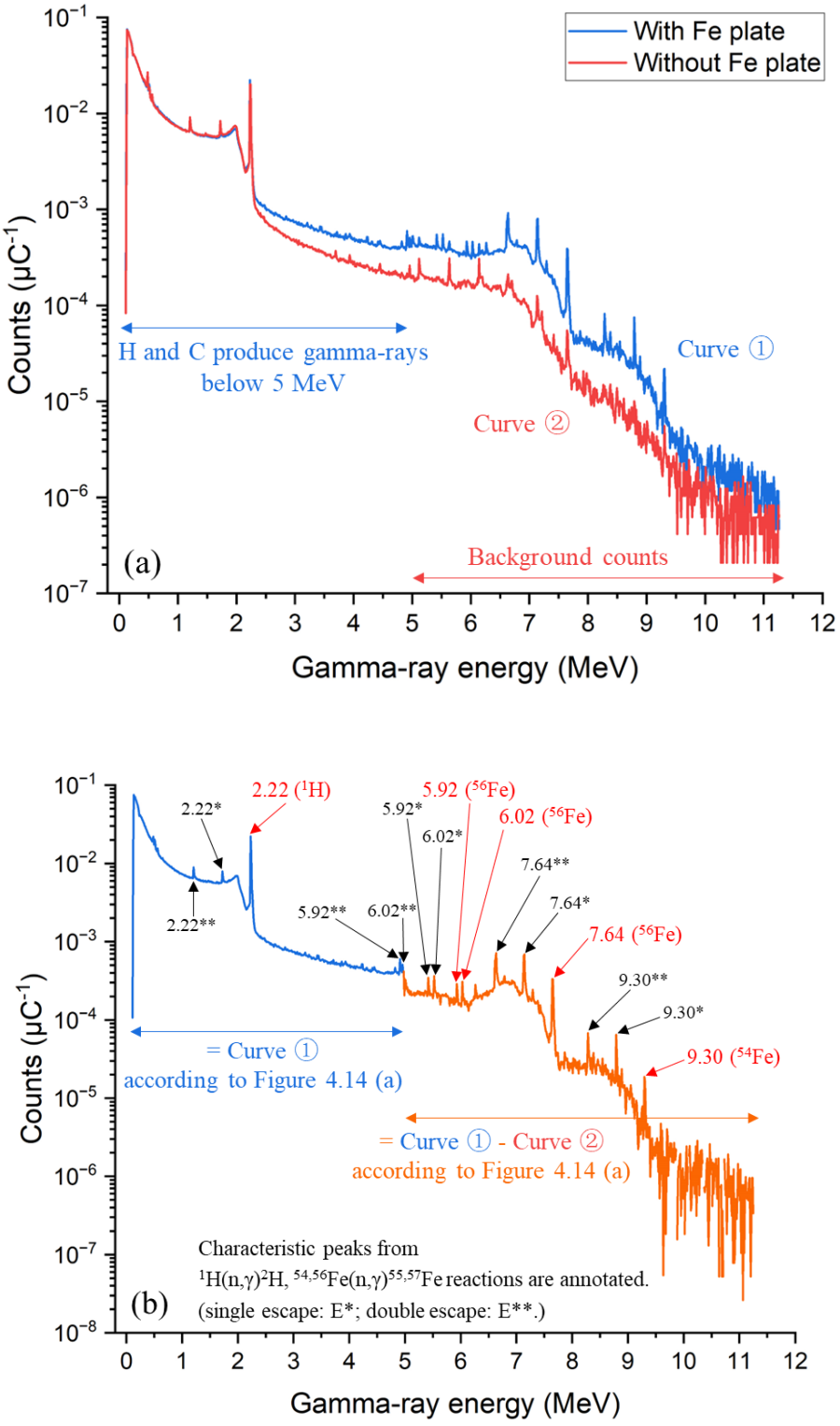

Figure 4.14. Gamma-ray spectra measured by Ge detector: (a) Gamma-ray spectra with and without the Fe plate; (b) Corrected gamma-ray spectrum.

4.5 Analysis of wall scattering effect in the experimental room at FNL

The neutron scattering effect in the experimental room at FNL was examined to give reference data for neutron irradiation experiments. A model of the experimental room is shown in Figure 4.15. The direct neutron dose, D_n, the target gamma-ray dose, $D_{\gamma_{target}}$, the wall scattered neutron dose, $D_{n_{wall}}$, and the wall induced gamma-ray dose, $D_{\gamma_{wall}}$, were calculated at 10-1000 cm distance to source. The results of D_n, $D_{\gamma_{target}}$, $D_{n_{wall}}$, and $D_{\gamma_{wall}}$ are shown in Figure 4.16. $D_{n_{wall}}$ and $D_{\gamma_{wall}}$ remain approximately constant in the room, while D_n and $D_{\gamma_{target}}$ is inversely proportional to the square of the distance. The results of $D_{\gamma_{target}}$ / D_n, $D_{n_{wall}}$ / D_n and $D_{\gamma_{wall}}$ / D_n are shown in Figure 4.17. $D_{\gamma_{target}}$ / D_n remains below 0.5% at 10-1000 cm distance. In contrast, $D_{n_{wall}}$ / D_n and $D_{\gamma_{wall}}$ / D_n increase rapidly, rising from 0.08% to 662.23% and from 0.04% to 314.38%, respectively, as the distance increases from 10 cm to 1000 cm. As the distance is below 100 cm, $D_{n_{wall}}$ / D_n and $D_{\gamma_{wall}}$ / D_n are below 8.3% and 4.2%, respectively. $D_{\gamma_{target}}$ is relatively low, however, $D_{n_{wall}}$ and $D_{\gamma_{wall}}$ become dominant if the distance is far from the neutron target.

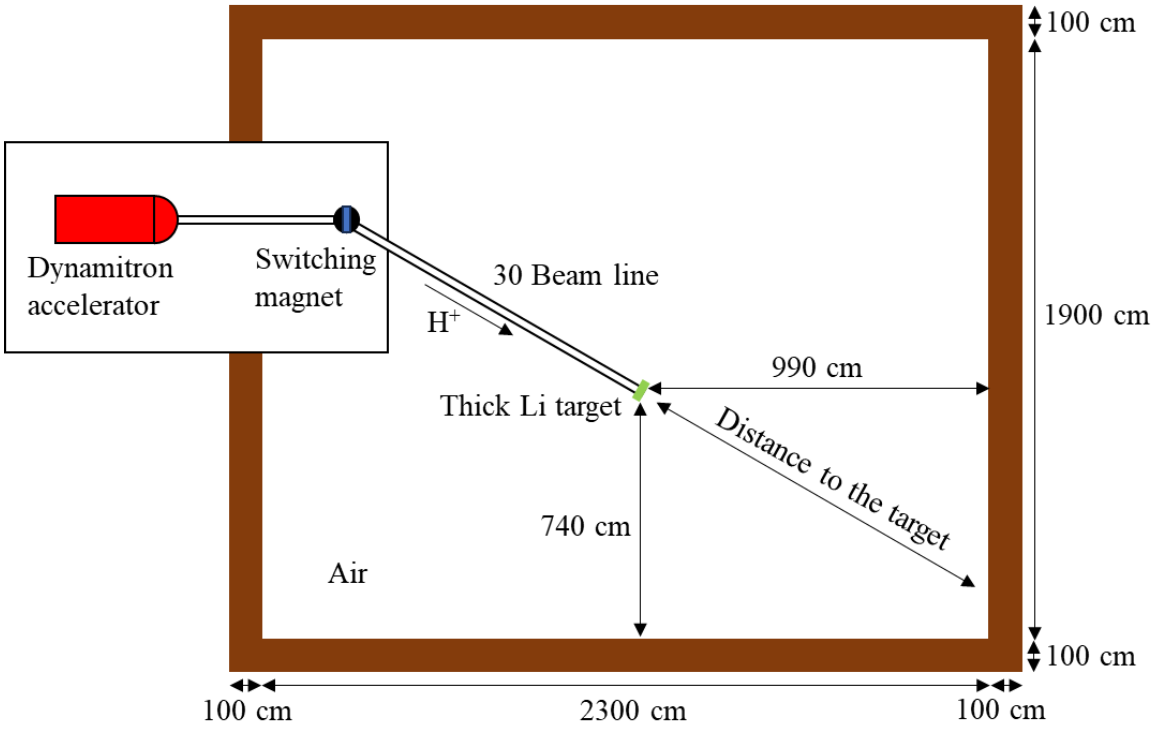

Figure 4.15. Model of the experimental room at FNL.

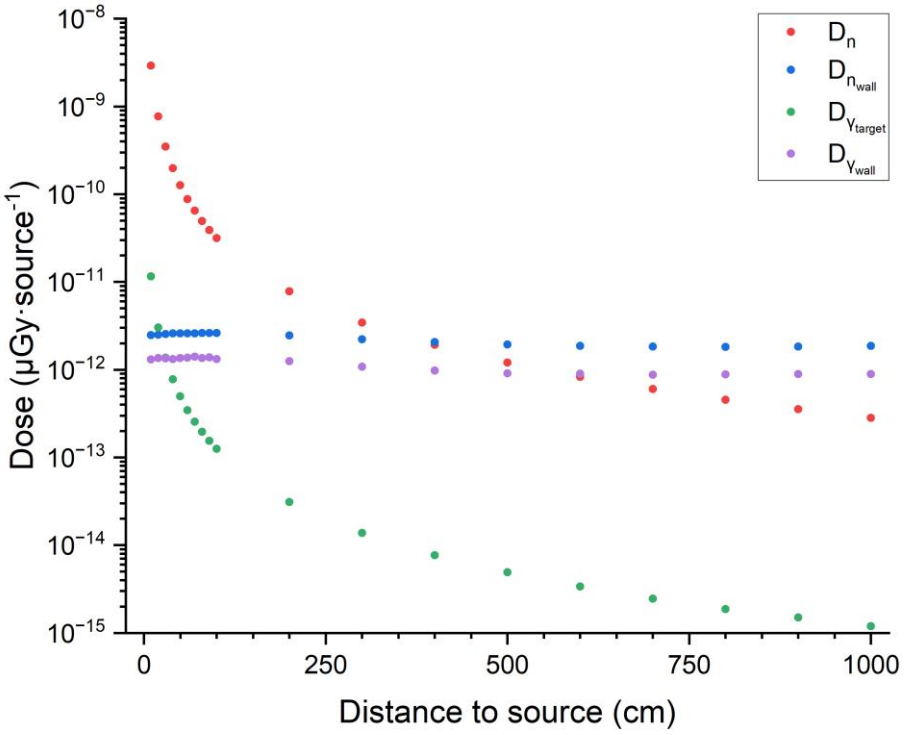

Figure 4.16. D_n, $D_{\gamma_{target}}$, $D_{n_{wall}}$, and $D_{\gamma_{wall}}$ in the experimental room at FNL.

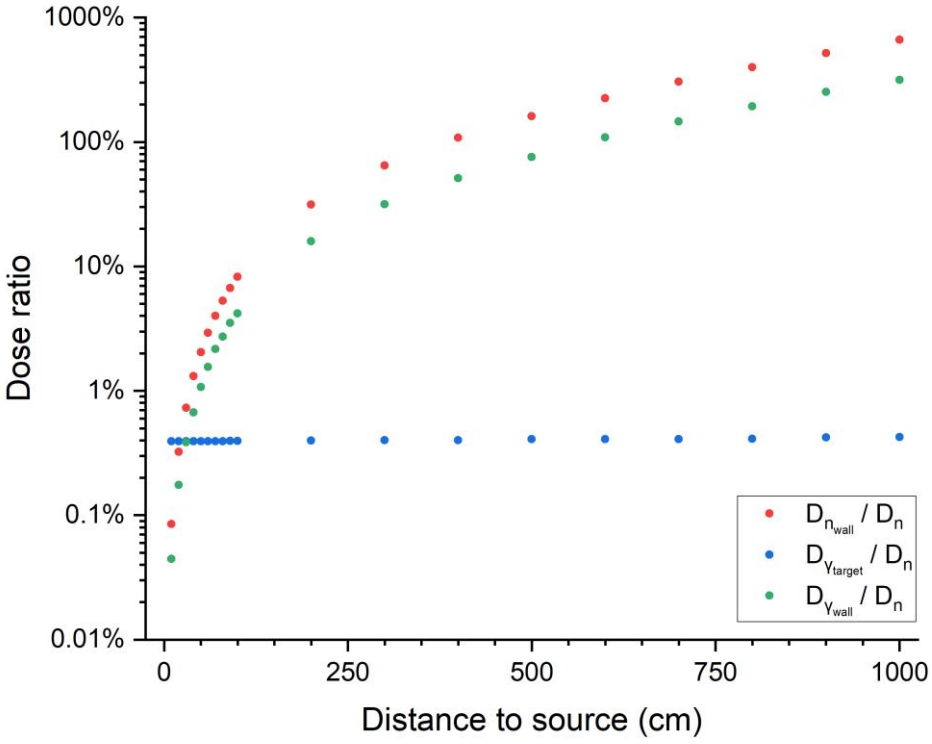

Figure 4.17. Results of D_n, $D_{\gamma_{target}}$, $D_{n_{wall}}$, and $D_{\gamma_{wall}}$.

The spectra of the target gamma-rays, wall scattered neutrons, and wall induced gamma-rays were calculated, as shown in Figure 4.18. In Figure 4.18 (a), gamma-rays are observed in the energy range up to 13 MeV due to the neutron interactions with C, Si, P, S, Cr, Mn, Fe, Ni, and Cu elements from the neutron target. In Figure 4.18 (b), the proportions of thermal, epithermal, and fast neutrons at 10-1000 cm distance to target are 70.4-81.6%, 4.7-3.8%, and 25.3-14.6%, respectively. As the measuring point becomes closer to the concrete wall, the proportion of thermal neutron increases while the proportion of epithermal neutron remains constant. In Figure 4.18 (c), gamma-rays are observed in the energy range up to 11 MeV due to the interactions of scattered neutrons with H, O, Na, Mg, Al, Si, S, K, Ca, and Fe elements from the concrete material.

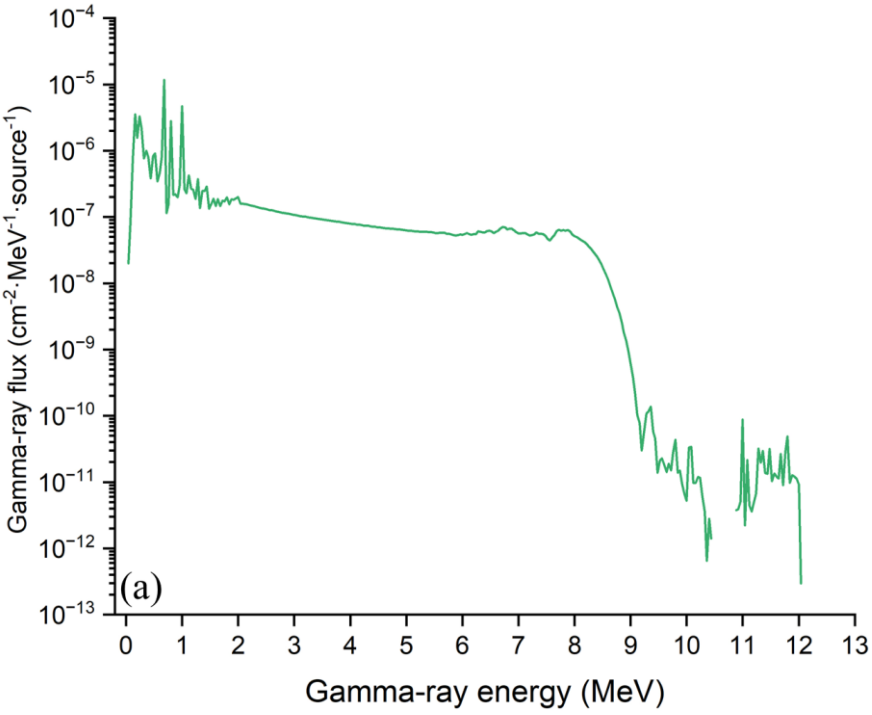

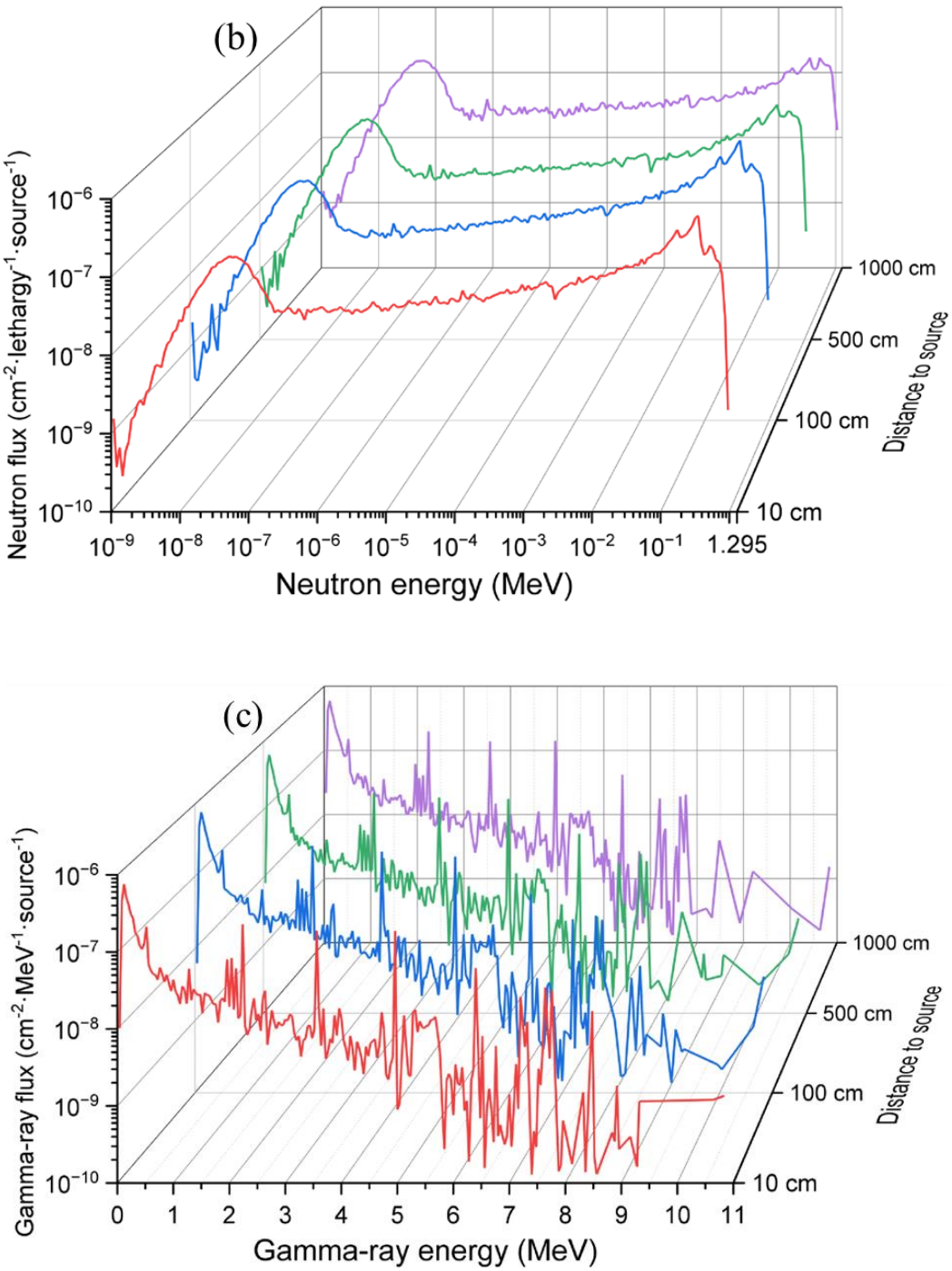

Figure 4.18. Contaminant neutrons and gamma-rays: (a) Target gamma-ray spectrum at 10 cm distance; (b) Scattered neutron spectra; (c) Wall-induced gamma-ray spectra.

Chapter 5. Summary and Future work

5.1 Summary

In this dissertation, various standard n-γ mixed fields were designed and developed by irradiating the moderator assemblies with the ~2.5 MeV D-D neutron source at OKTAVIAN and the ~2.95 MeV proton thick Li neutron source at FNL moderator assemblies and D-D and p-Li neutron sources. Different moderator assemblies are designed and developed with different combinations of Fe, W, Pb, Bi, LiF, MgF_2, TiF_3, C, and PE materials. These standard fields were classified into F-dominated field, E-dominated field, T-dominated field, as well as gamma-ray-only field, with arbitrary dose ratios, D_γ/D_n, neutron spectra with dominant energies from thermal to fast neutrons, and high gamma-ray energy spectra (up to ~10 MeV).

In Chapter 3, in the n-γ mixed fields, D_γ/D_n were produced as follows: 1.0-977.0% for F-dominated field (D_{fast}/D_n = 98.4-100.0%), 5.0-921.1% for E-dominated field (D_{epi}/D_n = 74.0-85.4%), 0.7-946.3% for T-dominated field ($D_{thermal}/D_n$ = 90.1-90.8%), and 11880.6% for gamma-ray-only field ($D_\gamma/D_{\gamma+n}$ = 99.2%). The maximum gamma-ray energy of these n-γ mixed fields is up to 12 MeV. The target gamma-ray dose was estimated as 2.06×10^4 μGy·h^{-1} to 9.34 μGy·h^{-1} at the distance to source from 1 cm to 100 cm. The target gamma-ray dose was not negligible, and it should be removed by a shielding material with appropriate thickness (Fe: ≥ 16cm; W: ≥ 5 cm; Pb: ≥ 11 cm; Bi: ≥ 12cm). $\dot{D}_\gamma$ and $\dot{D}_n$ of the n-γ mixed fields at the OKTAVIAN facility (10^9 n/s) were provided as reference, and a 5-20 cm Pb reflector was recommended to enhance $\dot{D}_\gamma$ and $\dot{D}_n$. The operation parameters of OKTAVIAN facility were introduced and the source term of D-D neutron was provided. The room effect of the experimental room was analyzed by calculating D_n', $D_{\gamma_{target}}$, $D_{n_{scattered}}$, and $D_{\gamma_{room}}$ and spectra of room scattered neutrons and room generated gamma-rays.

In Chapter 4, a ~10 MeV gamma-ray field was developed with a wide energy spectrum of characteristic gamma-rays was produced at 2.22, 5.92, 6.02, 6.38, 7.28, 7.64, 8.89, 9.30, and 10.04 MeV. The dose contaminations of the target gamma-rays, scattered neutrons, and wall-induced gamma-rays were effectively suppressed in the experimental room, i.e. η = 1.01%. At the exit of the moderator assembly, $\dot{D}_\gamma$ was calculated as 3.57×10^{-2} μSv·μC^{-1} via MCNP6 and 3.56×10^{-2} μSv·μC^{-}

[1] via PHITS (ver.3.320). The experimental result of $\dot{D}_\gamma$ was measured as 3.52 × 10^{-2} μSv·μC^{-1} using the GD-301, with errors of 1.64% and 1.28% compared with MCNP6 and PHITS (ver.3.320) simulation results, respectively. $\dot{D}_e$ and $\dot{D}_n$ were determined as 3.96% and 0.33% via MCNP6 and 3.28% and 0.32% via PHITS (ver.3.320), respectively. The spectrum of the gamma-ray field was measured using a Ge detector, and 2.22 MeV, 5.92 MeV, 6.02 MeV, 7.64 MeV, and 9.30 MeV peaks were identified clearly. When high-energy gamma-rays penetrate or interact with even a thin material, a small number of secondary electrons are emitted from the material, with energies corresponding to those of the incident gamma rays. In PHITS simulations, secondary electrons were discovered to be emitted from the moderator assembly, with the electron flux approximately two orders of magnitude lower than the gamma-ray flux. However, in the energy range above 1 MeV, f_{E_e} is approximately two orders of magnitude higher than f_{E_γ} for the GD-301. As a result, the electron absorbed dose of the GD-301 became comparable to the gamma-ray absorbed dose, i.e. $\dot{D}_{e_{glass}} : \dot{D}_{\gamma_{glass}} \approx 1{:}1$. In the dose measurement of BNCT, secondary electrons may introduce significant errors into the dose reading of the GD-301, if the electron absorbed dose is not properly corrected. Alternatively, a thin filter (e.g. 3.5 mm Fe, 3.1 mm Cu, 3.5 mm Sn, 1.2 mm W, and 2.1 mm Pb) can effectively stop these electrons and avoid unwanted electron dose deposition within the GD-301.

These reference n-γ mixed fields are valuable for calibrating and testing dosimeters and detectors, understanding the interactions of neutrons and gamma-rays with matter, and conducting dose irradiation experiments under not only BNCT but also other different n-γ mixed radiation conditions.

5.2 Future research plan

In Chapter 4, in the gamma-ray field, the dose ratio of neutron to gamma-ray is calculated as D_n / D_γ = 0.32% and the dose ratio of scattered neutron to gamma-ray is calculated as $D_{n_{wall}}$ / D_γ = 0.44%. Thus, in the gamma-ray dose measurement experiment, D_n and $D_{n_{wall}}$ were neglected. Technically, it is difficult to directly measure D_n and $D_{n_{wall}}$, because these small amounts of neutron dose cannot be detected by the GD-301. Alternatively, it is possible to measure the neutron flux by gold foil activation method. An experimental plan is shown in Figure 5.1. A piece of Au foil (1 cm ×

1 cm × 0.01 mm) is placed at 20 cm distance for irradiation. The neutron spectrum at this position is calculated via MCNP6, as shown in Figure 5.2. Thermal neutrons are dominant with flux proportion of 96.8%.

^{197}Au has large thermal neutron capture cross sections to produce an intense 0.411 MeV characteristic gamma-ray [96]:

$$^{197}\mathrm{Au} + \mathrm{n} \rightarrow {}^{198}\mathrm{Au} \xrightarrow[2.697\ \mathrm{days}]{98.3\%} {}^{198}\mathrm{Hg} + \beta^- + \bar{\upsilon} + \gamma\,(0.411\ \mathrm{MeV}) \tag{5.1}$$

The neutron flux, φ, can be determined by measuring the 0.411 MeV gamma-ray emission:

$$\varphi = \frac{A}{N \cdot \sigma \cdot (1 - e^{-\frac{\ln 2}{T_{1/2}} \cdot t})} \tag{5.2}$$

where A is the radioactivity of the activated Au foil after t time irradiation, N is the number of Au atoms, σ is the thermal neutron capture cross section, and $T_{1/2}$ is the half-life of ^{198}Au.

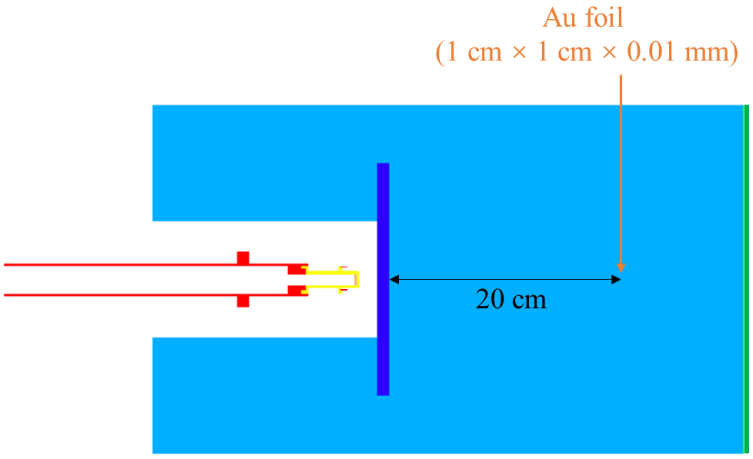

Figure 5.1. Experimental plan about neutron flux measurement.

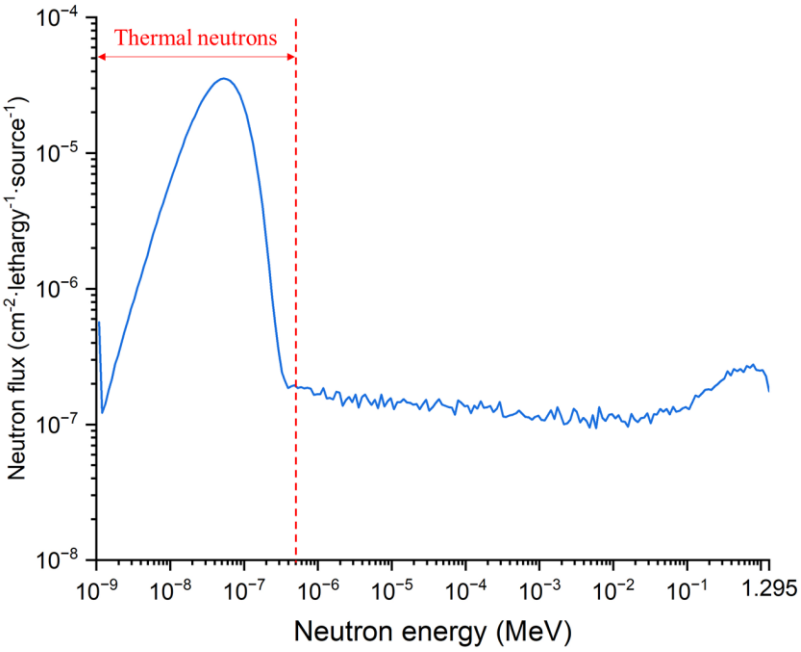

Figure 5.2. Neutron spectrum at 20 cm distance.

The ultimate goal of this dissertation is to validate and construct all the designed standard n-γ mixed fields for dosimeters and detectors in BNCT. Until now, only the gamma-ray field has been developed and validated completely. In the next step, the F-dominated, E-dominated, and T-dominate n-γ mixed fields will be validated by experiment at OKTAVIAN. The neutron spectra are will be measured by multi-foil activation method [97] and the gamma-ray spectra will be measured by Ge detector with additional neutron converters (candidates: Fe, W, LiF, Li_2CO_3, B_4C, PE, etc.). Alternatively, a liquid-moderator-based neutron spectrometer [98] is available at OKTAVIAN to measure the neutron spectra in 10 keV – 10 MeV.

Neutron and gamma-ray doses will be measured by the dual-filter method, as shown in Figure 5.3. In this method, two pieces of the GD-301 are controlled with specific neutron and gamma-ray responses by two different shielding filters. By subtraction results from the two pieces of the GD-301, gamma-ray dose, D_γ, and neutron dose, D_n, can be calculated by:

$$\begin{cases} D_{filter-1} - D_{filter-2} = (\mathrm{a}\cdot D_n + \mathrm{b}\cdot D_\gamma) - (\mathrm{a}\cdot D_n + \mathrm{c}\cdot D_\gamma) = (\mathrm{b}-\mathrm{c})\cdot D_\gamma \\ D_{filter-1} - D_{filter-2} = (\mathrm{d}\cdot D_n + \mathrm{e}\cdot D_\gamma) - (\mathrm{f}\cdot D_n + \mathrm{e}\cdot D_\gamma) = (\mathrm{d}-\mathrm{f})\cdot D_n \end{cases}$$

$$\Rightarrow \begin{cases} D_\gamma = (D_{filter-1} - D_{filter-2})/(\mathrm{b}-\mathrm{c}) \\ D_n = (D_{filter-1} - D_{filter-2})/(\mathrm{d}-\mathrm{f}) \end{cases} \quad (5.1)$$

where $D_{filter-1}$ and $D_{filter-2}$ are the total absorbed doses of the GD-301, a, b, c, d, e, and f are the conversion coefficients controlled by the filters.

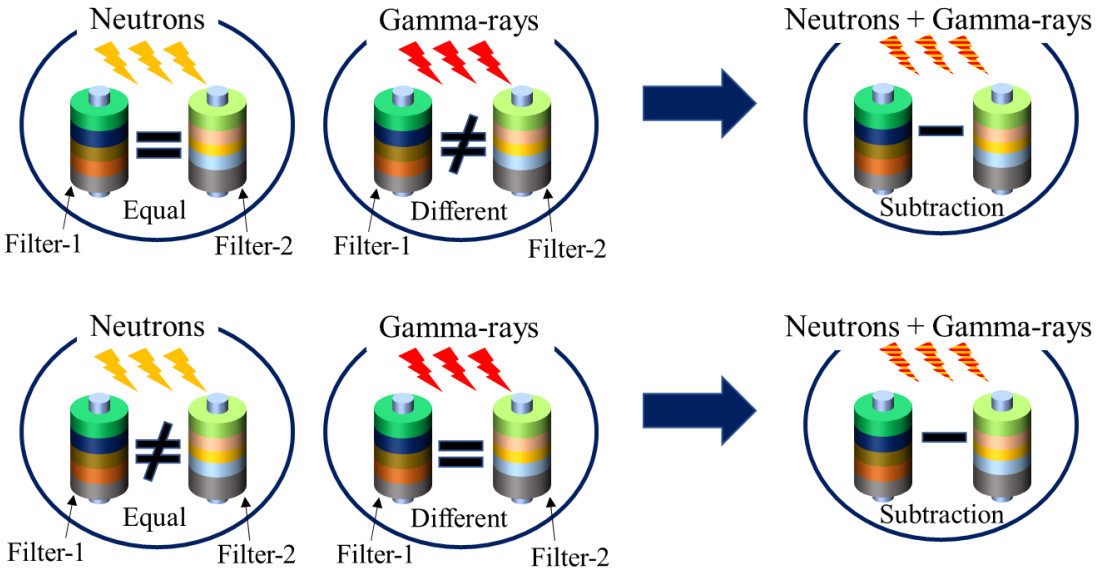

Figure 5.3. Dual-filter method for neutron and gamma-ray dose measurement.

References

1. ICRU, "Fundamental quantities and units for ionizing radiation," *Journal of the International Commission on Radiation Units and Measurements*, **11**, No.1, p.22 (2011); https://doi.org/10.1093/jicru_ndw040

2. ICRP, "ICRP Publication 60. Recommendations of the International Commission on Radiological Protection," *Ann ICRP*, **21**, p.5 (1991); https://journals.sagepub.com/doi/pdf/10.1177/ANIB_21_1-3

3. ICRP, "ICRP publication 103," *Ann ICRP*, **37**, 2-4, p.63-66 (2007); https://journals.sagepub.com/doi/pdf/10.1177/ANIB_37_2-4

4. J. Seco, B. Clasie, and M. Patridge, "Review on the characteristics of radiation detectors for dosimetry and imaging," *Physics in Medicine and Biology*, **59**, 20, p.R307-R329 (2014); https://doi.org/10.1088/0031-9155/59/20/R303

5. Russo, P. A. and Vo, D. T. Gamma-ray detectors for nondestructive analysis. Nondestructive Assay of Nuclear Materials for Safeguards and Security: Springer; 2005. p.1-5; https://doi.org/10.1007/978-3-031-58277-6_4

6. Piesch, E., "Albedo neutron dosimetry," *The International Journal of Applied Radiation and Isotopes*, **33**, 11, p.1061 (1982); https://doi.org/10.1016/0020-708X(82)90235-6

7. Podgorsak, E. B., "Review of radiation oncology physics: a handbook for teachers and students," *Vienna, Austria: IAE Agency*, **19**, p.72 (2003); https://edisciplinas.usp.br/pluginfile.php/5618241/mod_resource/content/1/Syllabus-iaea.pdf

8. Shunsuke Suzuki et al., "Developing and validating measurement methods combining 6LiF sintered capsule and Mg2SiO4: Tb (TLD-MSO-S) for γ-ray dose evaluation at accelerator-based BNCT system," *Nuclear Instruments and Methods in Physics Research Section A: Accelerators, Spectrometers, Detectors and Associated Equipment*, **1064**, 169443 (2024); https://doi.org/10.1016/j.nima.2024.169443

9. Kaiyong Tang et al., "Optimize neutron minimum detectable dose of OSL composite neutron detectors based on Al2O3:C and 6LiF," *Radiation Physics and Chemistry*, **229**, 112432 (2025); https://doi.org/10.1016/j.radphyschem.2024.112432

10. David Y.C. Huang and Shih-Ming Hsu, "Radio-photoluminescence glass dosimeter (RPLGD)," *Advances in cancer therapy*, p.553-568 (2011);
https://doi.org/10.5772/23710
11. Shih-Ming Hsu. et al., "Development and physical characteristics of a novel compound radiophotoluminescent glass dosimeter," *Radiation Measurements*, **43**, 2-6, p.538-541 (2008);
https://doi.org/10.1016/j.radmeas.2007.12.027
12. "最新がん統計," National Cancer Center Japan;
https://ganjoho.jp/reg_stat/statistics/stat/summary.html (accessed Mar. 22, 2025).
13. "死因別年間死亡数の割合," 公益財団法人生命保険文化センター;
https://www.jili.or.jp/lifeplan/lifesecurity/1226.html (accessed Mar. 22, 2025).
14. "令和 5 年(2023)人口動態統計月報年計（概数）の概況," Ministry of Health, Labour and Welfare;
https://www.mhlw.go.jp/toukei/saikin/hw/jinkou/geppo/nengai23/index.html (accessed Mar. 22, 2025).
15. "がんの放射線治療：現状と課題," Ministry of Health, Labour and Welfare;
https://www.mhlw.go.jp/file/05-Shingikai-10901000-Kenkoukyoku-Soumuka/0000127460.pdf
(accessed Mar. 22, 2025).
16. *Advances in Boron Neutron Capture Therapy*, Non-serial Publications, p.5, 7, 23-24, INTERNATIONAL ATOMIC ENERGY AGENCY, Vienna, Austria (2023).
https://www.iaea.org/publications/15339/advances-in-boron-neutron-capture-therapy
17. *Current Status of Neutron Capture Therapy*, IAEA-TECDOC-1223, p.1-3, 8, 34, INTERNATIONAL ATOMIC ENERGY AGENCY, Vienna, Austria (2001).
https://www.iaea.org/publications/6168/current-status-of-neutron-capture-therapy
18. Matsumura, Akira, "Initiatives Toward Clinical Boron Neutron Capture Therapy in Japan," *Cancer Biotherapy and Radiopharmaceuticals*, **38**, 4, p.201-207 (2023);
https://doi.org/10.1089/cbr.2022.0056
19. "Accelerator Knowledge Portal," IAEA Physics Section;
https://nucleus.iaea.org/sites/accelerators/Pages/default.aspx (accessed Jan. 30, 2025).
20. "Accelerator-based BNCT projects," International Society for Neutron Capture Therapy;

https://isnct.net/bnct-boron-neutron-capture-therapy/accelerator-based-bnct-projects-2021/ (accessed Jan. 16, 2025).

21. Zizhu Zhang et al., "A Review of Planned, Ongoing Clinical Studies and Recent Development of BNCT in Mainland of China," *Cancers*, **15**, 16, 4060 (2023); https://doi.org/10.3390/cancers15164060

22. Yoshiaki Kiyanagi et al., "Status of Accelerator-Based BNCT Projects Worldwide," *25th International Conference on the Application of Accelerators in Research and Industry (Caari 2018)*, **2160**, 050012 (2019); https://doi.org/10.1063/1.5127704

23. Takeo Nishitani et al., "Neutronics Analyses of the Radiation Field at the Accelerator-Based Neutron Source of Nagoya University for the BNCT Study," *Journal of Nuclear Engineering*, **3**, 3, p.222-232 (2022); https://doi.org/10.3390/jne3030012

24. Shunsuke Suzuki et al., "Developing and validating measurement methods combining 6LiF sintered capsule and Mg2SiO4: Tb (TLD-MSO-S) for γ-ray dose evaluation at accelerator-based BNCT system," *Nuclear Instruments and Methods in Physics Research Section A: Accelerators, Spectrometers, Detectors and Associated Equipment*, **1064**, p.169443 (2024); https://doi.org/10.1016/j.nima.2024.169443

25. Kiyomitsu Shinsho et al., "Measurements of γ-rays and neutrons in BNCT irradiation field using thermoluminescent phosphor," *Japanese Journal of Applied Physics*, **62**, 1, 010502 (2023); https://doi.org/10.35848/1347-4065/ac971e

26. Nishiki Matsubayashi et al., "Characteristics of optically stimulated luminescent dosimeter of beryllium oxide in BNCT irradiation field," *Radiation Measurements*, **161**, 106900 (2023); https://doi.org/10.1016/j.radmeas.2023.106900

27. K. Hiramatsu et al., "Gamma-Ray Dose Measurement with Radio-Photoluminescence Glass Dosimeter in Mixed Radiation Field for BNCT," *Icrs-13 & Rpsd-2016, 13th International Conference on Radiation Shielding & 19th Topical Meeting of the Radiation Protection and Shielding Division of the American Nuclear Society - 2016*, **153**, 04009 (2017); https://doi.org/10.1051/epjconf/201715304009

28. K. Tochitani et al., "Response control of RPLGD for gamma-ray dose measurement using lead filters for BNCT," *Applied Radiation and Isotopes*, **199**, 110897 (2023);
https://doi.org/10.1016/j.apradiso.2023.110897
29. F. Kamisaki et al., "Accurate gamma-ray dose measurement up to 10 MeV by glass dosimeter with a sensitivity control filter for BNCT," *Applied Radiation and Isotopes*, **209**, 111299 (2024);
https://doi.org/10.1016/j.apradiso.2024.111299
30. Józefowicz, K., andGolnik, N. and Zeilczyński, M., "Dosimetric Parameters of Simple Neutron + Gamma Fields for Calibration of Radiation Protection Instruments," *7TH SYMP ON NEUTRON DOSIMETRY*. Berlin, Germany, October 14-18,1991, Vol. 44, p.139-142, RADIATION PROTECTION DOSIMETRY (1992).
https://doi.org/10.1093/rpd/44.1-4.139
31. Tournier, B., andBarbry, F. and Verrey, B., "SILENE, a tool for neutron dosimetry," *Proceedings of the 8th Neutron Dosimetry Symposium*. Paris, France, November 13-17,1995, Vol. 70, p.345, Radiation Protection Dosimetry (1997).
https://doi.org/10.1093/oxfordjournals.rpd.a031973
32. Ferrari, M. et al., "Design development and implementation of an irradiation station at the neutron time-of-flight facility at CERN," *Physical Review Accelerators and Beams*, **25**, 10, 103001 (2022);
https://doi.org/10.1103/PhysRevAccelBeams.25.103001
33. Sumita, K. et al., "Osaka University 14 MeV Intense Neutron Source for Fusion Studies. (OKTAVIAN Program) " *Proceedings of the 12 symposium held in Juelich*. Juelich, Germany, September 13-17,1982, Vol. 15, p.53-54, Fusion Technology (1982).
https://inis.iaea.org/records/9bwna-s4f07
34. "Beamline の紹介," https://web.tohoku.ac.jp/fnl/beamline.html (accessed Jan. 16, 2025).
35. Bodansky, David and Wilson, Richard, *Nuclear Energy: Principles, Practices, and Prospects*, p.123-137, Springer New York, (2005).
https://doi.org/10.1063/1.881837
36. "APPENDIX. CROSS SECTIONS AND YIELDS: DEFINITIONS," International Atomic Energy Agency;

https://www-nds.iaea.org/medical/definitions.pdf (accessed Mar. 23, 2025).

37. "Microscopic Cross-section," Nuclear Power; https://www.nuclear-power.com/nuclear-power/reactor-physics/nuclear-engineering-fundamentals/neutron-nuclear-reactions/microscopic-cross-section/ (accessed Mar. 23, 2025).

38. Blokhin A.I. et al., "New version of neutron evaluated data library BROND-3.1," *Yad Reak Konst*, 2, p. 62-93 (2016); https://vant.ippe.ru/en/year2016/2/neutron-constants/1150-5.html

39. Ge, Zhigang et al., "CENDL-3.2: The new version of Chinese general purpose evaluated nuclear data library," *EPJ Web Conf*, **239**, p. 09001 (2020); https://doi.org/10.1051/epjconf/202023909001

40. "Evaluated Nuclear Data File (ENDF), Database," International Atomic Energy Agency; https://www-nds.iaea.org/exfor/endf.htm (accessed Jan. 16, 2025).

41. A. J. M. Plompen et al., "The joint evaluated fission and fusion nuclear data library, JEFF-3.3," *European Physical Journal A*, **56**, p. 181 (2020); https://doi.org/10.1140/epja/s10050-020-00141-9

42. Iwamoto, O. et al., "Japanese evaluated nuclear data library version 5: JENDL-5," *Journal of Nuclear Science and Technology*, **60**, 1, (2023); https://doi.org/10.1080/00223131.2022.2141903

43. Koning, A.J. et al., "TENDL: Complete Nuclear Data Library for Innovative Nuclear Science and Technology," *Nuclear Data Sheets*, **155**, p. 1-55 (2019); https://doi.org/10.1016/j.nds.2019.01.002

44. J. Hoste, *Isotopic Neutron Sources for Neutron Activation Analysis*, p.9-34, INTERNATIONAL ATOMIC ENERGY AGENCY, Vienna (1988). https://inis.iaea.org/records/5txmg-h5v96

45. R. J. Holmes, "Gamma ray and neutron sources," AAEC/S--24, p.123-132, (1982). https://inis.iaea.org/records/awyg6-4mc21

46. P. Suortti, "X-Ray, Synchrotron Radiation, and Neutron Diffraction," p.989-1023 (2003); https://doi.org/10.1016/B0-12-227410-5/00831-0.

47. Arai, M. and Crawford, K. Neutron sources and facilities. In: Bilheux, H, McGreevy, R,

Anderson, I (eds) Neutron Imaging and Applications Neutron Scattering Applications and Techniques Springer, Boston, MA2009. p.14;
https://doi.org/10.1007/978-0-387-78693-3_2

48. "World Nuclear Power Reactors 1951-2024,"
https://www.worldnuclearreport.org/reactors.html#tab=iso (accessed Feb. 2, 2025).

49. Yoshiaki Kiyanagi, "Accelerator-based neutron source for boron neutron capture therapy," *Therapeutic Radiology and Oncology*, **2**, (2018);
https://doi.org/10.21037/tro.2018.10.05

50. *Compact Accelerator Based Neutron Sources*, p.37-66, INTERNATIONAL ATOMIC ENERGY AGENCY, Vienna (2021).
https://www.iaea.org/publications/14948/compact-accelerator-based-neutron-sources

51. *Update of X Ray and Gamma Ray Decay Data Standards for Detector Calibration and Other Applications*, INTERNATIONAL ATOMIC ENERGY AGENCY, Vienna (2007).
https://www.iaea.org/publications/7551/update-of-x-ray-and-gamma-ray-decay-data-standards-for-detector-calibration-and-other-applications

52. Eckerman, K. and Endo, A., "ICRP Publication 107. Nuclear decay data for dosimetric calculations," *Ann ICRP*, **38**, 3, p. 31,39, 62-63 (2008);
https://www.icrp.org/publication.asp?id=ICRP%20Publication%20107

53. Lemos, N et al., "Bremsstrahlung hard x-ray source driven by an electron beam from a self-modulated laser wakefield accelerator," *Plasma Physics and Controlled Fusion*, **60**, 5, p.054008 (2018);
https://doi.org/10.1088/1361-6587/aab3b5

54. "Bremsstrahlung Radiation," Iowa State University, Center for Nondestructive Evaluation;
https://www.nde-ed.org/Physics/X-Ray/xrays.xhtml (accessed Jan. 28, 2025).

55. T W Huang et al., "Highly efficient laser-driven Compton gamma-ray source," *New Journal of Physics*, **21**, 1, p.013008 (2019);
https://doi.org/10.1088/1367-2630/aaf8c4

56. Shuji Miyamoto et al., "Laser Compton back-scattering gamma-ray beamline on NewSUBARU," *Radiation Measurements*, **41**, (2006);

https://doi.org/10.1016/j.radmeas.2007.01.013.

57. N. Stritt et al., "A MeV tunable gamma-ray source by Compton scattering," *NUCLEAR INSTRUMENTS & METHODS IN PHYSICS RESEARCH SECTION A-ACCELERATORS SPECTROMETERS DETECTORS AND ASSOCIATED EQUIPMENT*, **381**, 2-3, p.443-452 (1996); https://doi.org/10.1016/S0168-9002(96)00532-3

58. Michael F. L'Annunziat. Chapter 13 - Electromagnetic Radiation: photons. In: Radioactivity (Third Edition) 2023. p.709-746; https://doi.org/10.1016/B978-0-323-90440-7.00005-3

59. "Clinical Dosimetry System – Dose Ace," https://www.c-technol.co.jp/en/dosimetryequipment/clinicaldosimetry/ (accessed Jan. 26, 2025).

60. Protection, International Commission on Radiological, *ICRP Publication 74: Conversion coefficients for use in radiological protection against external radiation*, Elsevier Health Sciences, (1996). https://www.icrp.org/publication.asp?id=icrp%20publication%2074

61. Jasmina L. Vujic, "Monte Carlo Sampling Methods," https://web.tecnico.ulisboa.pt/~mcasquilho/acad/theo/simul/Vujic.pdf (accessed Feb. 10, 2025).

62. "The MCNP Code," Los Alamos National Laboratory; https://mcnp.lanl.gov/index.html (accessed Jan. 18, 2025).

63. "PHITS," Japan Atomic Energy Agency; https://phits.jaea.go.jp/index.html (accessed Jan. 18, 2025).

64. *X-5 Monte Carlo Team. MCNP - A General N-Particle Transport Code, Version 5*, p.3-78, (2003, updated 2005).

65. D.A. Brown et al., "ENDF/B-VIII.0: The 8th Major Release of the Nuclear Reaction Data Library with CIELO-project Cross Sections, New Standards and Thermal Scattering Data," *Nuclear Data Sheets, 148*, p. 1-142 (Feb. 2018); https://doi.org/10.1016/j.nds.2018.02.001

66. "Database for Prompt Gamma-ray Neutron Activation Analysis," International Atomic Energy Agency; https://www-nds.iaea.org/pgaa/ (accessed Jan. 16, 2025).

67. M. K. Reed et al., "Mixed-field dosimetry measurement of a target assembly for an accelerator-based neutron source for boron neutron capture therapy," *NUCLEAR INSTRUMENTS & METHODS IN PHYSICS RESEARCH SECTION A-ACCELERATORS SPECTROMETERS DETECTORS AND ASSOCIATED EQUIPMENT*, **419**, 1, p.160-166 (1998);
https://doi.org/10.1016/S0168-9002(98)01128-0

68. Y. Tanimura et al., "Evaluation of target photon dose mixed in mono-energetic neutron fields using Li(p,n)Be reaction," *Radiation Measurements*, **45**, 10, p.1163-1166 (2010);
https://doi.org/10.1016/j.radmeas.2010.06.013

69. Ehmann, W D and Vance, D E, *Radiochemistry and Nuclear Methods of Analysis*, p.162-175, John Wiley and Sons, New York, USA (1991).
https://www.osti.gov/biblio/5968504

70. Hubbell, J. H. and Seltzer, S. M., "X-Ray Mass Attenuation Coefficients," NIST Standard Reference Database 126;
https://dx.doi.org/10.18434/T4D01F (accessed Jan. 16, 2025).

71. "Thermal Neutron Capture Gamma-rays," IAEA.org;
https://www-nds.iaea.org/capgam/indexbye.htmlx (accessed Feb.11, 2025).

72. Sobolev, V., "MYRRHA ADS DATABASE: Part I. Thermophysical properties of molten lead-bismuth eutectic," SCK•CEN-BLG-1014, p. 8, The Belgian Nuclear Research Center (Nov. 2005).
https://inis.iaea.org/records/75rqc-acq87

73. Sumita, K. et al., "Status of Oktavian-Ⅰ and Proposal for Oktavian-Ⅱ," *Nuclear Science and Engineering*, **106**, 3, p.249-265 (1990);
https://doi.org/10.13182/NSE90-A29054

74. Murata, I., "Intense 14 MeV Neutron Source Facility (Oktavian) at Osaka University," IAEA-TECDOC--1743(Companion CD-ROM), p.110-117, (2014).
https://www-pub.iaea.org/MTCD/Publications/PDF/TE-1743-addCD_web.pdf

75. Shingo TAMAKI et al., "Radioactivation Analysis of Concrete Wall in OKTAVIAN Facility," *Plasma and Fusion Research*, **17**, (2022);
https://doi.org/10.1585/pfr.17.1405001

76. Joel G Rogers et al., "A 7-9 MeV isotopic gamma-ray source for detector testing," *NUCLEAR*

INSTRUMENTS & METHODS IN PHYSICS RESEARCH SECTION A-ACCELERATORS SPECTROMETERS DETECTORS AND ASSOCIATED EQUIPMENT, **413**, 2-3, (1998);
https://doi.org/10.1016/S0168-9002(98)00097-7

77. P.-A. Söderström et al., "Design and construction of a 9 MeV γ-ray source based on capture of moderated plutonium–beryllium neutrons in nickel," *Applied Radiation and Isotopes*, **191**, p.110559 (2023);
https://doi.org/10.1016/j.apradiso.2022.110559

78. G.B. Bishop, "A 6 MeV gamma photon facility," *Nuclear Instruments and Methods*, **121**, 3, p.499-504 (1974);
https://doi.org/10.1016/0029-554X(74)90204-3

79. Andrej Žohar et al., "Conceptual Design of Irradiation Facility with 6 MeV and 7 MeV Gamma Rays at the JSI TRIGA Mark II Research Reactor," *Advancements in Nuclear Instrumentation Measurement Methods and Their Applications (Animma 2019)*, **225**, p.04014 (2020);
https://doi.org/10.1051/epjconf/202022504014

80. Suzanne F. Nowicki, Stanley D. Hunter, and Ann M. Parsons, "Development of a quasi-monoenergetic 6 MeV Gamma Facility at NASA Goddard Space Flight Center," *NUCLEAR INSTRUMENTS & METHODS IN PHYSICS RESEARCH SECTION A-ACCELERATORS SPECTROMETERS DETECTORS AND ASSOCIATED EQUIPMENT*, **705**, (2013);
https://doi.org/10.1016/j.nima.2012.12.066

81. H. Mach and D. W. O. Rogers, "An Absolutely Calibrated Source of 6.13 Mev Gamma-Rays," *Ieee Transactions on Nuclear Science*, **30**, 2, p.1514-1517 (1983);
https://doi.org/10.1016/S0168-9002(98)00097-7

82. Munehiko Kowatari and Yoshihiko Tanimura, "Establishment of 6- to 7-MeV high-energy gamma-ray calibration fields produced using the 4-MV Van de Graaff accelerator at the Facility of Radiation Standards, Japan Atomic Energy Agency," *Radiation Protection Dosimetry*, **168**, 3, p.300-313 (2016);
https://doi.org/10.1093/rpd/ncv347

83. Shun Li et al., "Ultrafast multi-MeV gamma-ray beam produced by laser-accelerated electrons," *Physics of Plasmas*, **24**, 9, p.093104 (2017);

https://doi.org/10.1063/1.4996020

84. V. Senthilkumaran et al., "Intense gamma-ray source based on focused electron beams from a laser wakefield accelerator," *Applied Physics Letters*, **120**, 26, p.264103 (2022);
https://doi.org/10.1063/5.0095576

85. Nakajima K., "Conceptual designs of a laser plasma accelerator-based EUV-FEL and an all-optical Gamma-beam source," *High Power Laser Science and Engineering*, **2, e31**, (2014);
https://doi.org/10.1017/hpl.2014.37

86. Shouyuan Chen et al., "Shielded radiography with a laser-driven MeV-energy X-ray source," *Nuclear Instruments & Methods in Physics Research Section B-Beam Interactions with Materials and Atoms*, **366**, p.217-223 (2016);
https://doi.org/10.1016/j.nimb.2015.11.007

87. S. Matsuyama et al., "Upgrading of the 4.5 MV Dynamitron accelerator at Tohoku University for microbeam and nanobeam applications," *Nuclear Instruments & Methods in Physics Research Section B-Beam Interactions with Materials and Atoms*, **267**, 12-13, p.2060-2064 (2009);
https://doi.org/10.1016/j.nimb.2009.03.028

88. M. Baba et al., "Development of monoenergetic neutron calibration fields between 8 keV and 15 MeV," *NUCLEAR INSTRUMENTS & METHODS IN PHYSICS RESEARCH SECTION A-ACCELERATORS SPECTROMETERS DETECTORS AND ASSOCIATED EQUIPMENT*, **376**, 1, p.115-123 (1996);
https://doi.org/10.1016/0168-9002(96)00190-8

89. Shingo Tamaki et al., "Experimental test of neutron intensity monitor with isomer production reaction for p-Li neutron source for boron neutron capture therapy," *Frontiers in Nuclear Engineering*, **3**, p.1457737 (2024);
https://doi.org/10.3389/fnuen.2024.1457737

90. Drosg, M., "DROSG-2000: Neutron source reactions. Data files with computer codes for 56 monoenergetic neutron source reactions," p.3, International Atomic Energy Agency (2000).
https://inis.iaea.org/records/4phgf-htf74

91. Kulesza, J. A. et al., " MCNP® Code Version 6.3.0 Theory & User Manual," Los Alamos National Laboratory, Los Alamos, NM, USA, Tech. Rep. LA-UR-22-30006, Rev. 1, (Sep. 2022).

https://doi.org/10.2172/1889957

92. ICRP, "ICRP Publication 116. Conversion coefficients for radiological protection quantities for external radiation exposures," *ICRP Publication 116, Ann ICRP*, **40**, 2-5, p. 126, 128, 130 (2010); https://www.icrp.org/publication.asp?id=icrp%20publication%20116

93. TAKURO SHIIIBA et al., "Evaluation of the accuracy of mono-energetic electron and beta-emitting isotope dose-point kernels using particle and heavy ion transport code system: PHITS," *Applied Radiation and Isotopes*, **128**, 199 (2017); https://doi.org/10.1016/j.apradiso.2017.07.028

94. Takuro Shiiba et al., "Evaluation of the accuracy of mono-energetic electron and beta-emitting isotope dose-point kernels using particle and heavy ion transport code system: PHITS," *Applied Radiation and Isotopes*, **128**, p.199-203 (2017); https://doi.org/10.1016/j.apradiso.2017.07.028

95. Alves, A. P. et al. "HPGE gamma detector: efficiency curve evaluation during ten years of operation," 2009 International nuclear atlantic conference-INAC 2009, Rio de Janeiro, Brazil; Sep. 27 - Oct. 2, 2009. https://inis.iaea.org/records/9vaxh-9h326

96. RAFFLE, J. F., "Determination of absolute neutron flux by gold activation," *Journal of Nuclear Energy Part A Reactor Science*, **10**, 1-2, p. 8-13 (1959); https://doi.org/10.1016/0368-3265(59)90090-8

97. AGENCY, INTERNATIONAL ATOMIC ENERGY, "Practical aspects of operating a neutron activation analysis laboratory," *IAEA-TECDOC-564, IAEA, Vienna*, (1990); https://www.iaea.org/publications/820/practical-aspects-of-operating-a-neutron-activation-analysis-laboratory

98. S. Tamaki et al., "Performance test of liquid-moderator-based neutron spectrometer for BNCT: Mono-energetic and spontaneous fission spectrum neutron measurements," *NUCLEAR INSTRUMENTS & METHODS IN PHYSICS RESEARCH SECTION A-ACCELERATORS SPECTROMETERS DETECTORS AND ASSOCIATED EQUIPMENT*, **940**, p.435-440 (2019); https://doi.org/10.1016/j.nima.2019.06.063

Academic achievements

Journal articles

1. Zixu Xu, et al., Design of Moderator Assemblies for Fast, Epithermal, or Thermal Neutron–Dominated n-γ Mixed Fields Using a D-D Neutron Source, Nuclear Technology, 1–13 (2024); https://doi.org/10.1080/00295450.2024.2410642
2. Zixu Xu, et al., Development of a ~10 MeV gamma-ray field using an Fe-PE-Cd moderator assembly and a p-Li neutron source, Nuclear Technology (under review).
3. Kazuma Aoki, Zixu Xu, et al., Development and validation of gamma-ray dose measurement method using glass dosimeter covered with mixed material filters in a high-energy gamma-ray field, Nuclear Inst. and Methods in Physics Research, A (under review).

Conference proceedings

1. Zixu Xu, et al. Development of n-γ mixed fields by using a D-D neutron source for dosimetry studies of BNCT, Proceedings of the 37th Workshop on Radiation Detectors and Their Uses, Tsukuba, Ibaraki, Japan, Jan. 25-27, 2023, p.93-101, KEK (2024);（査読あり）
   https://www.i-repository.net/il/meta_pub/G0000128Lib_202325001
2. Zixu Xu, et al. Characterization of various types of n-γ mixed fields by using a D-D neutron source, Proceedings of the 2022 Symposium on Nuclear Data, Higashiosaka, Osaka, Japan, 2022, p.103-108, JAEA (2024);（査読なし）
   https://doi.org/10.11484/jaea-conf-2023-001

Conference presentations

Oral presentation

1. Zixu Xu, et al. Development of n-γ mixed fields by using a D-D neutron source for validation of material-filtered glass dosimeter for BNCT. 37th Workshop on Radiation Detectors and Their Uses, Jan. 25-27, 2023, Tsukuba, Ibaraki, Japan.

Poster presentations

2. Zixu Xu, et al. Development of n-γ mixed fields based on a D-D neutron source for validation of material-filtered RPLGD for BNCT. 11th International Symposium on Radiation Safety and Detection Technology (ISORD-11), Jul. 4-7, 2023, Seoul, South Korea.
3. Zixu Xu, et al. Simulation of developing neutron＆gamma-ray mixed field based on D-D neutron source. 2022 Symposium on Nuclear Data, Nov. 17-18, 2022, Higashiosaka, Osaka, Japan.

Acknowledgements

Appreciate my supervisor, Prof. Isao Murata, for his continuous support and patient guidance. His rigorous attitude toward scientific research, logical problem-solving mindset, and integrity in dealing with people and matters will continue to influence and encourage me throughout my life. I am truly blessed that I could meet Prof. Murata at Osaka University and become one of his doctoral students.

Appreciate Prof. Takanori Kitada and Prof. Fuminobu Sato for reviewing my doctoral dissertation and giving valuable advices on my research.

Appreciate Prof. Shigeo Matsuyama, Ms. Misako Miwa, and Mr. Sho Toyama for their sincere support and guidance during my experiment at Tohoku University. I will never forget this short but wonderful time.

Appreciate Mr. Shingo Tamaki and Ms. Sachie Kusaka for their kind assistance and care. I am deeply great grateful that I could always rely on them when facing any difficulties.

Appreciate Ms. Indah Rosidah Maemunah, Mr. Kazuma Aoki, Mr. Masaya Matsuki, Mr. Hikaru Matsunaga, Mr. Mikito Yagura, Mr. Voulgaris Nikolaos, Mr. Sota Araki, Mr. Yu Fujiwara, Mr. Ryota Eguchi, Mr. Hiroki Ichiryu, Mr. Kohei Sagara, Mr. Masashi Okamura, Ms. Yuri Morizane, Mr. Masahiro Hori, Mr. Yamato Fujii, Mr. Tsubasa Shigyo, Mr. Shogo Izutani, and all the other members who I met at OKTAVIAN in Osaka University, for their sincere help and company in these three years. Sharing life and culture with you in Japan is always unforgettable.

Appreciate my parents and all the family members for their unconditional love. Without you behind me, I would never become the person who I aspire to be.

Appreciate my friends in China for our cherished friendship.

These three years in Japan have become one of the most important memories in my life. I am looking forward the new adventures in the future. Always remember, be humble, be patient, and be thankful.

Appreciate all who I have ever met in Japan.